The Dissertation Committee for Zeyu Pan Certifies that this is the approved version of the following dissertation:

Polymer-based integrated photonic devices for interconnects

Committee:

Ray T. Chen, Supervisor

Zhigang (David) Pan

Paul S. Ho

Yaguo Wang

Hu Tao

Polymer-based integrated photonic devices for interconnects

by

Zeyu Pan

Dissertation

Presented to the Faculty of the Graduate School of

The University of Texas at Austin

in Partial Fulfillment

of the Requirements

for the Degree of

Doctor of Philosophy

The University of Texas at Austin

May 2018

Dedication

To my family, teachers, friends and anyone who help me.

Acknowledgements

I sincerely thank the faculty and staff of the Electrical and Computer Engineering Department (ECE) at The University of Texas at Austin for helping me and teaching me through all five years, and Microelectronics Research Center (MRC) provides the facilities in the clean room that I can use for the fabrication of my chip in nanometer level.

Foremost, I would like to thank my advisor, Dr. Ray T. Chen, who has been an enthusiastic and knowledgeable mentor to me. His passion for the work inspired me and his guidance has always led me to the right direction in my research. I am deeply grateful for his important contribution and guidance throughout all my research. Without his guidance and support, I would not be able to finish my research and study in the University of Texas at Austin.

I also thank my committee members, Dr. Paul S. Ho, Dr. David Pan, Dr. Yaguo Wang, and Dr. Hu Tao, for their time to serve on my committee and advise on my dissertation. I also wish to thank Dr. Harish Subbaraman and Dr. Xiaochuan Xu at Omega Optics Inc. for their kind help and guidance. I appreciate the help from the former and present members of our Optical Interconnect Group (Dr. Xingyu Zhang, Dr. John Covey, Chi-Jui Chung, Dr. Hai Yan, Dr. Zheng Wang, etc.) for their help both on my research and life. I also appreciate the help from Dr. Cheng Zhang at the University of Michigan – Ann Arbor for the collaboration and help on the imprinting. I would also like to thank Ms. Jackie Srnensky and Ms. Melanie R. Gulick for their help and administrative support.

Finally, I cannot thank my parents and family enough for always supporting me through my whole life.

Polymer-based integrated photonic devices for interconnects

Zeyu Pan, Ph.D.

The University of Texas at Austin, 2018

Supervisor: Ray T. Chen

Integrated photonic devices based on optical waveguides have been extensively studied for various applications, especially the high-speed intra- and inter-chip interconnects. Usually, a waveguide contains a core with high refractive index and cladding with lower refractive index. Among various waveguides, silicon, polymer, and silicon-polymer hybrid devices are the most promising candidates for low cost, small size, light weight, and low power consumption (CSWaP) optical interconnect. Firstly, silicon-based optical devices can be fabricated using CMOS compatible nanofabrication technology, which is already widely used to manufacture integrated circuits. Silicon photonic devices can have very small footprint and enable high density photonic circuits, due to high refractive index contrast. However, one of the intrinsic obstacles is the absence of $\chi^{(2)}$-nonlinearity in unstrained silicon due to its centrosymmetric crystal structure, making modulating photons on silicon platform a great challenge. Secondly, polymer-based devices have been found very attractive, owing to the advantages of high thermo-optic (TO) or electro-optic (EO) coefficient, high transparency in the telecommunication wavelength windows, and fabrication feasibility over large areas on printed circuit board (PCB) or other kinds of substrates. The roll-to-roll (R2R) compatible imprinting and ink-jet printing for developing polymer-based devices on flexible or rigid substrates enable large-area, light-weight, low-cost optical interconnects. However, due to the low refractive

index contrast, the polymer photonic devices always require large footprint. Finally, the silicon-organic hybrid (SOH) platform enables the marriage of the best of these two materials and thus has been receiving substantial attention.

In this dissertation, integrated photonic devices based on silicon, polymer, or hybrid platform will be presented. First, high-efficiency quasi-vertical tapers for polymer waveguide based inter-board optical interconnects will be demonstrated. A triangular-shape tapered structure is adopted above the waveguide core to transform a fiber mode into a single mode polymer rib waveguide mode as an optical mode transformer. A coupling loss of 1.79±0.30 dB and 2.23±0.31 dB per coupler for the quasi-TM and quasi-TE mode respectively have been experimentally demonstrated, across the C and L bands (1535 nm – 1610 nm). Then, a reconfigurable thermo-optic polymer switch based true-time-delay network will be analyzed and demonstrated. Thirdly, I will show a novel subwavelength-grating waveguide ring resonator based high-speed modulators, which is the largest bandwidth and the most compact footprint that has been demonstrated for the ring resonators on the silicon-organic hybrid (SOH) platform. Finally, the on-chip time-division multiplexing and de-multiplexing system will be designed and analyzed.

Table of Contents

List of Tables

List of Figures

Chapter 1: Introduction

Polymer-based integrated photonic devices receive significant attention for their enhanced performance. One of the most representative areas of application is the interconnects. The work presented in this dissertation involves the all polymer-based devices and silicon-organic hybrid (SOH) devices. A brief introduction will be covered in this chapter.

1.1 HIGH PERFORMANCE POLYMERS FOR INTEGRATED PHOTONICS

1.1.1 Electro-optic polymer

Electro-optic (EO) polymers have a remarkable EO coefficient (r33 > 400pm/V) [1], ultrafast response speed (< 1 *f*s) [2–4], small dispersion, and spin-casting compatibility, which promise low-power consumption, ultra-high speed modulation, and ease of fabrication [5].

1.1.2 Thermo-optic polymer

Among various optical switches, polymer-based thermo-optic (TO) devices have been found very attractive, owing to advantages of 1) large thermo-optic coefficient (-1~3 $x10^{-4}$ K^{-1}) [6–8], 2) high transparency in the telecommunication wavelength windows, and 3) fabrication feasibility over large areas on PCBs and other kinds of substrates. With these special features, TO polymer devices have enabled widespread applications in several areas, such as communication and radar, add/drop multiplexing, bypass switching in the event of a network failure or network jam, packet switching, etc. [6–21].

1.2 POLYMER-BASED INTEGRATED PHOTONIC DEVICES

Polymer-based passive and active photonic devices have been extensively used in various applications, including communication networks [9,11,14,19–27], optical

backplanes and inter-chip interconnects [28–36], sensors [4,37–46], etc. However, until now, the most common methods for polymer optical device fabrication are either using Reactive-ion Etching (RIE) to define the pattern into a resist, and transferring the pattern to the optical polymer via plasma etching [28,38,42]; or directly writing the pattern in a low-loss UV/Ebeam curable polymer using lithography [18,19,47,48]. Although these methods are straightforward, they are not a cost-effective way due to the complicated fabrication process involved. Moreover, these techniques are not scalable beyond the size of a wafer. In this dissertation, we introduced a novel and an etch-less solution processing technique utilizing a combination of imprinting and ink-jet printing for developing polymer photonic devices [16,20,37,44–46,49]. Owing to the roll-to-roll (R2R) compatibility of the employed solution processing techniques, photonic system development over large areas on either rigid or flexible substrates, at high-throughput, and at a low cost, is possible. Moreover, these devices can be integrated with other printed photonic and electronic components, such as light sources, modulators, antennas on the same substrate, thus achieving an integrated system that can be conformably integrated on any platform.

1.3 SILICON-ORGANIC HYBRID INTEGRATED PHOTONIC DEVICES

Silicon photonics [50,51], which can be fabricated using CMOS compatible nanofabrication technology and are the key components for integrated photonics, has been widely accepted as one of the essential technologies in the next generation optical interconnect [5,52,53]. One of the intrinsic obstacles is the absence of $\chi^{(2)}$-nonlinearity in unstrained silicon due to its centrosymmetric crystal structure, making modulating photons on silicon platform a great challenge. The silicon-organic hybrid (SOH) platform enables the marriage of the best of the two materials and thus has been receiving substantial attention. Compared with the plasma dispersion effect [54], electro-optic polymers have a

large electro-optic coefficient [1], ultrafast response speed [2–4], small dispersion, and spin-casting compatibility. It allows complex optical functionalities monolithically integrated with advanced electronics at a competitive cost. Thus, the silicon-organic hybrid (SOH) integrate photonic devices is a very promising candidate for low cost, small size, light weight, and low power consumption (CSWaP) optical interconnect.

1.4 DISSERTATION OVERVIEW

This dissertation is organized as follows:

In Chapter 2, I will demonstrate a mode transformer based on the quasi-vertical taper is demonstrated to enable high coupling efficiency from a standard SMF into a single mode polymer rib waveguide for optical inter-board interconnects.

Chapter 3 introduces a thermo-optical switch and 2-bit TO TTD module fabricated using imprinting and inkjet printing.

Chapter 4 reports the first high-speed optical modulator based on electro-optic polymer infiltrated subwavelength grating waveguide ring resonator, which is the largest bandwidth and the most compact footprint that has been demonstrated for the ring resonators on the silicon-organic hybrid platform.

In Chapter 5, the 50 GHz optical time-domain multiplexing and de-multiplexing system is designed based on IMEC iSiPP50G platform.

Finally, in Chapter 6, I will conclude the above work and discuss future direction of this dissertation.

Chapter 2: High efficiency quasi-vertical tapers for polymer waveguide based inter-board optical interconnects

A mode transformer based on the quasi-vertical taper is designed to enable high coupling efficiency for inter-board level optical interconnects involving single mode polymer waveguides and standard single mode fibers. A triangular region fabricated above the waveguide is adopted to adiabatically transform the mode from the fiber into the polymer waveguide. The effects of the geometrical parameters of the taper, including the width, height, tip width, etc. on the coupling efficiency are numerically investigated. Based on this, a quasi-vertical taper for the polymer rib waveguide system is designed, fabricated, and characterized. Coupling losses of 1.79±0.30 dB and 2.23±0.31 dB per coupler for quasi-TM and quasi-TE mode, respectively, are measured across the optical communication C and L bands (1535 nm - 1610 nm). Low-cost packaging, leading to widespread utilization of polymeric photonic devices, is envisioned for optical interconnect applications.[1]

2.1 INTRODUCTION

Polymer-based passive and active photonic devices have been extensively used in various applications, including communication networks [9,11,14,19–27], optical backplanes and inter-chip interconnects [28–36], sensors [4,37–46], etc. Low-cost and high-efficiency packaging of these devices is crucial to enable an economically viable market. The most prominent methods to couple light into a single mode polymer waveguide include edge coupling using lensed fiber [16,20,21,37] and surface coupling using grating couplers [55–60]. Although lensed fibers provide acceptable coupling

[1] Portion of this chapter has been published in Z. Pan *et al*., "Quasi-vertical tapers for polymer-waveguide-based interboard optical interconnects," Photonics Res. 3, 317–323 (2015).
Z. Pan designed, simulated, fabricated, and measured the sample, then wrote the manuscript based on the simulation, fabrication and measurement results.

efficiencies, they are more expensive than the standard single mode fibers (SMF) and are difficult to package due to their limited misalignment tolerance [38,47]. Conventional polymer grating couplers provide limited coupling efficiency in a narrow bandwidth, due to the small refractive index contrast between the polymer materials [59,60]. Some schemes utilize a thin high index coating (HIC) in order to achieve the required phase matching condition [56–58] and to improve coupling efficiency, still the bandwidth is not large enough to cover both C and L bands. High efficiency, wide bandwidth, and low-cost packaging techniques will tremendously benefit polymer waveguide based optical interconnect devices.

In this paper, we design a mode transformer based on a quasi-vertical taper [61–78] to enable high efficiency coupling between a standard SMF and a single mode polymer rib waveguide. In this design, a triangular-shape tapered structure is adopted above the waveguide core to transform a fiber mode into a single mode polymer rib waveguide mode as an optical mode transformer. It comprises of a triangular region with a fixed height, whose width is linearly tapered from the fiber end to a narrow tip at the waveguide end. We experimentally demonstrate a coupling loss of 1.79±0.30 dB and 2.23±0.31 dB per coupler for the quasi-TM and quasi-TE mode, respectively, across the C and L bands (1535 nm – 1610 nm).

2.2 Design and Optimization of Quasi-Vertical Tapers

Schematics of an optical backplane for optical inter-board interconnects and our designed taper-waveguide system to enable such high-efficiency packaging are shown in Figure 2.1(a) and Figure 2.1(b), respectively. The single mode polymer waveguide considered in this work consists of a 3.5 μm thick UV15LV (n = 1.501 @ 1.55 μm) bottom cladding; 3 μm thick UFC-170A (n = 1.496 @ 1.55 μm) top cladding; and 2.3 μm thick

(1.8 μm slab, h = 0.5 μm rib height, W = 8.5 μm rib width) SU8 (n = 1.575 @ 1.55 μm) core layer. The mode transformer based on a quasi-vertical taper consists of a triangular region with a constant height H, whose width w is linearly tapered down from W at the fiber end to a finite tip width t at the waveguide end. We choose these parameters for the triangular taper section based on the coupling efficiency simulations which will be discussed later. This tapered structure is adopted above the waveguide core to transform the fiber mode into the polymer rib waveguide mode, which works as an optical mode transformer. Because the taper height is higher at the fiber facet than at the single mode polymer waveguide end, the waveguide mode size in the vertical direction becomes larger at the fiber facets and can better match with the input/output (I/O) fiber mode. Ideally, the tapered tip should be infinitely narrow. However, due to the limited resolution achieved by the photolithography, we fixed the tip width t to a finite value. The effect of the tip width on the coupling efficiency will also be discussed later.

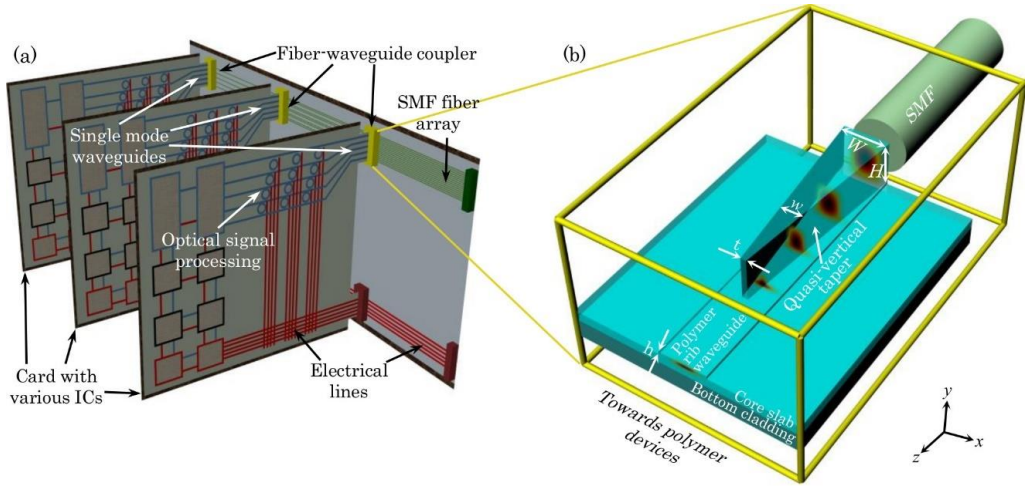

Figure 2.1: (a) Schematic of an optical backplane. (b) Schematic of a taper-waveguide system for coupling between standard SMFs and single mode waveguides. In this diagram, the top cladding is transparent to clearly show the system structure and the mode propagating inside the quasi-vertical taper and the polymer rib waveguide.

2.2.1 Mode profiles

The mode profile distributions of quasi-TM mode inside the taper at the fiber facet and device end are shown in Figure 2.2(a) and Figure 2.2(b), respectively. The mode profile distributions of quasi-TE mode at fiber facet (Figure 2.3a) and device end (Figure 2.3b) have similar plots shown here for quasi-TM mode. The polymer waveguide at device end consists a 1.8 μm thick SU8 core slab, and an 8.5 μm wide and 0.5 μm height SU8 core rib. The quasi-vertical taper at the fiber facet consists of a 1.8 μm SU8 core slab and an 8.5 μm wide and 8 μm height SU8 core rib (these values are chosen based on simulation results that will be discussed later). The eigen-modes are calculated using the beam propagation method (RSoft BeamPROP). It can be seen that the mode profile of a polymer waveguide at device end has large mismatch with the standard SMF (MFD 10.4 μm) in the vertical direction, while the mode profile of taper at the fiber facet provides a better match with the standard SMF.

When the rib height is smaller than 1.2 μm, the higher order modes are cut-off and the polymer waveguide becomes a single mode waveguide. Therefore, the polymer waveguide with rib height 0.5 μm can satisfy the single mode condition. Although the polymer waveguide with rib height 8 μm cannot satisfy the single mode condition, the quasi-vertical taper designed in this paper can filter out these higher order modes, which will be discussed later.

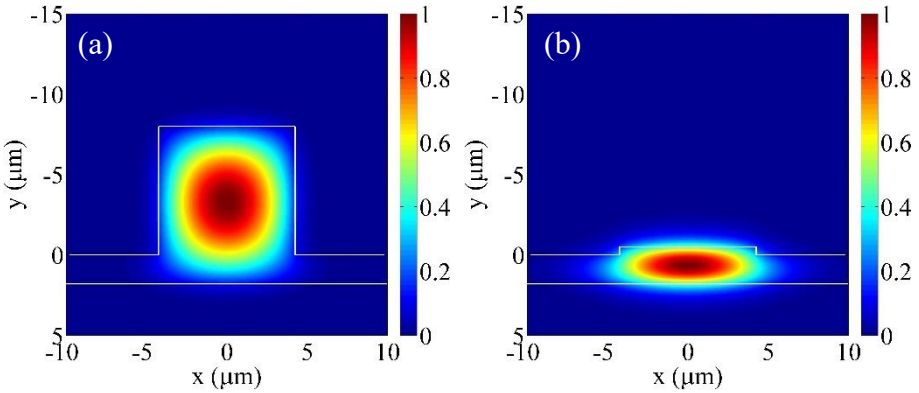

Figure 2.2: The mode profile distributions of quasi-TM mode inside the taper at (a) the fiber facet (rib width 8.5 μm, rib height 8 μm), and (b) the device end (rib width 8.5 μm, rib height 0.5 μm).

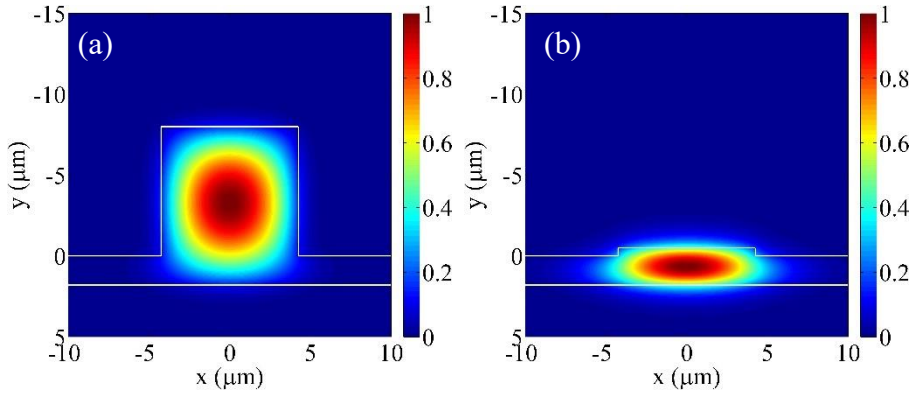

Figure 2.3: The mode profile distributions of quasi-TE mode inside the taper at (a) the fiber facet (rib width 8.5 μm, rib height 8 μm), and (b) the device end (rib width 8.5 μm, rib height 0.5 μm).

2.2.2 Coupling efficiency

The fiber coupling efficiency, η, can be calculated by a normalized overlap integral between the fiber and waveguide modes [79–81]:

$$\eta = \frac{\left|\iint F(x,y)W'(x,y)dxdy\right|^2}{\iint F(x,y)F'(x,y)dxdy \iint W(x,y)W'(x,y)dxdy} \tag{2.1}$$

where $F(x,y)$ is the function describing the complex amplitude of the single mode fiber, $W(x,y)$ is the function describing the complex amplitude of the waveguide eigen-mode, and the $'$ symbol represents the complex conjugate.

The coupling efficiencies for both quasi-TM and quasi-TE modes from the standard SMF (e.g., Corning© SMF-28) to the single mode polymer waveguide with different geometries are calculated using Eq. (2.1). The mode field diameter (MFD) of the standard SMF is 10.4 μm at 1.55 μm wavelength. The coupling efficiency of quasi-TM and quasi-TE mode from SMF into the quasi-vertical taper at the fiber facet as a function of the rib height and width are plotted in Figure 2.4a and Figure 2.4b, respectively. The white demarcation curve indicates the cut-off region. The upper right region above the white curve in Figure 2.4 indicates the multi-mode region, while the bottom left region below the white curve indicates the single mode region. Consequently, we choose the taper rib width at the fiber facet as 8.5 μm and rib height as 8 μm to have a larger coupling efficiency of 84.92% (quasi-TM mode) and 84.84% (quasi-TE mode) with the SMF, and a waveguide rib width of 8.5 μm and rib height as 0.5 μm at the device end to satisfy the single mode condition.

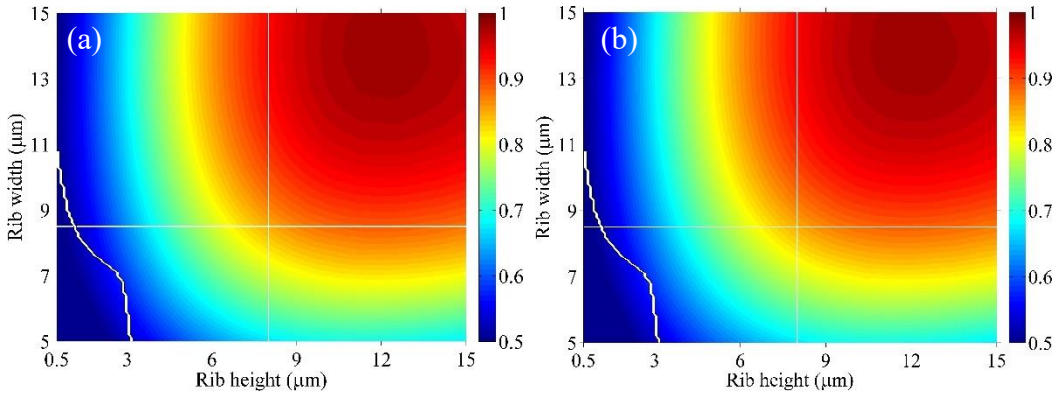

Figure 2.4: Coupling efficiency of (a) quasi-TM and (b) quasi-TE mode from a standard SMF into the taper at the fiber facet versus the rib height and rib width of the taper. The white demarcation curve indicates the cut-off region. The bottom left region under the white curve and upper right region above the white curve indicates the single-mode and multi-mode region, respectively. The intersection point of two white lines indicates the chosen rib height of 8 μm and width of 8.5 μm for the quasi-vertical taper at the fiber facet.

The total coupling efficiency from a standard SMF to a polymer waveguide through a quasi-vertical taper is calculated using the eigenmode expansion method (PhotonDesign FIMMPROP). The total length of the quasi-vertical taper is fixed at 1.2 mm. Considering the limited resolution achieved by the photolithography, the calculated total coupling efficiencies of quasi-TM mode per coupler are 68.16% (1.66 dB), 73.20% (1.35 dB), 78.56% (1.04 dB), and 83.01% (0.81 dB) for tip widths of 2.0 μm, 1.8 μm, 1.5 μm, and 1.0 μm, respectively. The calculated total coupling efficiencies of quasi-TE mode per coupler are 71.86% (1.44 dB), 75.43% (1.22 dB), 79.63% (0.98 dB), and 83.33% (0.79 dB) for tip widths of 2.0 μm, 1.8 μm, 1.5 μm, and 1.0 μm, respectively. Therefore, the coupling loss and the polarization dependence can be further reduced by using more advanced photolithography instruments to reduce the taper tip width.

The fundamental and higher order modes propagating through the taper are calculated using the beam propagation method (RSoft BeamPROP). The fundamental and second-order quasi-TM modes propagating though the taper with tip width t = 1.8 μm are shown in Figure 2.5a and Figure 2.5b, respectively. The fundamental (Figure 2.6a) and second-order (Figure 2.6b) quasi-TE modes propagating through the taper into the polymer waveguide are similar to Figure 2.5a and Figure 2.5b, respectively. The electric fields are normalized to the maximum electric field of the taper at fiber facet (z = 0 μm). As the optical beam propagates through the taper, the mode energy of the fundamental mode is drawn towards the rib and slab region, while the mode energy of the higher order mode concentrates in the taper region. Thus, the higher order modes will be filtered by the quasi-vertical taper. Thus, even though the taper supports multiple modes at the fiber facet, it only couples the fundamental mode into the single mode polymer waveguide.

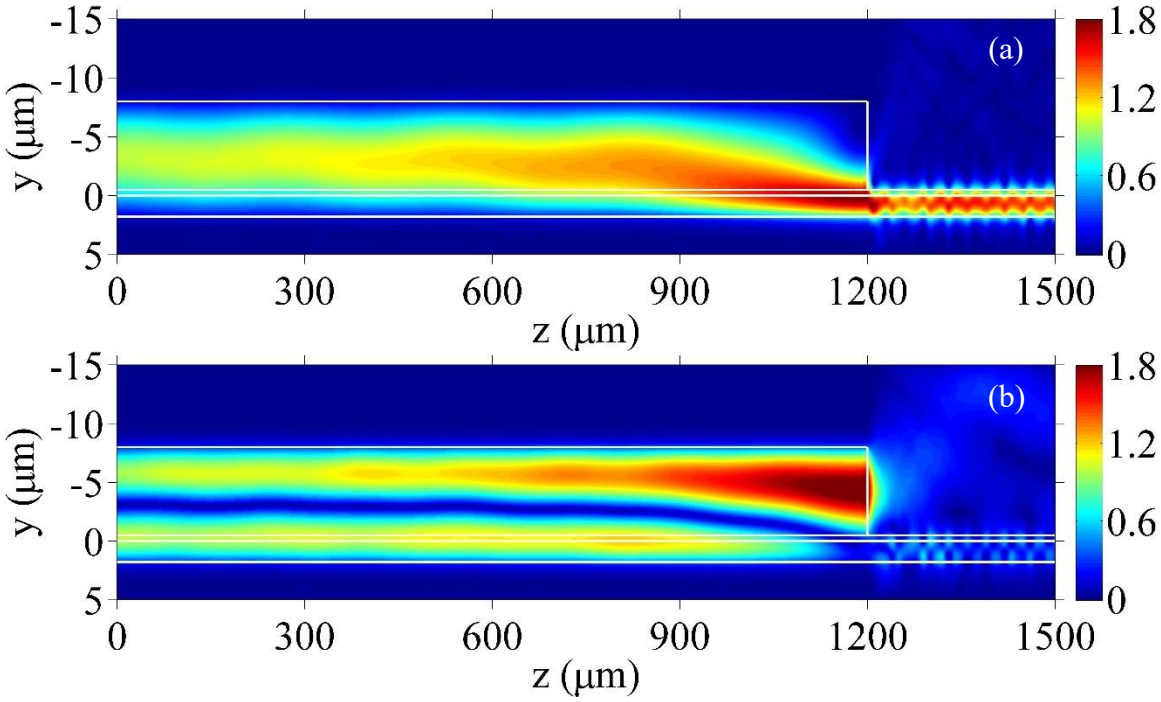

Figure 2.5: The (a) fundamental and (b) second-order quasi-TM modes propagating through the taper into the polymer waveguide. The electric fields are normalized to the maximum electric field of the taper at fiber facet ($z = 0$ μm). The length of the taper is 1.2 mm. Light propagates in the $+z$ direction from left to right. A tip width of 1.8 μm is assumed in this calculation.

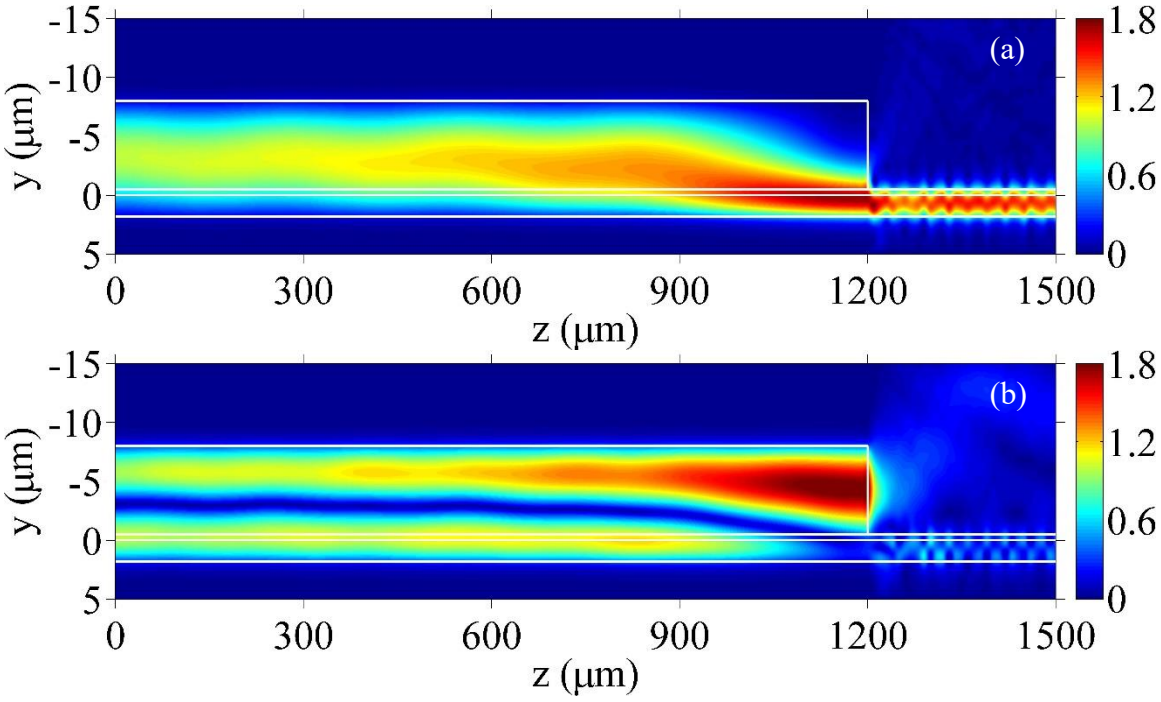

Figure 2.6: The (a) fundamental and (b) second-order quasi-TE modes propagating through the taper into the polymer waveguide. The electric fields are normalized to the maximum electric field of the taper at fiber facet ($z = 0$ μm). The length of the taper is 1.2 mm. Light propagates in the $+z$ direction from left to right. A tip width of 1.8 μm is assumed in this calculation.

2.2.3 Coupling misalignment tolerance

A larger misalignment tolerance significantly facilitates the device packaging. The misalignment tolerance in the x- and y-directions for the case of direct coupling from a lensed SMF (MFD 2.5 μm) into a polymer waveguide with a rib width of 8.5 μm and a rib height of 0.5 μm [16,20], and from a standard SMF (MFD 10.4 μm) to the quasi-vertical taper are calculated using Eq. (2.1). Figure 2.7a shows the coupling efficiency of quasi-TM mode versus the x- (horizontal) and y- (vertical) misalignments for the case of coupling from the standard SMF (MFD 10.4 μm) into the polymer waveguide through the quasi-

vertical taper. Figure 2.7b shows the coupling efficiency of quasi-TM mode versus the x- (horizontal) and y- (vertical) misalignments for the case of direct coupling from the lensed SMF (MFD 2.5 μm) into the polymer waveguide. Figure 2.7c shows the coupling loss of quasi-TE mode for both cases along the x- and y- axes. The corresponding figures for quasi-TE mode are shown in Figure 2.8a, Figure 2.8b, and Figure 2.8c, respectively. Compared to using a lensed fiber, utilizing the quasi-vertical taper (tip width 1.8 μm in this calculation), the peak coupling efficiency from a fiber into a polymer waveguide is increased from 49.95% to 73.20% (coupling loss is reduced from 3.02 dB to 1.35 dB) for quasi-TM mode, and from 49.67% to 75.43% (coupling loss is reduced from 3.04 dB to 1.22 dB) for quasi-TE mode. The 1 dB misalignment tolerance in the vertical direction is increased from 1.25 μm to 4.33 μm for quasi-TM mode, and from 1.24 μm to 4.32 μm for quasi-TE mode, compared to the lensed fiber case. The overall cost of the packaging also can be reduced by using cheaper standard SMFs.

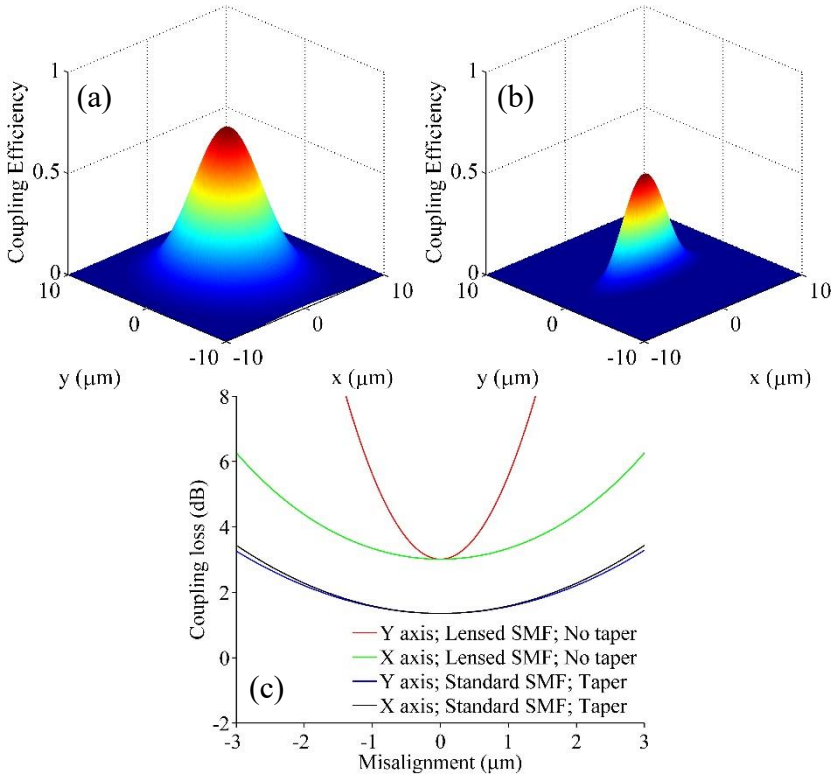

Figure 2.7: (a) The calculated optical coupling efficiency of quasi-TM mode from a standard SMF (MFD 10.4 μm) into a polymer waveguide through a quasi-vertical taper versus the misalignment in x- (horizontal) and y- (vertical) directions. (b) The calculated optical coupling efficiency of quasi-TM mode from a lensed SMF (MFD 2.5 μm) into a polymer waveguide (rib width 8.5 μm and rib height 0.5 μm) without a taper versus the misalignment in x- and y-direction. (c) The coupling loss of quasi-TM mode in (a) and (b) versus the misalignment in x- and y- axis.

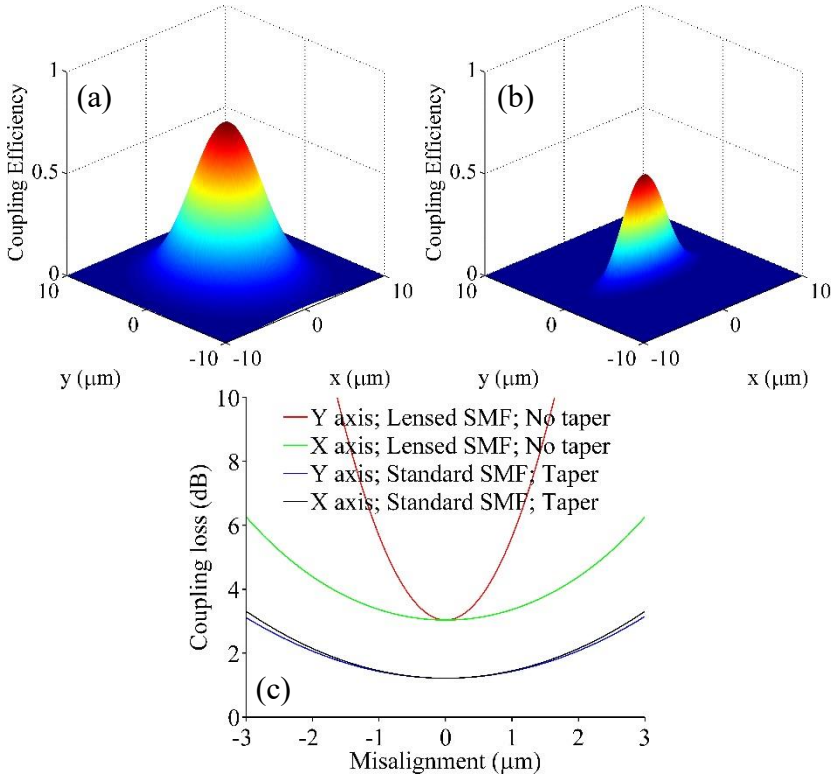

Figure 2.8: (a) The calculated optical coupling efficiency of quasi-TE mode from a standard SMF (MFD 10.4 μm) into a polymer waveguide through a quasi-vertical taper versus the misalignment in x- (horizontal) and y- (vertical) directions. (b) The calculated optical coupling efficiency of quasi-TE mode from a lensed SMF (MFD 2.5 μm) into a polymer waveguide (rib width 8.5 μm and rib height 0.5 μm) without a taper versus the misalignment in x- and y-direction. (c) The coupling loss of quasi-TE mode in (a) and (b) versus the misalignment in x- and y- axis.

2.3 FABRICATION PROCESS

A schematic of the fabrication process is shown in Figure 2.9. First, a UV15LV bottom cladding layer is spin-coated on a silicon substrate, then the slab layer (SU8 2002) is spin-coated on top of the bottom cladding layer, as shown in Figure 2.9a. Next, the waveguide rib layer (SU8 2000.5) is spin-coated and patterned using photolithography, as shown in Figure 2.9b. Then, the quasi-vertical taper layer (SU8 2007) is spin-coated and

the taper pattern is defined using another photolithography step, as shown Figure 2.9c. Finally, the top cladding (UFC170A) is spin-coated, as shown in Figure 2.9d.

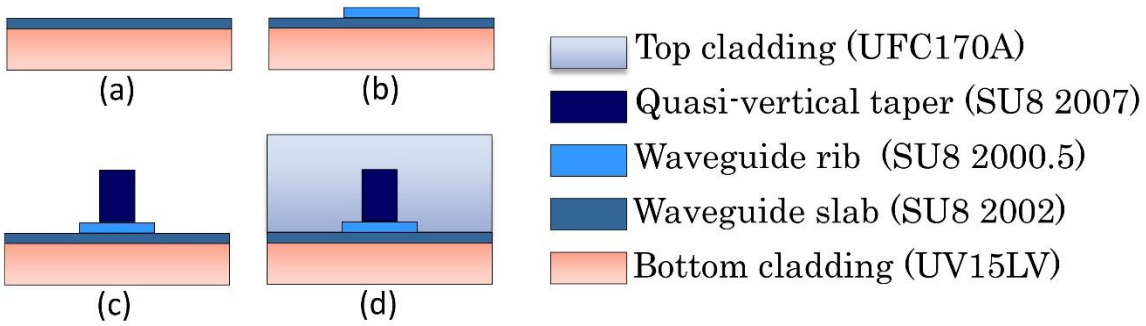

Figure 2.9: Fabrication process flow for the quasi-vertical taper. (a) Spin-coat the bottom cladding material (UV15LV) and waveguide slab layer material (SU8 2002) on the substrate. (b) Spin-coat the waveguide rib layer material (SU8 2000.5) and perform the first photolithography step to form the rib core layer of the SU8 polymer waveguide. (c) Spin-coat the top layer material of the quasi-vertical taper (SU8 2007) and perform the second photolithography step to form the triangular region of a taper. (d) Spin-coat the top cladding material (UFC170A).

The top-view and cross-section scanning electron microscope (SEM) images of a fabricated quasi-vertical taper are shown in Figure 2.10. Figure 2.10a shows a top view close to the tip, and Figure 2.10b shows a cross section of the taper at fiber facet. A zoomed image at the tip is shown in the inset of Figure 2.10a. The fabricated tip width is around 1.8 μm, due to the limited resolution of the photolithography process.

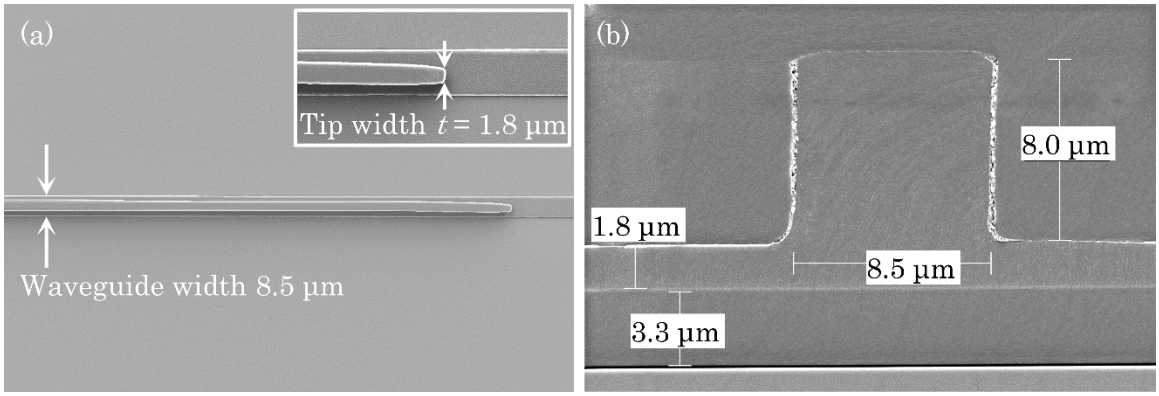

Figure 2.10: (a) Top-view SEM image of a fabricated quasi-vertical taper. (b) Cross-section SEM images of a fabricated quasi-vertical taper at fiber facet. The inset in (a) is a zoomed view at the tip.

2.4 Experimental Characterization of the Quasi-Vertical Taper

The schematic and setup to measure the propagation loss of polymer waveguides is shown in Figure 2.11. Light from a broadband infrared continuous wave ASE source (Thorlabs ASE730) is passed through a polarization controller (OZ Optics FPR-11-11-1550-8/125-P-P-1&2&3-50-3S3S-3-1-ER=30), which outputs linearly polarized TM or TE modes with a polarization extinction ratio about 34 dB. A polarization maintaining fiber (OZ Optics PMF-1550-8/125-0.25-L) and a standard SMF (Corning© SMF-28), which works as the input and output fiber respectively, are mounted on an 8-axis positioning stages (Newport PM500-C). The output power is collected by an optical power meter (Newport 2832-C). The inset at the top right corner of Figure 2.11b shows the magnified view of the aligned fibers and polymer waveguide with quasi-vertical tapers on chip. The measured propagation loss of the polymer waveguide is 0.27 dB/mm using the cut-back method [76,77].

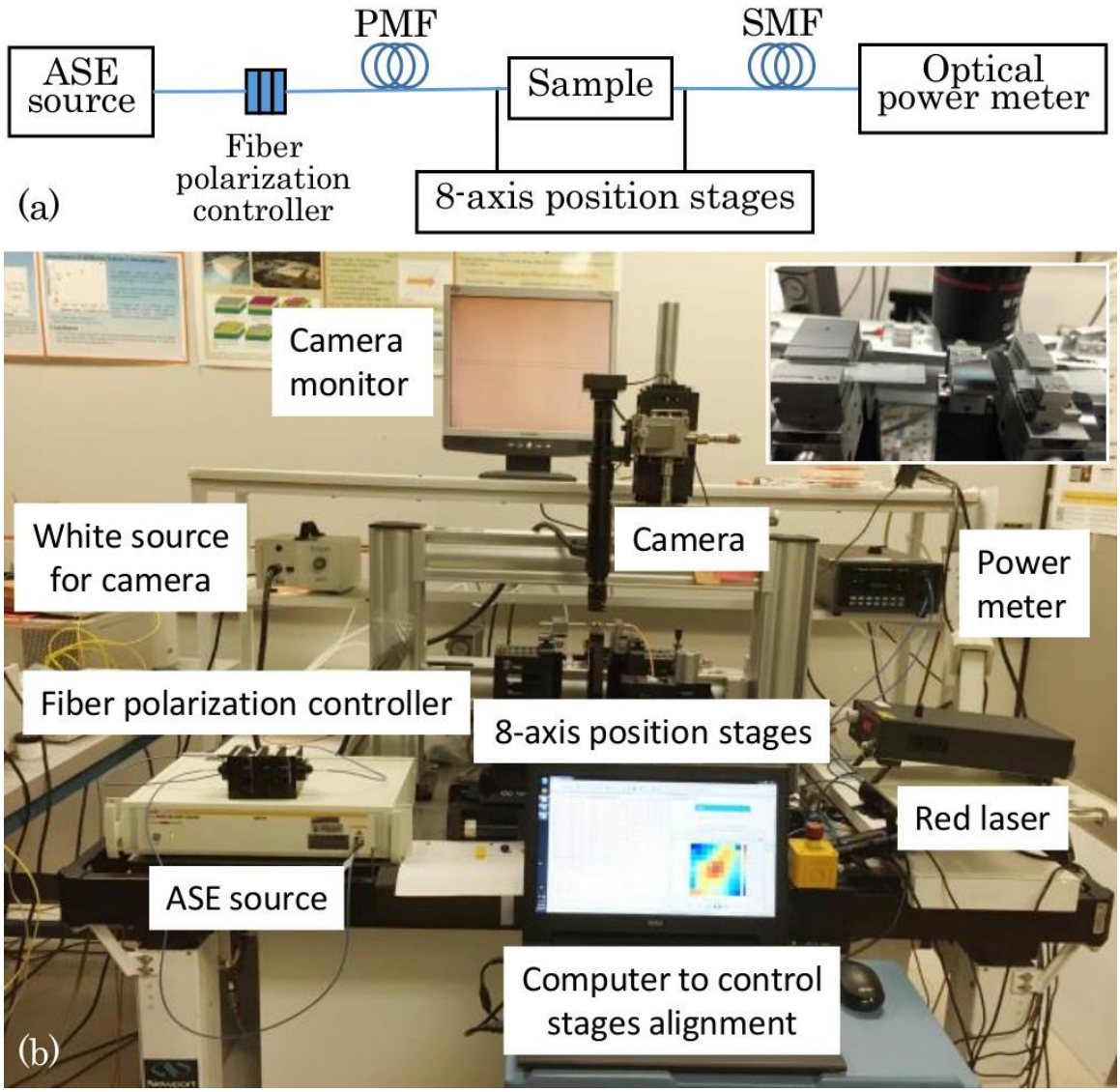

Figure 2.11: The (a) schematic and (b) experimental setup to measure the propagation loss of a polymer waveguide. The inset at the top right corner of (b) shows the magnified view of the aligned fibers and the polymer waveguide with quasi-vertical taper.

The coupling loss spectrums are measured by an Optical Spectrum Analyzer (ANDO AQ6317B). The calculated coupling losses spectrums from the measured OSA for quasi-TM and quasi-TE polarization are plotted in Figure 2.12. The measurement results

of the fabricated quasi-vertical taper demonstrate coupling losses of 1.79±0.30 dB and 2.23±0.31 dB per coupler for the quasi-TM and quasi-TE modes, respectively, across the C and L bands (1535 nm – 1610 nm). For the case of directly coupling light from a lensed SMF to a polymer waveguide without a taper, the measured coupling losses per facet are 3.44±0.24 dB and 3.85±0.24 dB for quasi-TM and quasi-TE modes, respectively. Thus, the quasi-vertical taper can reduce the coupling loss, as well as the overall packaging cost. The experimentally measured coupling losses are larger than our calculated values, which is possibly due to the scattering from the fabrication induced roughness. The additional loss for the quasi-TE mode, comparing to the quasi-TM mode, is due to the increased scattering from sidewall roughness of the fabricated waveguides.

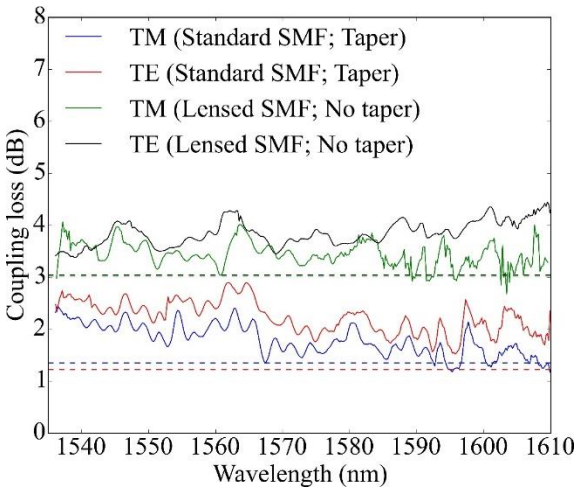

Figure 2.12: The measured coupling losses versus the wavelength. The measured coupling losses per taper are 1.79±0.30 dB and 2.23±0.31 dB for quasi-TM and quasi-TE modes, respectively, for the case of coupling light from a standard SMF (MFD 10.4 μm) to the polymer waveguide through a quasi-vertical taper. The coupling losses per facet are 3.44±0.24 dB and 3.85±0.24 dB for quasi-TM and quasi-TE modes, respectively, for the case of directly coupling light from a lensed SMF (MFD 2.5 μm) to a polymer waveguide without a taper. The different dashed lines correspond to the simulated coupling losses. The colors are shown to correspond to their respective measured counterpart.

The measured increase in coupling loss of both quasi-TM and quasi-TE modes between the standard SMF (MFD 10.4 μm) and quasi-vertical taper for horizontal (x axis) and vertical (y axis) misalignment is shown in Figure 2.13a. The measured increase in coupling loss of both quasi-TM and quasi-TE modes between the lensed SMF (MFD 2.5 μm) and polymer waveguide without a taper for horizontal (x axis) and vertical (y axis) misalignment is shown in Figure 2.13b. The solid curves are the simulation results. By using the quasi-vertical taper, the measured 1 dB misalignment tolerance in the vertical direction is increased from 1.24 μm to 4.33 μm, which agrees well with the calculated tolerance.

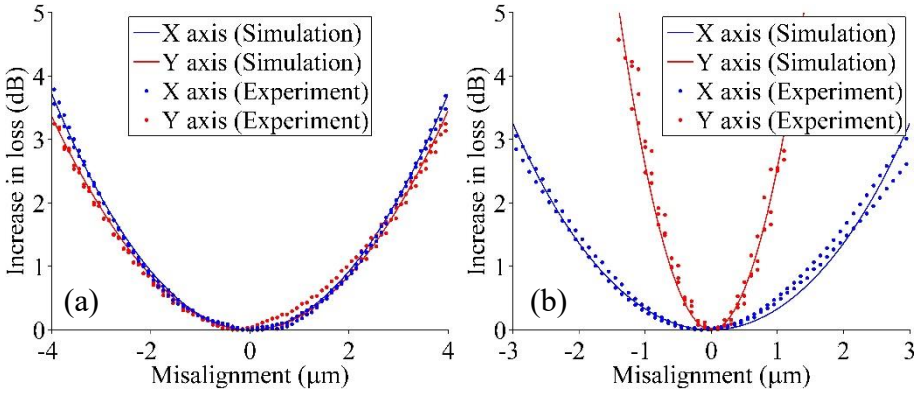

Figure 2.13: (a) The measured increase in coupling loss of both quasi-TM and quasi-TE modes between the standard SMF (MFD 10.4 μm) and quasi-vertical taper vs horizontal (x axis) and vertical (y axis) misalignment. (b) The measured increase in coupling loss of both quasi-TM and quasi-TE modes between the lensed SMF (MFD 2.5 μm) and polymer waveguide without a taper vs horizontal (x axis) and vertical (y axis) misalignment.

2.5 SUMMARY

A quasi-vertical taper, which is a triangular region on top of the single mode rib polymer waveguide, is adopted to enable high coupling efficiency from a standard SMF (MFD 10.4 μm) into a single mode polymer rib waveguide for optical inter-board interconnects. Compared to coupling light directly from a lensed SMF (MFD 2.5 μm), the coupling loss is reduced from 3.44±0.24 dB to 1.79±0.30 dB for quasi-TM mode and from 3.85±0.24 dB to 2.23±0.31 dB for the quasi-TE mode, across the C and L bands (1535 nm – 1610 nm). The 1 dB misalignment tolerance for both quasi-TM and quasi-TE modes is increased from 1.24 μm to 4.33 μm in the vertical direction. Due to the utilization of standard low cost SMFs for packaging, the overall packaging cost and packaging efforts for the single mode polymer photonic system can be minimized. Further improvement in the coupling efficiency can be achieved via adopting advanced lithography processes to reduce the taper tip width.

Chapter 3: Reconfigurable thermo-optic polymer switch based true-time-delay network

Phased-array antenna (PAA) technology plays a significant role in modern day radar and communication networks. True-time-delay (TTD) enabled beam steering networks provide several advantages over their electronic counterparts, including squint-free beam steering, low RF loss, immunity to electromagnetic interference (EMI), and large bandwidth control of PAAs. Chip-scale and integrated TTD modules promise a miniaturized, light-weight system; however, the modules are still rigid, and they require complex packaging solutions. Moreover, the total achievable time delay is still restricted by the wafer size. In this work, we propose a light-weight and large-area, true-time-delay beamforming network that can be fabricated on light-weight and flexible/rigid surfaces utilizing low-cost "printing" techniques. In order to prove the feasibility of the approach, a 2-bit thermo-optic polymer TTD network is developed using a combination of imprinting and ink-jet printing. RF beam steering of a 1x4 X-band PAA up to 60° is demonstrated. The development of such active components on large area, light-weight, and low-cost substrates promises significant improvement in size, weight, and power (SWaP) requirements over the state-of-the-art.[2]

3.1 INTRODUCTION

Integrated optical switches are important building blocks in optical links and systems [22,25,82–85]. Among various optical switches, polymer-based thermo-optic

[2] Portion of this chapter has been published in Z. Pan *et al*., "RF beam transmission of x-band PAA system utilizing large-area, polymer-based true-time-delay module developed using imprinting and inkjet printing," in Photonics West (SPIE, 2016), Vol. 9747, p. 97471T–97471T–7, and Z. Pan *et al*., "Reconfigurable thermo-optic polymer switch based true-time-delay network utilizing imprinting and inkjet printing," in Photonics West (SPIE, 2015), Vol. 9362, pp. 936214–936218.
Z. Pan designed, simulated, fabricated, and measured the sample, then wrote the manuscript based on the simulation, fabrication and measurement results.

(TO) switches have been found very attractive, owing to advantages of 1) large thermo-optic coefficient (-1~3 x10^{-4} K^{-1}) [6–8], 2) high transparency in the telecommunication wavelength windows, and 3) fabrication feasibility over large areas on PCBs and other kinds of substrates. With these special features, TO polymer switches have enabled widespread applications in several areas, such as communication and radar, add/drop multiplexing, bypass switching in the event of a network failure or network jam, packet switching, etc. [6–21]. However, until now, the most common methods for polymer optical device fabrication are either using Reactive-ion Etching (RIE) to define the pattern into a resist, and transferring the pattern to the optical polymer via plasma etching [28,38,42]; or directly writing the pattern in a low-loss UV/Ebeam curable polymer using lithography [18,19,47,48]. Although these methods are straightforward, they are not a cost-effective way due to the complicated fabrication process involved. Moreover, these techniques are not scalable beyond the size of a wafer. In this work, we introduced a novel and an etch-less solution processing technique utilizing a combination of imprinting and ink-jet printing for developing polymer photonic devices [16,20,37,44–46,49]. The structure of a complete true-time-delay reconfigurable module, comprising of an array of interconnected TO switches and polymer delay lines [9–11,23,86–88]. Phase delay configuration of a 2-bit TO TTD module and the beam steering of a 1x4 X-band PAA system utilizing the fabricated TTD modules are demonstrated. Owing to the roll-to-roll (R2R) compatibility of the employed solution processing techniques, photonic system development over large areas on either rigid or flexible substrates, at high-throughput, and at a low cost, is possible. Moreover, these devices can be integrated with other printed photonic and electronic components, such as light sources, modulators, antennas on the same substrate, thus achieving an integrated system that can be conformably integrated on any platform.

3.2 POLYMER BASED THERMO-OPTIC SWITCH

A single TO polymer switch is first introduced in this section, followed by the development of the entire TTD module later. A schematic of a single 2x2 TO switch is shown in Figure 3.1. In this design, a single mode waveguide comprising of 3.5 μm thick UV15DC80LV (n=1.501 @ 1.55 μm) bottom cladding; 3 μm thick UFC-170A (n=1.496 @ 1.55 μm) top cladding; and 2.3 μm thick (0.5 μm rib height, 1.8 μm slab) and 8.5 μm wide SU8 (n=1.575 @ 1.55 μm) core layer, is considered. An 8 μm wide and 500 μm long gold heating electrode is used to heat the polymer in the center of the junction.

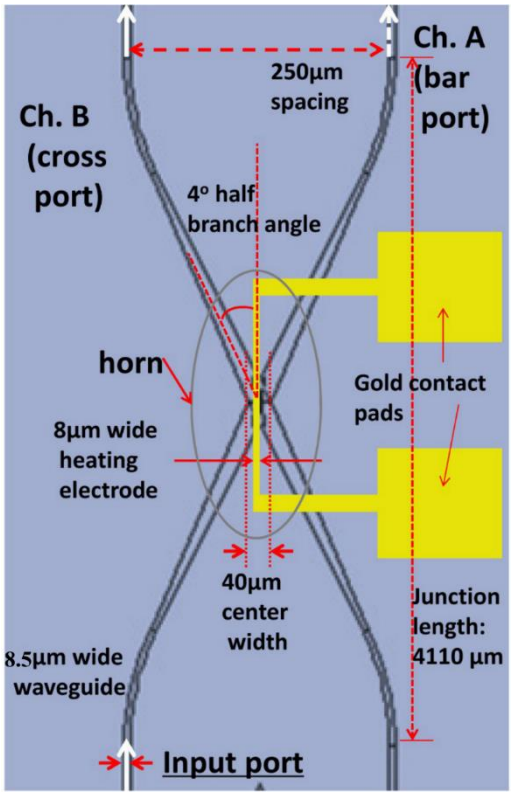

Figure 3.1: Schematic of a single 2×2 TO polymer switch [20]. Depending on whether a voltage is applied across the heating electrode to heat the junction region, light exits from the bar port (no applied voltage) and cross port (with applied voltage).

Normally, when there is no heat applied at the junction region, light from the input port will exit from the bar port. By heating the junction region in the switch, the refractive index of the polymer underneath is reduced, which creates a total-internal-reflection (TIR) condition, thus directing the light to output from the cross port. Figure 3.2(a) and Figure 3.2(b) show the simulation results performed by the beam propagating method (BeamPROP from RSoft Suite) in the OFF state (no voltage across the electrode) and the ON state (voltage across the electrode) of the TO switch, respectively.

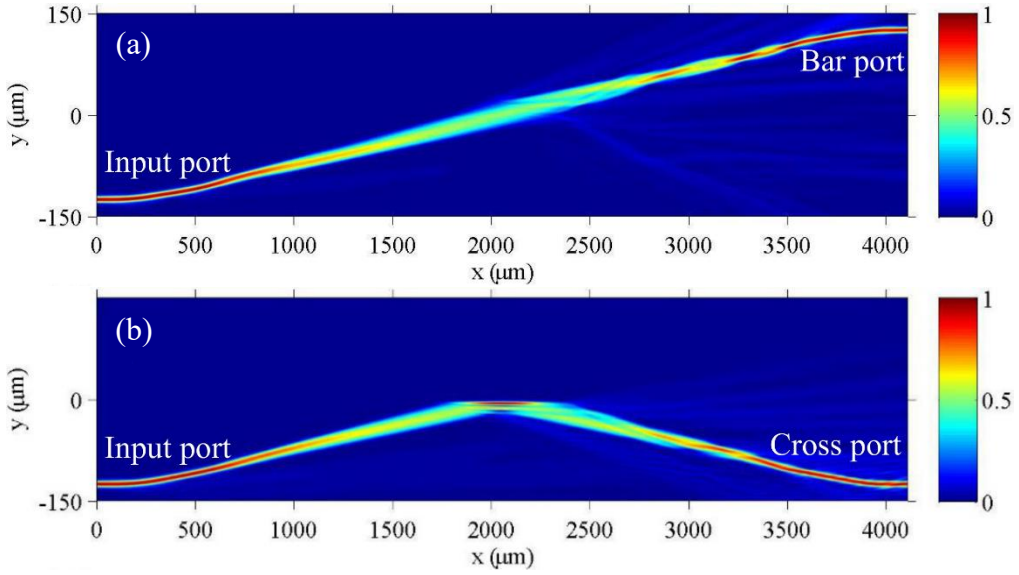

Figure 3.2: Light propagation through the switch in the (a) OFF and (b) ON states of the switch. Heating in the junction causes a local decrease in the refractive index, thus leading to total-internal-reflection (TIR) condition in the center of the horn structure.

An essential consideration in fabricating such a 2-bit TTD device is to ensure the waveguides are defect-free over the entire device area, which is a non-trivial challenge.

Hard mold imprinting gives satisfactory results for small-area devices, but lacks the capability to provide uniform imprinting over a large area, with de-molding constituting the greatest challenge [44,89]. In comparison, soft mold gives better uniformity over a large area and an easier de-molding process. However, a suitable material system needs to be selected in order to provide a reliable mold that can repeatedly be utilized. In this work, PDMS (mixed at a 10:1 ratio with curing agent) was chosen as the imprinting soft mold material. First, the 4-inch Si mold is fabricated using conventional RIE method, and is then thoroughly cleaned and coated with a surfactant to lower its surface energy. Then, PDMS is used to duplicate the TTD patterns from a 4-inch Si mold. A picture of a successfully developed large-area PDMS flexible mold is shown in Figure 3.3(a). The mold showed no defects when inspected under a microscope over the entire area. Next, the PDMS mold is used to imprint the pattern in the UV15DC80LV bottom cladding layer. Figure 3.3(b) and Figure 3.3(c) shows the microscope image of a TO polymer switch and curved polymer waveguides on the UV imprinted UV15DC80LV respectively, which demonstrates a defect-free surface achieved from such a large-area imprinting process.

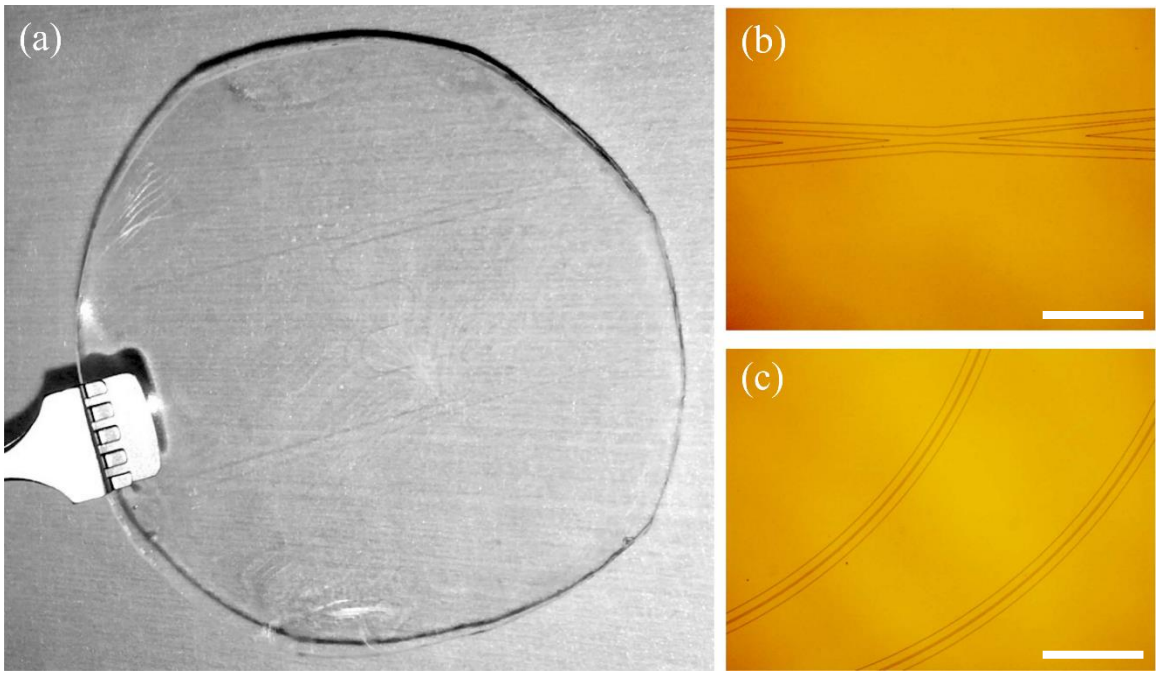

Figure 3.3: (a) The picture of a large-area PDMS flexible mold fabricated from a 4-inch silicon wafer. The microscope images of (b) the horn structure of a TO polymer switch, (c) curved polymer waveguides. The white bar at right bottom corner of (b) and (c) indicates the length of 0.5 mm.

We fabricated a single switch device in order to characterize its performance. First, a flexible mold containing a single TO switch core pattern is replicated from a silicon hard mold. The core waveguide pattern is then defined in the UV15DC80LV bottom cladding layer, using UV imprinting technique. The SEM cross-section of printed layers in the polymer waveguide is shown in Figure 3.4(a). An atomic force microscope (AFM) image of the imprinted core pattern of the waveguide in UV15DC80LV bottom cladding layer is shown in Figure 3.4(b). The measured roughness is 1.45 *nm*, which is comparable to our previous results [16]. The core layer trench is filled by inkjet-printing the SU8 material. Inkjet printing of SU8 automatically produces a flat surface profile on top, which can be

used for subsequent material printing. The top UFC-170A cladding layer is then coated on top of the core layer. Finally, gold metal heater is deposited on the top cladding layer using photolithography, ebeam evaporation, and lift-off [28,38].

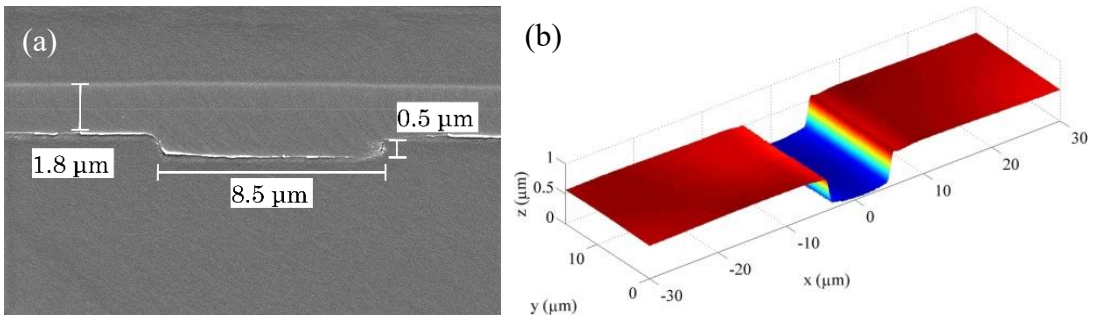

Figure 3.4: (a) SEM cross-section view of printed layers in the polymer waveguide. (b) An AFM measured bottom cladding of the polymer waveguide.

The optical microscope image of a fully fabricated single TO switch and a camera image of a fully fabricated 2-bit TO TTD module is shown in Figure 3.5 and its insert at the bottom left corner, respectively.

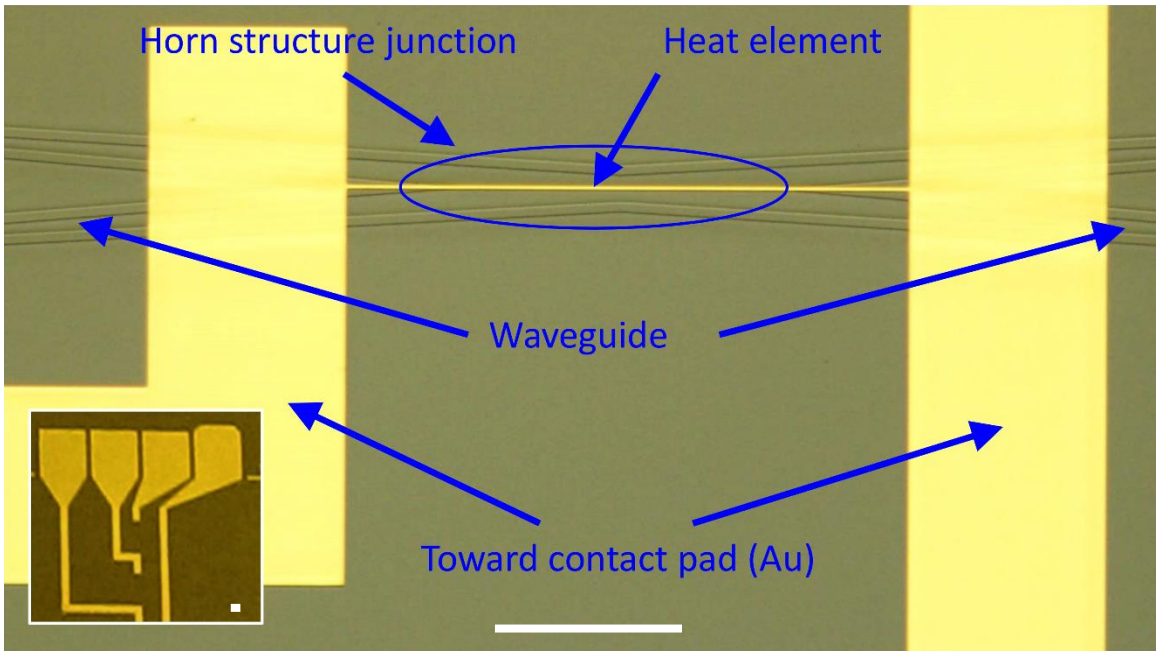

Figure 3.5: The optical microscope image of a fabricated single TO switch. Insert at left bottom corner shows a camera image of a fully fabricated 2-bit TTD module. The white bar at bottom of the figure and right-bottom corner of the insert indicates the length of 0.5 mm.

Next, the static and dynamic characteristics of the fabricated TO polymer switch are measured. Light from a 1550 *nm* tunable laser source (Santec ECL-200) is coupled into and out of the device using lensed fibers (OzOptics TSMJ-3U-1550-9/125-0.25-7-2.5-14-2). The normalized output optical power from the bar port versus the electrical power consumed by the heater is plotted in Figure 3.6(a). The switch consumes about 110 mW of the electrical power. Next, the dynamic characteristics are tested. A 100 Hz square wave signal generated by a function generator (Agilent 33120A) is applied across the heating electrode, and the output optical response from the bar port is obtained from a digital oscilloscope (HP 1660ES), as shown in Figure 3.6(b). The rise and fall times for the switch are measured to be 0.49 ms and 0.35 ms, respectively.

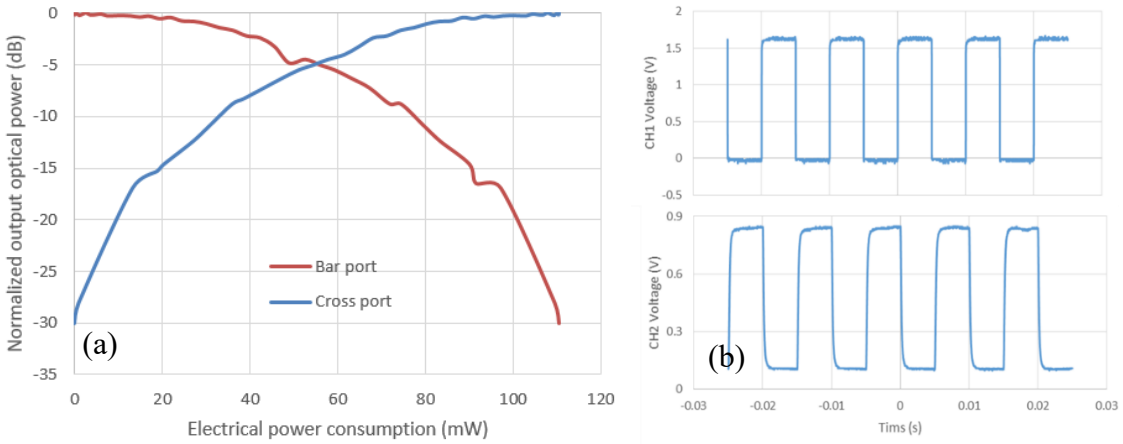

Figure 3.6: (a) The normalized output optical power of bar port shows the TO switch with a power consumption of 110 mW. (b) Optical response with square wave function applied across the heating electrode at 100 Hz frequency (CH1 represents the applied voltage and CH2 represents bar port).

3.3 2-BIT RECONFIGURABLE TTD NETWORK

In the previous section, a single TO-polymer switch device was demonstrated. In this section, we incorporate such TO switches in a reconfigurable delay line architecture, shown in Figure 3.7, and demonstrate a 2-bit TTD module. The 2-bit TTD module consists of three 2×2 TO polymer switches interconnected via judiciously chosen lengths of polymer waveguide delay lines. The minimum length increment (ΔL) determines the minimum achievable time delay step ($\Delta\tau$) according to $\Delta\tau = n_{eff}\ (\Delta L/c)$, where n_{eff} is the effective index of the mode in the waveguide and c is the speed of light in vacuum. At the first switch (n=0), the optical signal is delivered to either the reference waveguide (length L_0) or the delay line (length $L_0+\Delta L$), depending on the chosen ON or OFF state of TO polymer switch. Then, the second switch (n=1) couples the optical signal into two more

waveguides with lengths L_0 and L_0+2·ΔL. The last switch (n=2) of the 2-bit delay TTD line is used to control the optical signal to couple into one of the output waveguides.

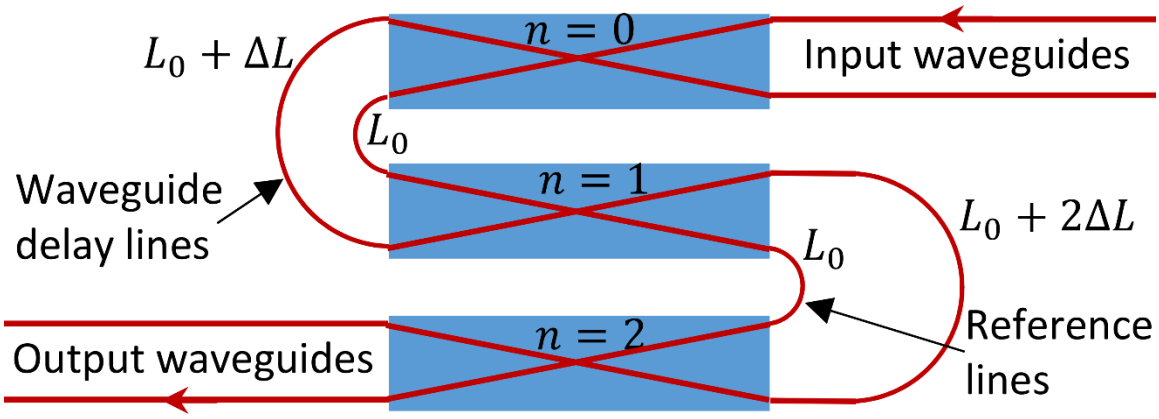

Figure 3.7: Schematic of a reconfigurable 4-bit TTD unit comprising of 2×2 TO polymer switches and polymer waveguide delay lines.

Table 3.1 lists the switch ON and OFF configuration for a 2-bit TTD module providing the time delay 0 *ps*, 11.54 *ps*, 23.09 *ps*, and 34.64 *ps,* the largest time delay chosen in order to provide a 60° steering of RF signal in an X-band PAA. Note that this largest time delay we chose is not restricted due to the printing technology, but due to our measurement capability in our laboratory setup. When both n=0 and n=1 switches are OFF, the optical signal goes through reference lines. When n=0 switch is ON and n=1 switch is OFF, the optical signal travels additional length ΔL compared to the reference line, thus the TTD module provides 11.54 *ps* time delay w.r.t the reference line. Similarly, other delay configurations can be understood from Table 3.1.

Configuration	**0$\Delta\tau$**	**1$\Delta\tau$**	**2$\Delta\tau$**	**3$\Delta\tau$**
Phase delay	**0 ps**	**11.54 ps**	**23.09 ps**	**34.64 ps**
n=0 (ΔL)	OFF	ON	OFF	ON
n=1 ($2\Delta L$)	OFF	OFF	ON	ON

Table 3.1: ON and OFF configuration for each switch in a 2-bit reconfigurable TO-switch based TTD module.

We fabricated the 2-bit TTD module using the fabrication process outlined in our previous publications [20,21]. In order to measure the time delay from the fabricated 2-bit module, we performed a phased versus frequency measurement and derived the time delay from the plots. The schematic and setup to measure the time delay of the 2-bit reconfigurable TO-switch based TTD module is shown in Figure 3.8. The optical signal paths are shown as blue lines and the electrical signal paths are indicated as red lines in Figure 3.8(a). Light at a wavelength of 1550nm from a tunable laser (Santec ECL200) is passed through a $LiNbO_3$ electro-optical modulator (COVEGA MACH-40), which modulates the RF signal generated by a network analyzer (Agilent 8510C) onto the optical carrier. The modulated light signal is then amplified by an EDFA (Amonics AEDFA-C-30I-B). A lensed polarization maintaining fiber (OZ Optics) and a lensed single mode fiber (OZ Optics), which work as the input and output fiber, respectively, are mounted on an eight-axis positioning stage (Newport XPS-C8). The sample is placed in between, and the position stages are controlled using an automation software to efficiently couple light into and out of the TTD module. The output power is amplified by an EDFA (BaySpec Metro-III_AE), which is then detected using a photodiode (Discovery Semiconductors DSC40S).

The detected RF signal is then input into the second port of the network analyzer for analyzing the time delay.

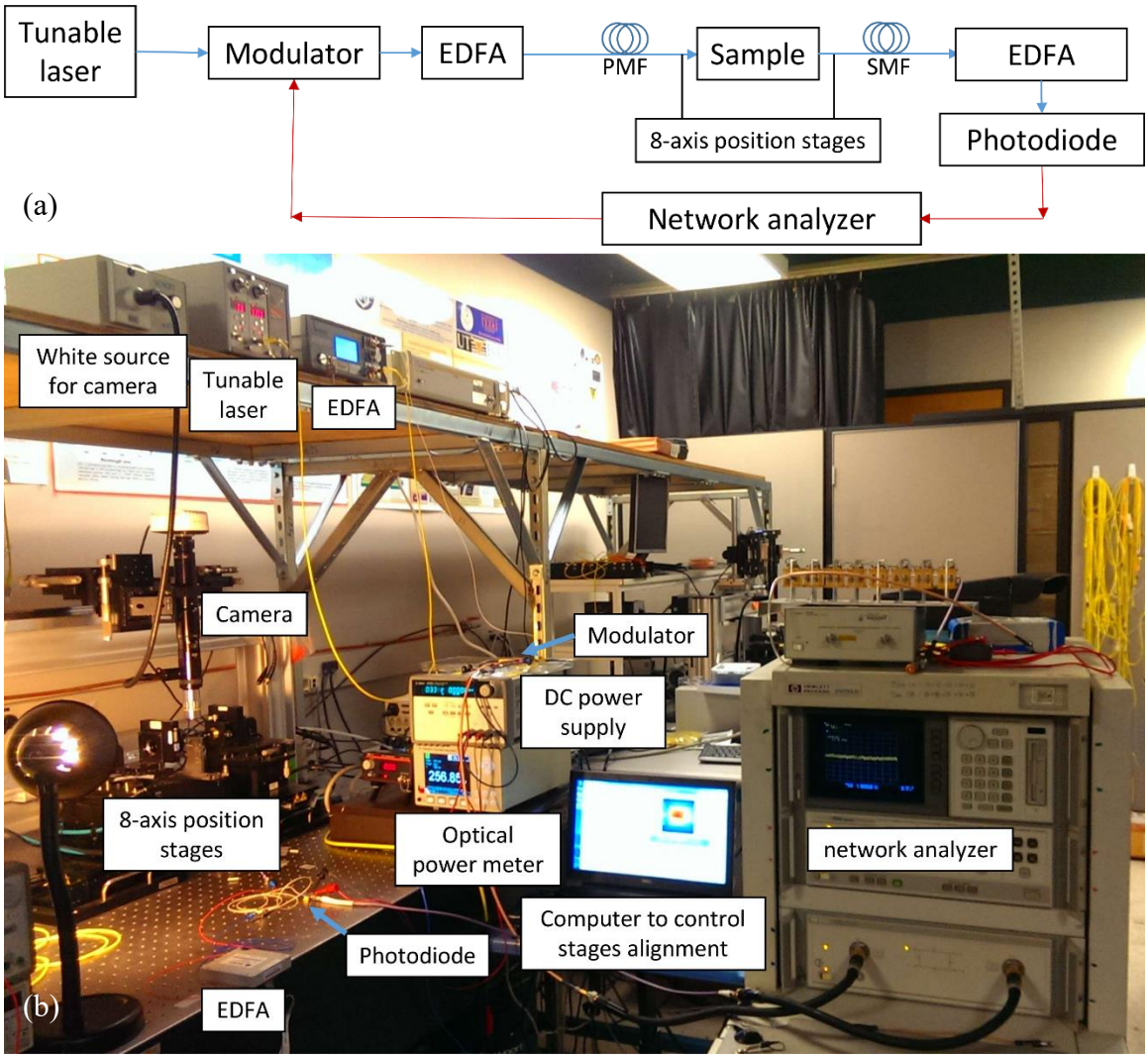

Figure 3.8: (a) Schematic and (b) experimental setup to measure the time delay from the reconfigurable 2-bit TTD module. The blue and red lines in (a) indicate the optical and the electrical signal propagation lines, respectively.

The measured phase versus frequency plots for all the delay configurations indicated in Table 3.1 are shown in Figure 3.9. The phase versus frequency plot is a straight line for all the configurations, thus confirming true-time-delay behavior. The time delay is determined by calculating the slope of the straight lines using:

$$\Delta\tau = -\frac{d\phi}{d\omega} = -\frac{1}{360} \cdot \frac{d\theta}{df} \tag{3.1}$$

The measured time delay values using Eq. (3.1) for $0\Delta\tau$, $1\Delta\tau$, $2\Delta\tau$, and $3\Delta\tau$ are 0.64 ps, 10.74 ps, 22.90 ps, and 35.39 ps, respectively, which are very close to the designed values shown in Table 3.1. The measured phase versus frequency plots of all the 4 delay line configurations from the 2-bit TTD module are shown in Figure 3.9.

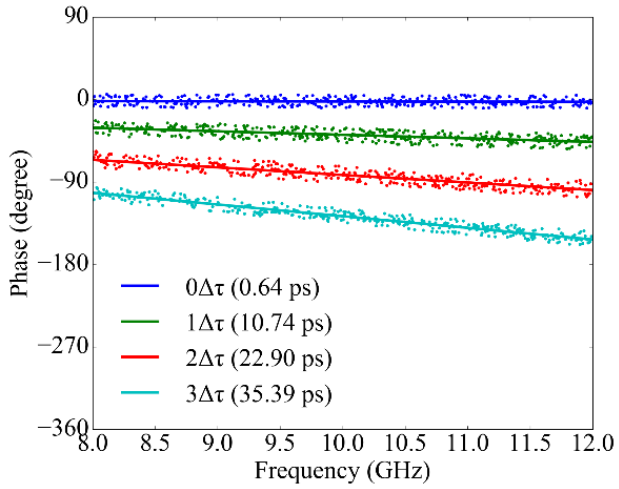

Figure 3.9: The measured phase versus frequency plots of all the 4 delay line configurations from the 2-bit TTD module.

3.4 X-BAND PHASED ARRAY ANTENNA DEMONSTRATION

A phased array antenna (PAA) can steer an RF beam with the fed phase difference between the elements without having to mechanically move the antenna. The radiation

pattern of the PAA can be reinforced at the desired direction and suppressed in undesired directions. Table 3.2 lists the delay configuration for four 2-bit TTD modules capable of providing up to ±60° steering angle for an X-band Phased Array Antenna (PAA). It should be noted that this upper limit in the steering angle is not limited by our technology, but by the characterization setup available in our laboratory for conducting antenna pattern measurements. When the 4 TTD modules are configured with $0\Delta\tau$, $1\Delta\tau$, $2\Delta\tau$, and $3\Delta\tau$ delays, respectively, a 16.78 degree steering of the RF signal is achieved. Similarly, if setting the time delay of TTD modules as $0\Delta\tau$, $2\Delta\tau$, $4\Delta\tau$, and $6\Delta\tau$ respectively, the PAA steers to 35.26 degree. Lastly, the element time delay configurations of $0\Delta\tau$, $3\Delta\tau$, $6\Delta\tau$, and $9\Delta\tau$ gives the 60 degree steering angle.

Steering Angle (deg)	**Module #1**	**Module #2**	**Module #3**	**Module #4**
60.00 °	$0\cdot\Delta\tau$	$3\cdot\Delta\tau$	$6\cdot\Delta\tau$	$9\cdot\Delta\tau$
35.26 °	$0\cdot\Delta\tau$	$2\cdot\Delta\tau$	$4\cdot\Delta\tau$	$6\cdot\Delta\tau$
16.78 °	$0\cdot\Delta\tau$	$1\cdot\Delta\tau$	$2\cdot\Delta\tau$	$3\cdot\Delta\tau$
0 °	$0\cdot\Delta\tau$	$0\cdot\Delta\tau$	$0\cdot\Delta\tau$	$0\cdot\Delta\tau$
-16.78 °	$3\cdot\Delta\tau$	$2\cdot\Delta\tau$	$1\cdot\Delta\tau$	$0\cdot\Delta\tau$
-35.26 °	$6\cdot\Delta\tau$	$4\cdot\Delta\tau$	$2\cdot\Delta\tau$	$0\cdot\Delta\tau$
-60.00 °	$9\cdot\Delta\tau$	$6\cdot\Delta\tau$	$3\cdot\Delta\tau$	$0\cdot\Delta\tau$

Table 3.2: Time delay configuration for each element in a 2-bit 1x4 X-Band PAA system utilizing 4 TO-TTD modules.

The far-field radiation patterns of the 1x4 PAA are measured in an anechoic chamber in our laboratory utilizing a fully automated measurement setup [9,87,88,90–94]

at a frequency of 12.5GHz. The measured results are shown in Figure 3.10. It can be seen that the simulated (solid curves) and the measured (dotted curves) agree well with each other. Using R2R manufacturing over large areas, beam steering of very large aperture PAAs is achievable in the future. Such a low-cost manufacturing alternative will tremendously benefit light-weight and conformal air- and space-borne PAA communication and radar applications.

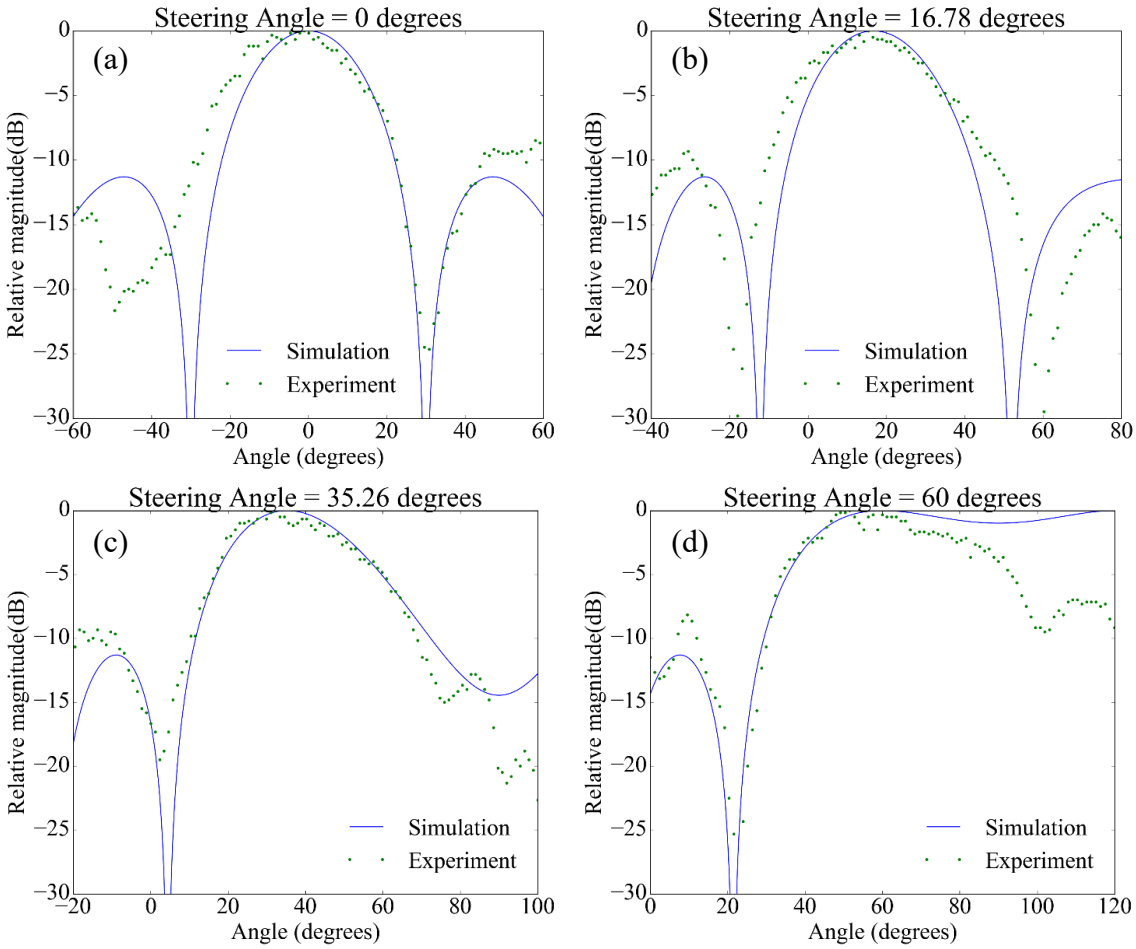

Figure 3.10: The simulated (solid curve) and measured (dotted curves) far-field radiation patterns from the 1x4 X-band PAA when the elements are configured to steer at (a) 0 degrees, (b) 16.78 degrees, (c) 35.26 degrees, and (d) 60 degrees.

3.5 SUMMARY

Utilizing the etch-free and roll-to-roll compatible fabrication process for fabricating very large-area polymer photonic systems utilizing large-area imprinting and inkjet printing processes, we developed a 2-bit TO TTD module in this work. From a fabricated basic TTD module, time delays of 0.64 ps, 10.74 ps, 22.90 ps, and 35.39 ps are measured for $0\Delta\tau$, $1\Delta\tau$, $2\Delta\tau$, and $3\Delta\tau$ configuration, respectively. A 1x4 X-band PAA system is setup and RF beam steering at 0°, ±16.78°, ±35.26°, and ±60° is demonstrated. Thus, our R2R compatible process holds great promise for scalable and low-cost manufacturing of true-time-delay feed networks for large aperture phased array antennas on rigid as well as on flexible substrates.

Chapter 4: High-speed modulator based on electro-optic polymer infiltrated subwavelength grating waveguide ring resonator

Silicon-organic hybrid integrated devices show great potential in high-speed optical interconnects and sensors. In this chapter, a high-speed modulator based on electro-optic (EO) polymer (SEO125) infiltrated sub-wavelength grating (SWG) waveguide ring resonator is presented. The core of the SWG waveguide consists periodically arranged silicon pillars along the light propagation direction, which provides large mode volume overlap with EO polymer. The optimized SWG shows a mode volume overlap of 36.2% with a silicon duty cycle of 0.7. The 3-dB modulation bandwidth of the fabricated modulator is measured to be larger than 40 GHz occupying an area of 70 μm x 29 μm, which is the largest bandwidth and the most compact footprint that has been demonstrated for the ring resonators on the silicon-organic hybrid platform.

4.1 INTRODUCTION

Silicon photonics [50,51] has been widely accepted as one of the essential technologies in the next generation optical interconnect [5,52,53]. One of the intrinsic obstacles is the absence of $\chi^{(2)}$-nonlinearity in unstrained silicon due to its centrosymmetric crystal structure, making modulating photons on silicon platform a great challenge. State-of-the-art silicon photonic modulators rely on plasma dispersion [95–97], which modulates both the real and imaginary components of the refractive index, causing undesired nonlinear response [98,99]. Although more than 50 $Gbits^{-1}$ on-off keying has been demonstrated with reverse-biased p-n junctions [100], achieving a small footprint, low power consumption, low modulation voltage and high-speed modulator is still challenging [101].

The silicon-organic hybrid (SOH) platform enables the marriage of the best of the two materials and thus has been receiving substantial attention. Compared to plasma dispersion [54], electro-optic (EO) polymers have a remarkable EO coefficient (r33 > 400pm/V) [1], ultrafast response speed (< 1 *f*s) [2–4], small dispersion, and spin-casting compatibility, which promise low-power consumption, ultra-high speed modulation, and ease of fabrication [5]. Modulators with bandwidth over 100 GHz have been demonstrated [101,102], but their millimeter long device length defeats the purpose of chip-scale integration [103–105]. Structural slow light, such as slot photonic crystals [106,107] and plasmonic devices [108,109], can effectively shrink the phase shifter size but at the price of significantly increased insertion loss [110–114]. Inspired by the success of silicon microring resonators, a few attempts have been made to replicate microrings on SOH platform [115] through several waveguiding structures [116–122]. Strip waveguides based microring resonators with EO polymer as top cladding have a radius of 40 μm [116,123]. The performance of the devices is limited by the small overlap between EO polymer and the guided mode [116,123]. Slot waveguide based ring resonators can increase the mode volume overlap significantly but suffer from an ultra-high loss of 35 dB/cm [115,124]. The diameter of the slot waveguide based ring resonator is as large as 60 μm [115].

In this paper, we report a subwavelength grating (SWG) ring resonator based modulator. Compared to slot waveguides, SWG provides competitive mode volume overlap and a comparable propagation loss as strip waveguides [125]. A 3-dB small signal modulation bandwidth larger than 40 GHz has been observed, occupying merely an area of 70 μm x 29 μm. According to the authors' best knowledge, it is the most compact and fastest ring resonator modulator that has been demonstrated on the SOH platform.

4.2 SUBWAVELENGTH GRATING WAVEGUIDE DESIGN

The schematic of SWG waveguides [126–133] is shown in Figure 4.1(a). The hybrid waveguide core is formed by periodically interlacing segments of high and low refractive index materials at a subwavelength pitch. The top and bottom claddings are EO polymer SEO125 (Soluxra LLC) and silicon dioxide, respectively. The optical mode propagates along the *z*-direction and its optical properties can be tuned by adjusting the period (*P*), waveguide width (*W*), pillar length (*L*), and Si thickness (*H*). The simulated photonic band structure of the SEO125/silicon SWG waveguides, using the 3D plane wave expansion method (RSoft, inc.), is shown in Figure 4.1(b). The black line represents the light line of SEO125 (n = 1.63). The solid and dashed lines denote even- and odd-like modes, respectively, which are categorized according to their modes with respect to the central slab plane in the *y*-direction. When the modes are away from the edge of reduced Brillouin zone, the dispersion characteristic of the guided modes resembles that of a uniform waveguide. The electrical fields $|E_x|^2$ of optical modes, which is aligned parallel to the poling direction of SEO, at *x*-slice (x = 0 μm), *y*-slice (y = 0 μm), and *z*-slice (z = 0 μm) are plotted in Figure 4.1(c), (d), and (e), respectively. It can be observed that there is a strong optical field exists outside Si pillars in the SEO125 region. The mode volume overlap integral $f = \int_{SEO125} \varepsilon |E_x|^2 dv / \int_{total} \varepsilon |E_x|^2 dv$ is adopted to quantify the optical field in SEO125.

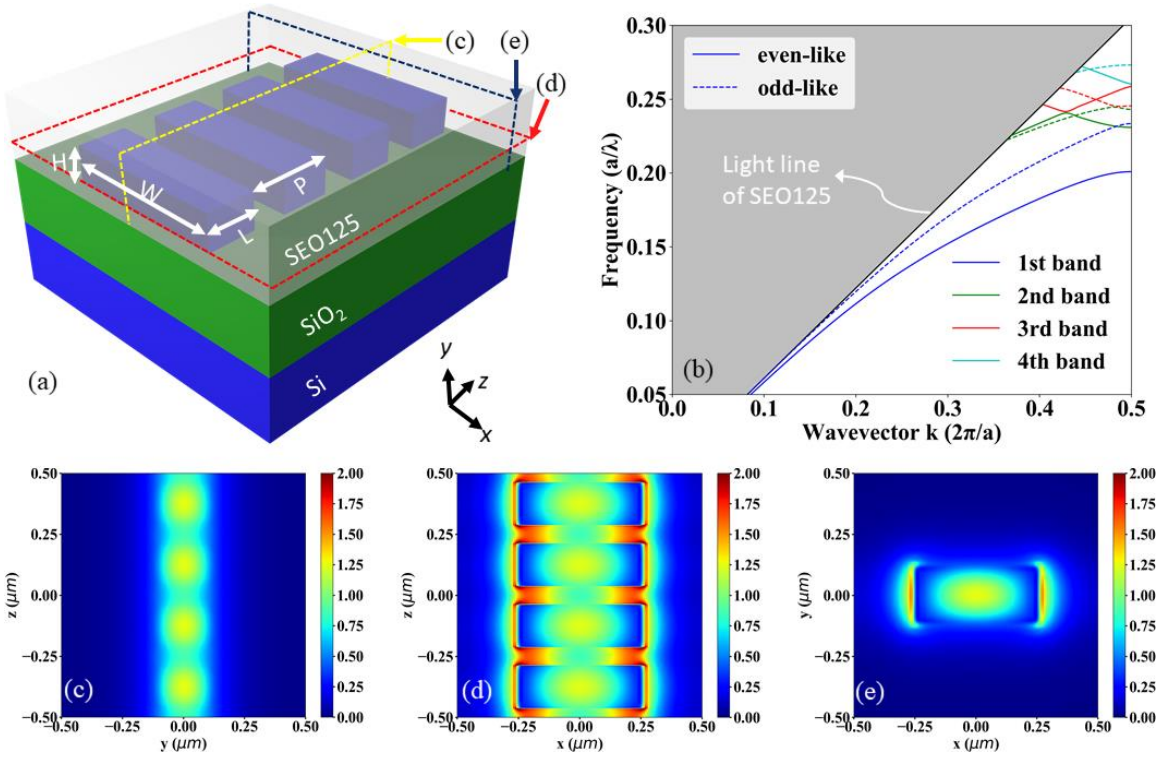

Figure 4.1: (a) Schematic of an SWG waveguide for the optical modulator. (b) Photonic band structure of SWG waveguides with SEO125 as top cladding for the waveguide width $W = 500\ nm$ and pillar length $L = 175\ nm$. The y-axis on the right side is the wavelength λ corresponding to the period $P = 250\ nm$. The black line at the boundary of the grey region indicates the light line of SEO125. The solid and dashed lines indicate the even-like and odd-like modes respect to the central slab plane in the y-direction, respectively. The electrical field distribution of the SWG waveguide at (c) x-slice ($x = 0\ \mu m$), (d) y-slice ($y = 0\ \mu m$), and (e) z-slice ($z = 0\ \mu m$), for the SWG waveguide width $W = 500\ nm$, pillar length $L = 175\ nm$, height $H = 220\ nm$, and period $P = 250\ nm$.

The mode volume overlap factor f in SEO125 region, effective index, and group index of the SWG waveguides versus the waveguide width W and the duty cycle ($= L/P$) are calculated and shown in Figure 4.2(a), (c) and (e), respectively. The overlap factor in SEO125 region, effective index, and group index versus the duty cycle for several

waveguide widths are shown in Figure 4.2(b), (d) and (f), respectively. As the waveguide width or duty cycle decreases, the overlap factor increases, while both effective and group index decreases. This indicates more optical energy of the SWG waveguides is concentrated inside SEO125, which has lower refractive index 1.637 comparing to that of silicon 3.476.

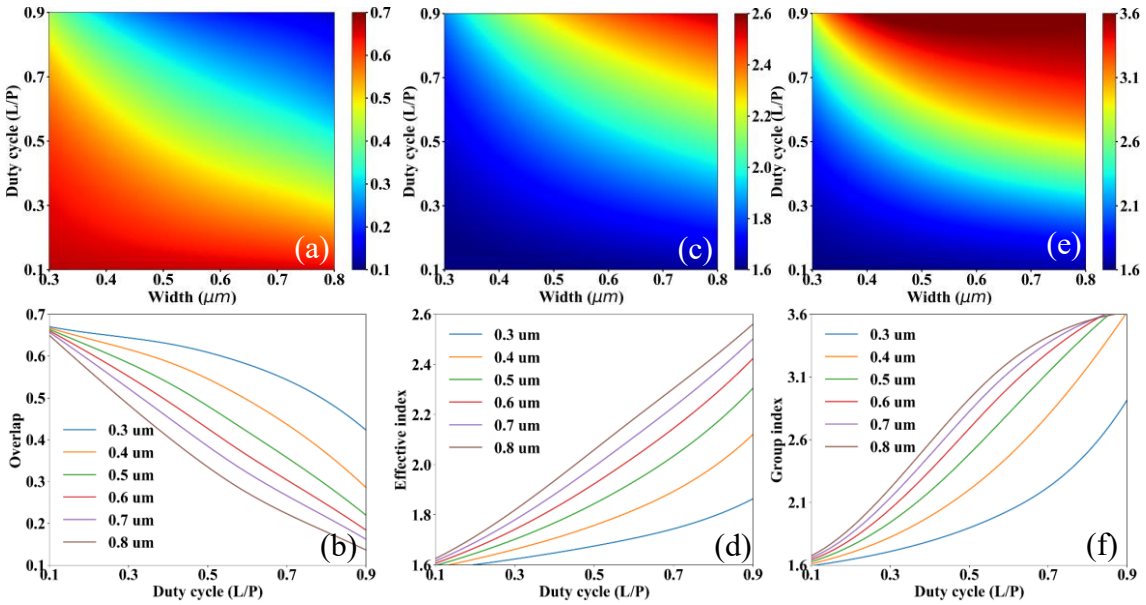

Figure 4.2: (a) Mode volume overlap integral factor in SEO125 region, (c) effective index, and (e) group index of SWG waveguides versus the waveguide width and the duty cycle (= L/P) at period P = 250 nm. (b) Overlap factor in SEO125, (d) effective index, and (e) group index of SWG waveguides versus the duty cycle (= L/P) for several waveguide widths at period P = 250 nm.

The overlap factor in SEO125 region, effective index, and group index of the SWG waveguides versus the SWG period and duty cycle are calculated and shown in Figure 4.3(a), (c), and (e), respectively. The overlap factor in SEO125 region, effective index, and group index versus the duty cycle for several SWG periods are shown in Figure 4.3(b), (d),

and (f), respectively. As the SWG period or duty cycle decreases, the overlap factor increases, while both effective and group index decreases. It can be seen that the SWG period doesn't affect the SWG waveguides much if the sub-wavelength condition ($p < \lambda/4$) is satisfied, where λ is wavelength inside the waveguide.

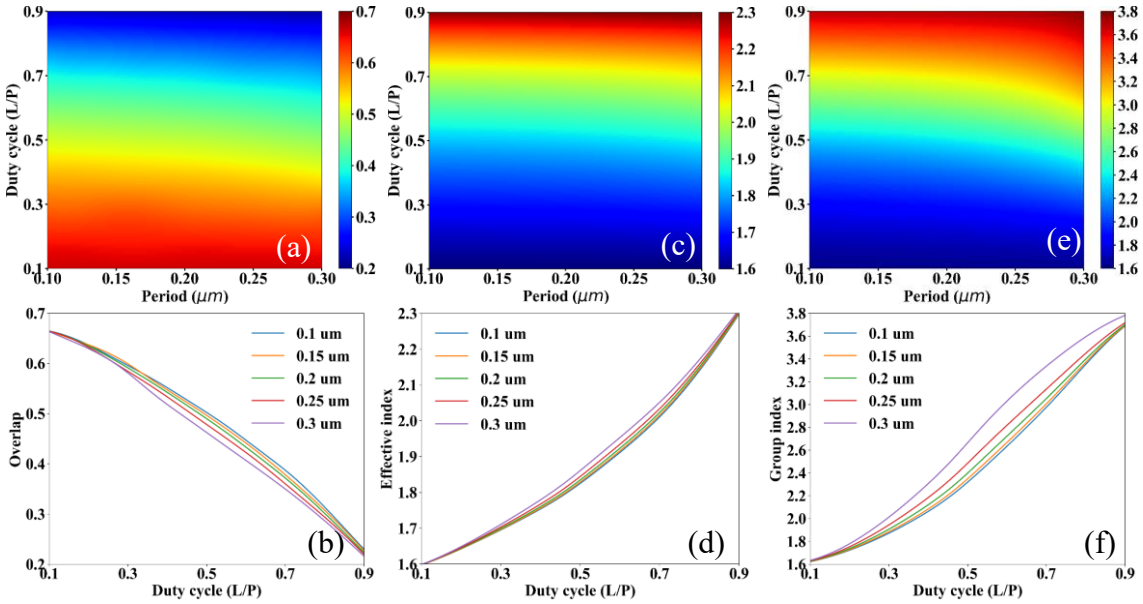

Figure 4.3: (a) Overlap factor in SEO125 region, (c) effective index, and (e) group index of SWG waveguides versus the SWG period and the duty cycle (= L/P) at waveguide width W = 500 nm. (b) Overlap factor in SEO125, (d) effective index, and (e) group index of SWG waveguides versus the duty cycle (= L/P) for several SWG periods at waveguide width W = 500 nm.

We analyzed the mode volume overlap factor f, effective index, and group index of the SWG waveguides versus the duty cycle (= L/P), the waveguide width W, and SWG period (P), as shown in Figure 4.2 and Figure 4.3. As SWG duty cycle, the waveguide width W, or SWG period decreases, mode volume overlap factor f increases, meaning that more electrical energy is concentrated inside SEO125 region. It can also be seen that the

period does not affect the SWG much, if the subwavelength condition ($p < \lambda/4$) is satisfied, where λ is the wavelength inside the waveguide. In this chapter, SWG is optimized to operate at λ_0 = 1565 nm, and we will focus on the fundamental TE-like mode (blue solid line in Figure 4.1(b)). To ensure the SWG structure operates in the subwavelength regime and ease of fabrication, we choose the period P = 250 nm, and the pillar length L = 175 nm, corresponding to a duty cycle of 0.7, along with the waveguide width W = 500 nm. In this configuration, the mode volume overlap integral f equals 36.2%. Compared a typical strip waveguide (f ~ 4.0%), it increases around 9 times.

4.3 SUBWAVELENGTH GRATING WAVEGUIDE RING RESONATOR DESIGN AND OPTIMIZATION

The proposed SWG ring resonator based modulator is shown in Figure 4.4(a). Subwavelength grating couplers are exploited for interfacing single mode fibers [134,135]. The rounded rectangular shape is adopted instead of the most common circular shape to gain more flexibility in tuning the coupling strength between the bus waveguide and the ring resonator. The zoomed-in schematic of the SWG ring resonator is shown in Figure 4.4(b). The shape of the ring resonator is defined by the coupling length L_c, phase shifter length L_a, and bending radius R, which are 9 µm, 50 µm, and 10 µm, respectively. The SWG ring resonator is formed by the SWG waveguide [130,133] optimized in the previous paragraph except for the four bends at the corners, in which trapezoidal shape pillars are fine-tuned to minimize the bending loss [136,137]. SU-8 island is used to isolate the center electrode and ring resonator. The n_{eff} of the SWG waveguide with SEO125 and SU8 cladding is 2.031 and 1.994, respectively. The reflection between two waveguides is merely 0.0085%. Thus, the influence of using SU-8 island can be ignored. Due to the compact size, the walk-off between electrical and optical signal is negligible. Thus, high-

speed modulation can be readily achieved with lumped electrodes [41]. It has been proved that without 50 Ω termination, lumped electrodes can effectively reduce the power consumption compared to traveling wave electrodes [39,138]. To reduce the reflection of RF signals, ground-signal-ground (GSG) electrodes are designed and optimized with Ansys HFSS to provide 50 Ω impedance match with GSG RF probes. As shown in Figure 4.4(b), the central width, gold thickness, and gap are 25 μm, 2.4 μm, and 4 μm respectively. The detailed simulation process can be found in Figure 4.5.

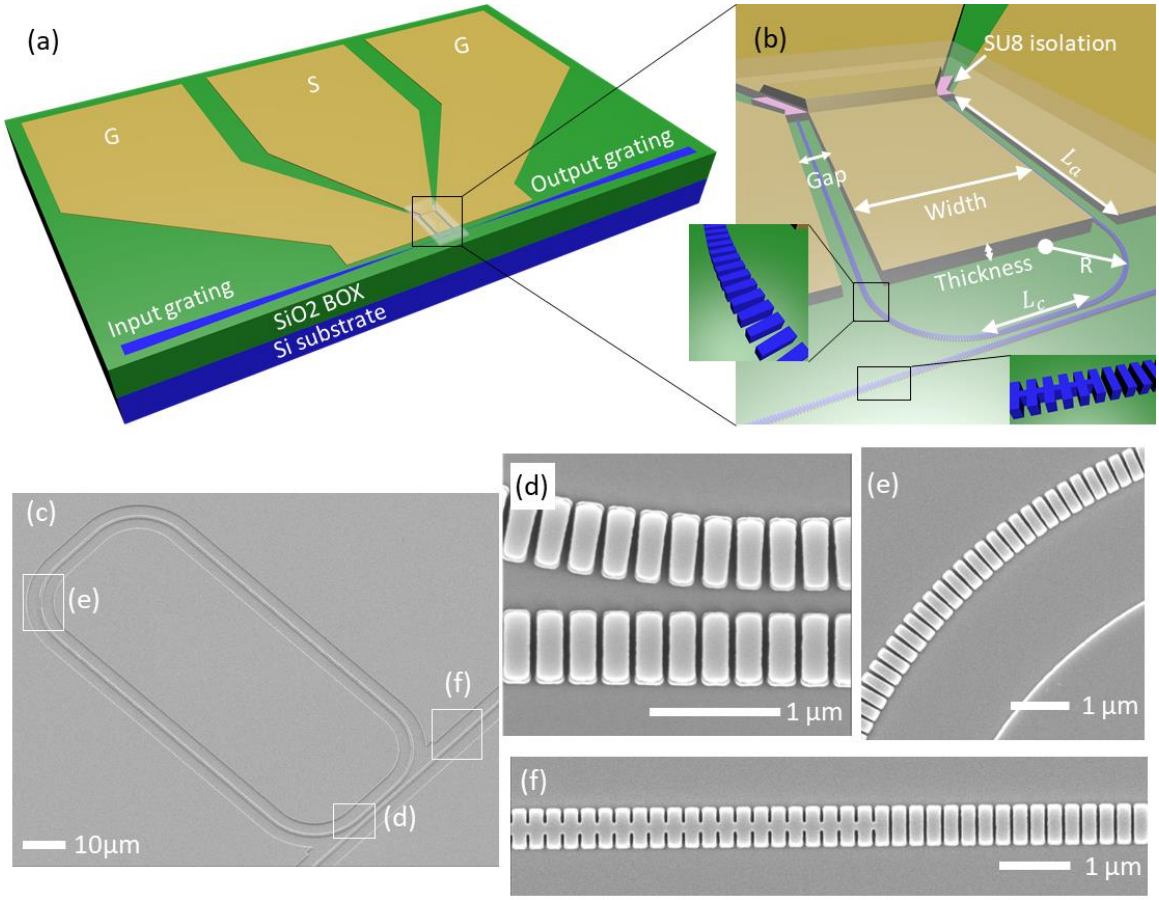

Figure 4.4: (a) Schematic of an EO polymer modulator based on the SWG ring resonator. The device is fabricated on a silicon-on-isolator (SOI) wafer. The input and output grating couplers are used to couple the light into and out of the device, respectively. The "G", "S", and "G" electrode pads are used to connect with a GSG high-speed RF probe, which is used to provide the RF signal to modulate the EO polymer modulator based on the SWG ring resonator. (b) The zoomed-in schematic of the SWG ring resonator. SWG is used for both the ring and the bus waveguide. The trapezoid SWG is used at the SWG bends to reduce the bending loss. A converter is used to convert between the conventional strip mode and SWG mode. SU-8 island is used to isolate the center electrode and ring resonator. The transparent region in (a) and (b) indicates the coated EO polymer. SEM images of the fabricated SWG ring resonator (c) and zoomed in images (d) (e) and (f).

The impedance of the electrodes versus the RF signal frequency & the central width, thickness, and gap are calculated and shown in Figure 4.5(a), (c), and (e), respectively. The impedance versus the RF signal frequency for several central widths, thickness, and gaps are shown in Figure 4.5(b), (d), and (f), respectively. As the central width decreases, thickness decreases, or gap increases, the impedance increases. The impedance is almost flat at 50 Ω when central width, thickness, and gap are 25 µm, 2.4 µm, and 4 µm, respectively. Thus, the optimized optical coupling length L_c is decided by $L_c = width - 2 \times R + Gap$, which equals 9 µm.

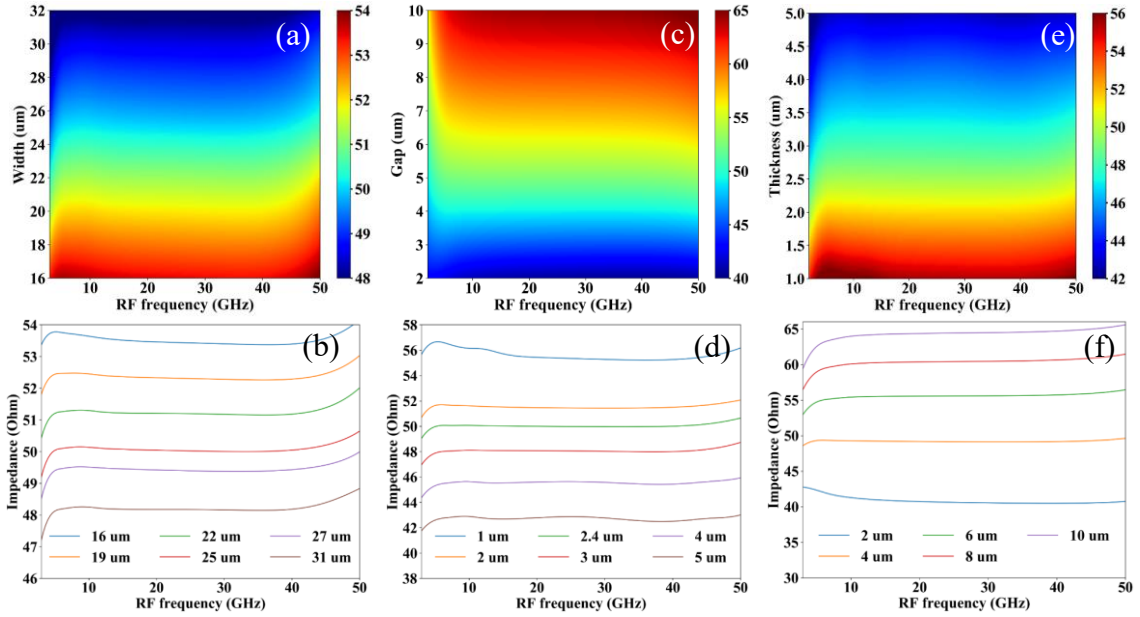

Figure 4.5: (a) The impedance of the electrodes versus RF frequency and central width for electrode thickness 2.4 µm and gap 4 µm. (b) The impedance of the electrodes versus RF frequency at several central widths for electrode thickness 2.4 µm and gap 4 µm. (c) The impedance of the electrodes versus RF frequency and thickness for central width 25 µm and gap 4 µm. (b) The impedance of the electrodes versus RF frequency at several thicknesses for central width 25 µm and gap 4 µm. (e) The impedance of the electrodes versus RF frequency and gap for central width 25 µm and thickness 2.4 µm. (f) The impedance of the electrodes versus RF frequency at several gaps for central width 25 µm and thickness 2.4 µm.

4.4 HIGH SPEED MODULATOR FABRICATION

The modulator is fabricated on a silicon-on-isolator (SOI) chip. The SWG ring resonator is patterned by e-beam lithography and reactive ion etching (RIE). A 2.6 μm thick SU-8 island is formed by photolithography to let the electrodes cross over the SWG waveguide without causing any optical loss. Then the electrodes are fabricated with the standard liftoff process. Finally, EO polymer is spin-casted and cured under 80°C for 5 hours in the vacuum oven to assure the entire subwavelength structures are infiltrated. The detailed fabrication procedure can be found in Figure 4.6. The SEM of the fabricated SWG ring resonator is shown in Figure 4.4(c-f).

4.4.1 Device fabrication

The SWG ring modulator is fabricated on a silicon-on-isolator (SOI) chip. The fabrication procedures are listed in the following: (1) The SWG ring resonator is patterned by e-beam lithography and etched by RIE. (2) The silicon region underneath the electrodes is defined by photolithography and etched by RIE, as shown in Figure 4.6(a). (3) The SU-8 island is formed by photolithography to let the electrodes cross over the SWG waveguide without causing any optical loss, as shown in Figure 4.6(b). (4) The electrodes are fabricated by e-beam evaporation and standard lift-off process, as shown in Figure 4.6(c). (6) The SEO125 is coated, cured, and poled.

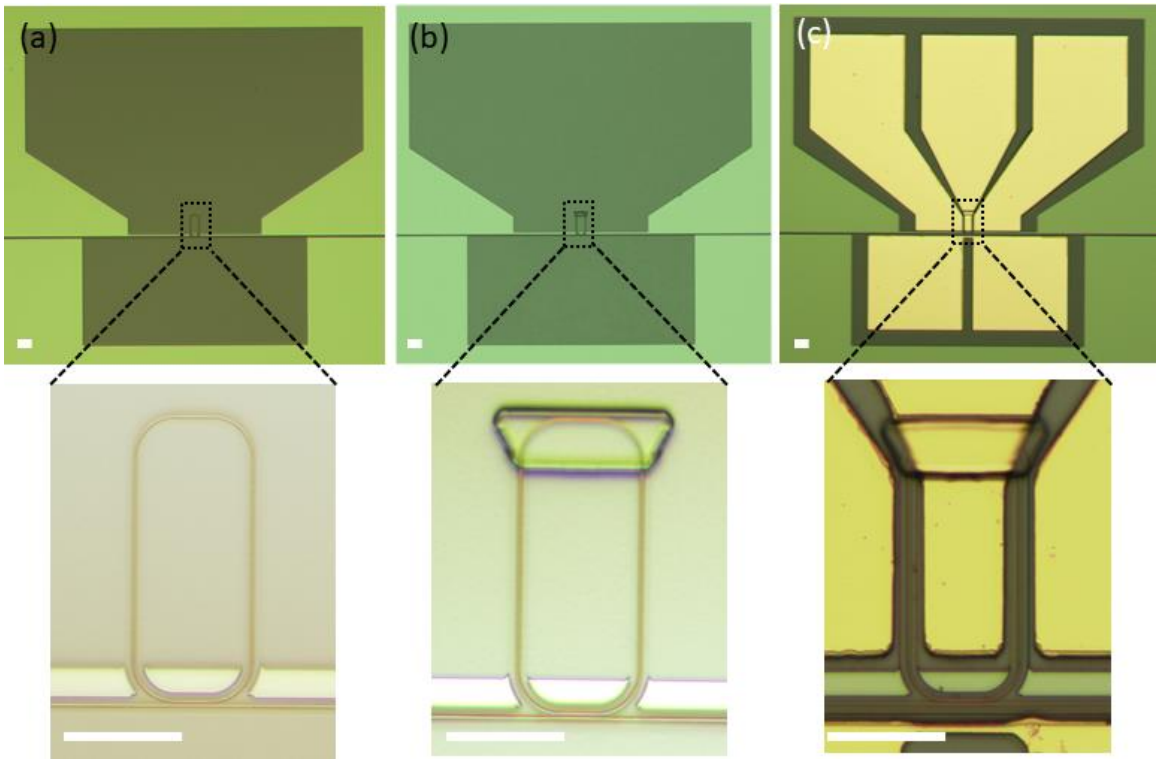

Figure 4.6: (a) The SWG ring modulator is patterned by e-beam lithography and etched by RIE. (b) The SU-8 island is formed by photolithography to let the electrodes cross over the SWG waveguide without causing any optical loss. (c) The electrodes are fabricated by e-beam evaporation and standard lift-off process. The upper and lower images are the whole device and zoomed in at the ring resonator, respectively. The white bar at left-bottom corner indicates the length of 30 μm.

4.4.2 Electric-optical polymer poling

For electro-optical (EO) polymer device, EO polymer poling is one of the most important steps. The EO-polymer is poled at 150°C for 1 minute to align the chromophore molecules, and then the temperature slowly reduces to the room temperature for the following measurements. During this poling process, the leakage current is monitored. The

smaller leakage current indicates higher poling field across the EO polymer, that is, higher poling efficiency. At first the EO polymer are randomly aligned. When the hotplate is heated to 150 °C, the EO polymer reaches its glass transition temperature, thus EO polymer are aligned under the applied DC voltage. Even after the temperature is reduced, the aligned EO polymer will keep aligned. As seen in Figure 4.7, the maximum leakage current is around 1.5 nA, which indicates a high poling efficiency.

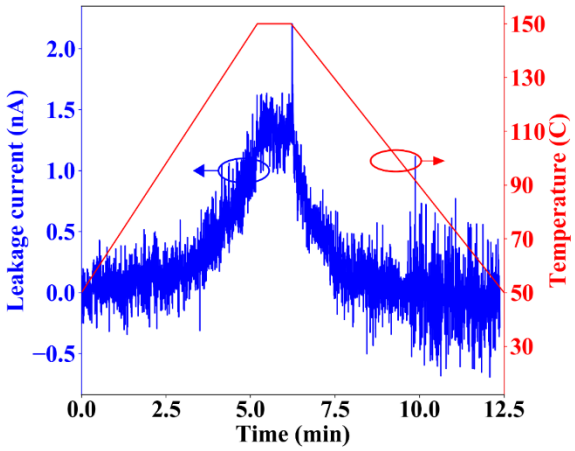

Figure 4.7: The leakage current and poling temperature versus the poling time.

4.5 Results and Discussion

The transmission of the fabricated SWG ring resonator is characterized by amplified spontaneous emission (ASE) broadband optical source and optical spectrum analyzer (OSA) [134,135]. To maximize the extinction ratio, a set of devices with different gaps are fabricated and measured. The spectra are summarized in Figure 4.8(a). The relation between the extinction ratio and the gap is extracted and plotted in Figure 4.8(b). The maximum extinction ratio is 25.9±3.5 dB, corresponding to an edge-to-edge gap of

500 nm between the bus waveguide and the ring resonator. The on-chip insertion loss of the modulator is around 4 dB.

The extinction ratio decreases drastically to ~10 dB due to the scattering centers formed by non-uniform refractive index of the EO-polymer induced during poling [139–141]. To characterize the poling efficiency, DC voltage is applied to the electrodes with a configuration shown in the inset of Figure 4.8(c). The red shift of the resonance is observed and plotted in Figure 4.8(c). The resonance shift versus the applied voltage is summarized in Figure 4.8(d). The orange solid line is the linear fitting of the measurement data, giving an averaged resonance shift of 41.3 pm/V. Thus, from the electro-optic effect $\Delta n = \frac{1}{2} r_{33} n^3 \frac{V}{d}$ [142], the EO coefficient is estimated to r_{33} = 54.7 pm/V, corresponding to a poling efficiency of 43.8% compared to the EO coefficient of the bulk EO polymer.

The setup to measure the optical response and side-lobe of the modulator is shown in Figure 4.8(e). The blue and red lines indicate the optical and RF signal, respectively. The top and bottom dashed boxes are used to measure the S21 response and side-lobes, respectively. The single wavelength light is generated by a tunable laser (Santec ECL200). A polarization maintaining fiber (PMF, OZ Optics PMF-1550-8/125-0.25-L) is used to couple the light into the modulator. The light from the output grating coupler is collected by a standard single mode fiber (SMF, Corning SMF-28) [134,135]. The RF signal, which is output from the port #1 of the vector network analyzer (VNA, Agilent N5230A), is applied to the sample via a GSG probe (Cascade ACP40-GSG-250). The aligned grating couplers and the applied GSG probe is shown in Figure 4.8(f). For the S21 response measurement, a high-speed photodiode (New Focus 1014 45-GHz) converts the optical signal into the RF signal, which is fed into the port #2 of the VNA. For the side-lobe measurement, the output optical signal from SMF is directly connected to the optical spectrum analyzer (OSA, ANDO AQ6317B).

The measured and normalized optical response of the SWG optical modulator is shown in Figure 4.8(g). The optical response is measured at the rising edge of the resonance, which is the black dashed line in Figure 4.8(c). The reflection from port #1 is subtracted during normalization. The measured 3-dB bandwidth is 41.4 GHz, and the 6-dB bandwidth is 44.1 GHz. The measured optical transmission spectra of the modulator operating at 8-26 GHz, as shown in Figure 4.8(h). The modulation index versus frequency is shown in Figure 4.8(i). The modulation index results are normalized to a 10 dBm launch power. The observed small signal bandwidth is limited by our measurement instruments (e.g. 2.92mm RF cables have a 3-dB bandwidth of 40 GHz). The potential bandwidth can be estimated by $\frac{1}{f_c^2} = \frac{1}{f_{\tau_p}^2} + \frac{1}{f_{RC}^2}$, where f_{τ_p} and f_{RC} denote the photon lifetime and RC delay determined cutoff frequencies, respectively [143]. Since the Q factor of the resonator is ~1000 after poling, corresponding to a photon lifetime of ~0.83 ps, the photon lifetime induced cut-off frequency $f_{\tau_p} = \frac{1}{2\pi\tau_p} = 192$ GHz. The equivalent circuit of the modulator is shown in the inset of Figure 4.8(i). As the modulator is directly driven by the electric field between the gold electrodes with negligible resistance, f_{RC} is infinite. The cutoff frequency is therefore determined by photon lifetime. Basic on this analysis, the modulator can potentially operate at 192 GHz [143].

As aforementioned, due to the compact device footprint, lumped electrodes without termination are used to apply electrical signals. The power consumption is equivalent to charging and discharging two capacitors. The total capacitance [117] is estimated to be 0.4 *f*F. According to Figure 4.8(c), assuming V_{pp} = 5.0 V is selected, which corresponds to a 6 dB on-off ratio, the power consumption can be estimated by $\frac{1}{4}CV^2$ = 2.5 *f*J/bit, assuming equal probabilities of logical ones and zeros and only transitions consume energy. The power consumption can be further improved by reducing the capacity, which can be readily achieved by reducing the size of the ring.

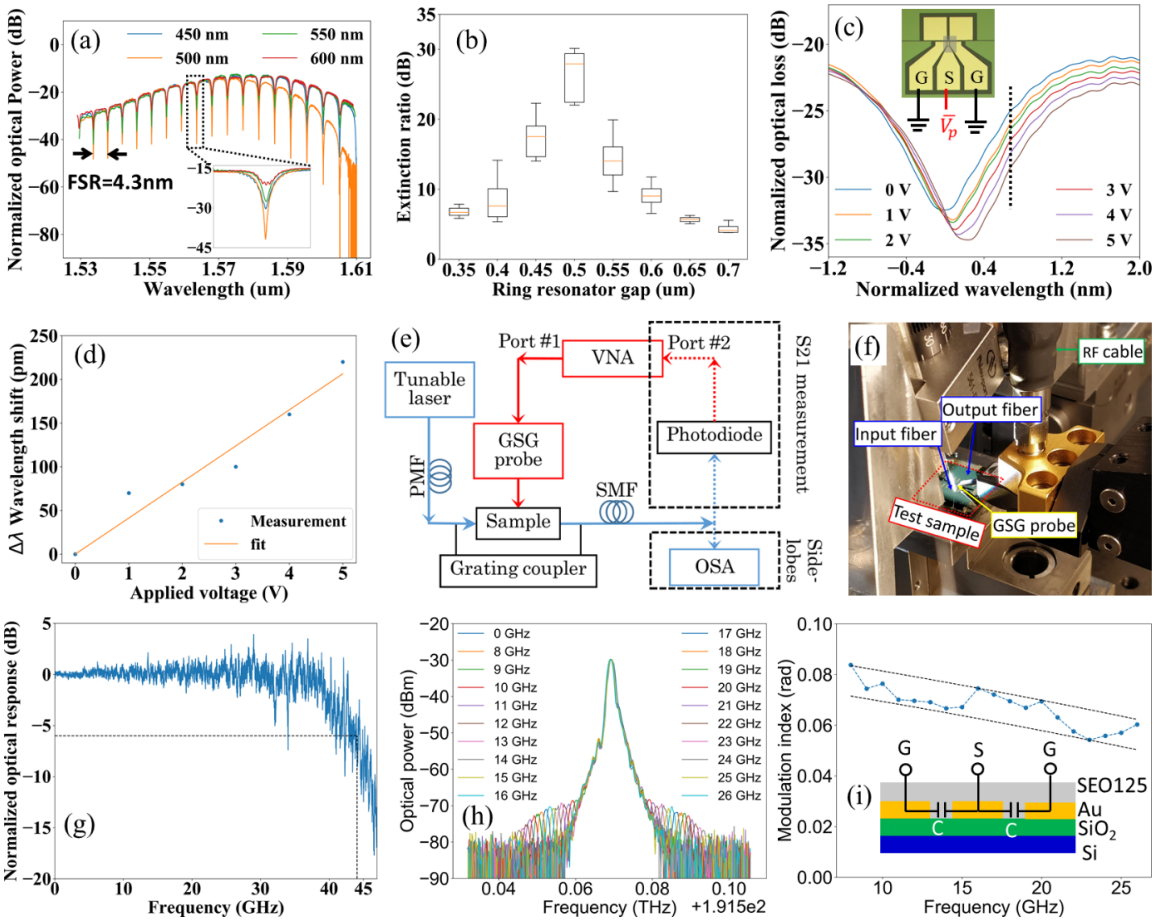

Figure 4.8: (a) The normalized optical spectrums with the gap size 450 *nm*, 500 *nm*, 550 *nm* and 600 *nm*. (b) The measured extinction ratio versus the gap size between the bus and the ring. (c) The spectrum resonance shift after applied the electric field. The DC voltage is applied to the electrodes with a configuration in the insert. (d) the wavelength shift in picometer versus the applied electrical voltage. (e) The setup to measure the RF response and side-lobe of the modulator. The blue and red lines indicate the optical and RF signal, respectively. The top and bottom dashed boxes are used to measure the S21 response and side-lobes, respectively. (f) The magnified view of the sample connected with fibers using the grating coupler and RF cables using the GSG probe. (g) The measured and normalized optical response versus the frequency. (h) The measured optical transmission spectra of the modulator operating at 8-26 GHz. (i) The modulation index versus frequency. The modulation index results are normalized to a 10 dBm launched power. The equivalent circuit of the modulator is shown in the insert.

4.6 SUMMARY

We have demonstrated the first high-speed optical modulator based on electro-optic polymer infiltrated subwavelength grating waveguide ring resonator. Compared to a conventional strip waveguide, SWG structure increases the interactive volume between the optical signal and EO polymer. The measured 3-dB bandwidth is larger than 40 GHz. The power consumption for digital communication is 2.6 *f*J/bit. The bandwidth can be further increased, and the power consumption can be further decreased by reducing the duty cycle or the size of the ring resonator.

Chapter 5: On-chip time-division multiplexing and de-multiplexing system

Significate effort in integrated photonics has been put in recent years into further increasing the bandwidth of the high-speed optical communication. Most of them are based on the wavelength-division multiplexing (WDM). However, such WDM system has more carrier wavelengths, which increases the complexity and reduce the non-regeneration distance. In this chapter, the 50 GHz optical time-domain multiplexing and de-multiplexing system is designed based on IMEC iSiPP50G platform. The multiplexing system combines 4 channels of 12.5 GHz RF signals to a 50 GHz optical signal. The de- multiplexing system converts the 50 GHz multiplexed optical signal back to 12.5 GHz RF signal.

5.1 INTRODUCTION

The rapid growth of telecommunication networks and data transportation technology have attracted a lot of research interest in high-speed optical and electronic devices and systems. Especially, optical fiber communication becomes more and more important for the data center, 5G mobile network, internet of thing (IoT), etc. [144] because of its advantages over electrical communication, such as transmission capacity, high security, low power consumption, low cost, low cross-talk, and low EMI.

A straight forward approach to increase the bandwidth is to increase the number and density of the carrier wavelength in the wavelength division multiplexing (WDM) system [145] or mode-division multiplexing (MDM) [146]. However, such a system has a very complex system and significantly reduced the non-regeneration distance [147]. To simply the system and increase the bandwidth, I have designed the optical time-domain multiplexing and de-multiplexing system [148] in this chapter. The time-domain

multiplexing and de-multiplexing system uses only one wavelength 1.55 um, which greatly simplifies the system.

5.2 RING RESONATOR

To demonstrate the multiplexing and de-multiplexing system, a ring resonator from IMEC is used as the building block. The layout of such a ring resonator can be found in Figure 5.1. This ring has a radius of 5 um with a gap size 150 um between ring and bus waveguide. The FSR (free spectral range) and Q-factor is 19.2 nm and 2200, respectively. The measured S21 3dB bandwidth is 47 GHz.

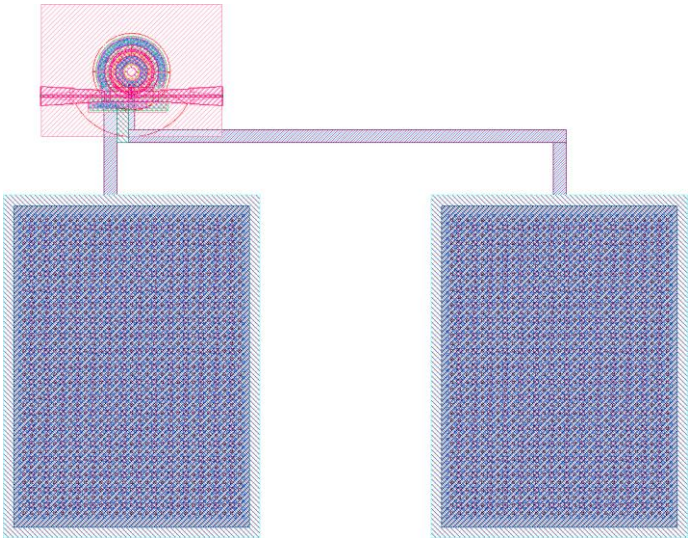

Figure 5.1: The layout of a ring resonator. The size of the electrical pads is 60um * 80um.

To study the properties of this ring resonator, Lumerical INTERCONNECT with IMEC CML library is used for the simulation. The schematic of the setup to simulate the resonance shift of a ring resonator is shown in Figure 5.2(a). The optical network analyzer (ONA_1) is used to supply an optical signal to the ring resonator and analyze the output

signal. The DC power supply (DC_cathode) fixes at 0 V, and another DC power supply (DC_anode) is set a negative voltage for the reverse bias of the ring resonator. The output signal received by the optical network analyzer is shown in Figure 5.2(b).

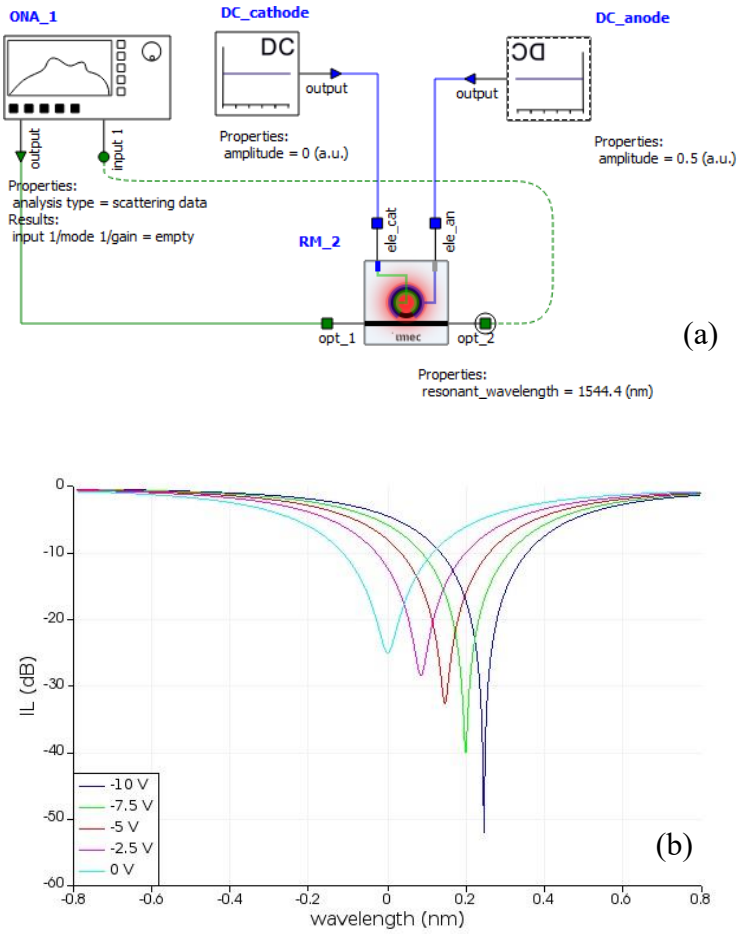

Figure 5.2: (a) Schematic to simulate a ring resonator using Lumerical INTERCONNECT and IMEC CML library. (b) The resonance shift of a ring resonator with reverse bias voltage.

5.3 TIME-DIVISION MULTIPLEXING SYSTEM

The schematic of optical time-domain multiplexing (MUX) system is illustrated in Figure 5.3. In the multiplexer, light from a distributed feedback (DFB) laser is split into 4 channels. Each channel is modulated by the 12.5 GHz electrical signal. The pulse train from a pulse generator with 12.5 GHz repetition rate and 20 ps pulse width is also split into 4 channels and a time delay of 20(n-1) ps is introduced into channel n. The pulse train is used to periodically turn on the high-speed switch and couple the 12.5 GHz signal into the bus waveguide while reducing the signal duration from 80 ps to 20 ps and adding a time delay of 20(n-1) ps. A 50 GHz signal is obtained by combining all the signals of 4 channels with time delay spacing of 20 ps.

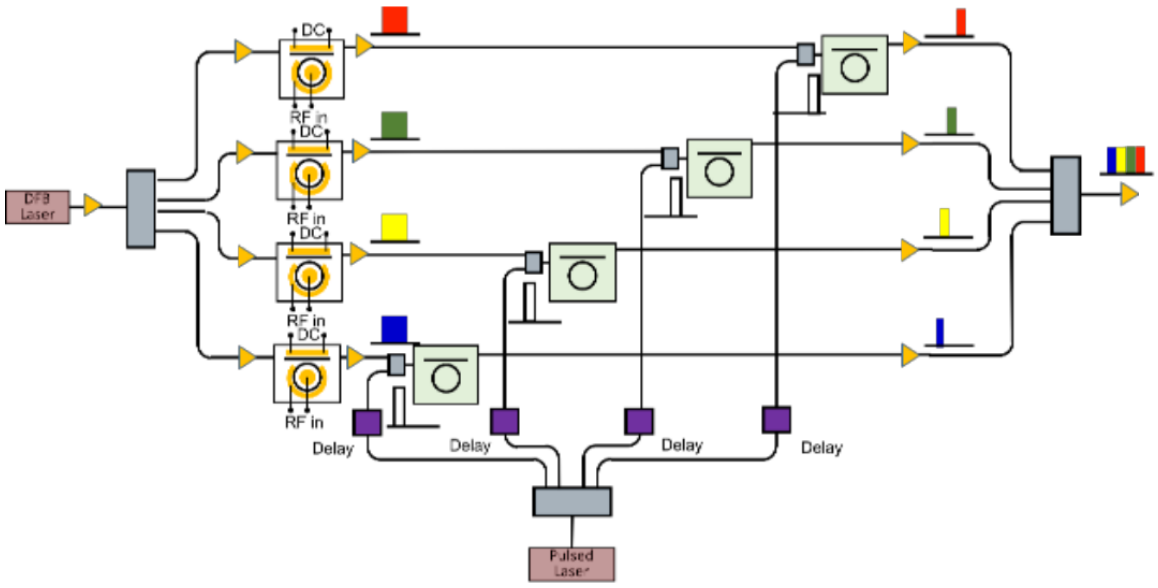

Figure 5.3: Optical time-domain multiplexing system.

The layout of such an optical time-domain multiplexing system is shown in Figure 5.4(a). The grating couplers are arranged at one side for the fiber array. There is one LO

(local oscillator) optical input, four optical inputs for optical switches, four GS RF inputs for ring modulators, and one optical output. Three 1x2 Multimode Interference (MMI) is used for power splitting and three Y-branches are used for power combining. For the initial demonstration, the optical switches are replaced as optical ring modulators, as shown in Figure 5.4(b).

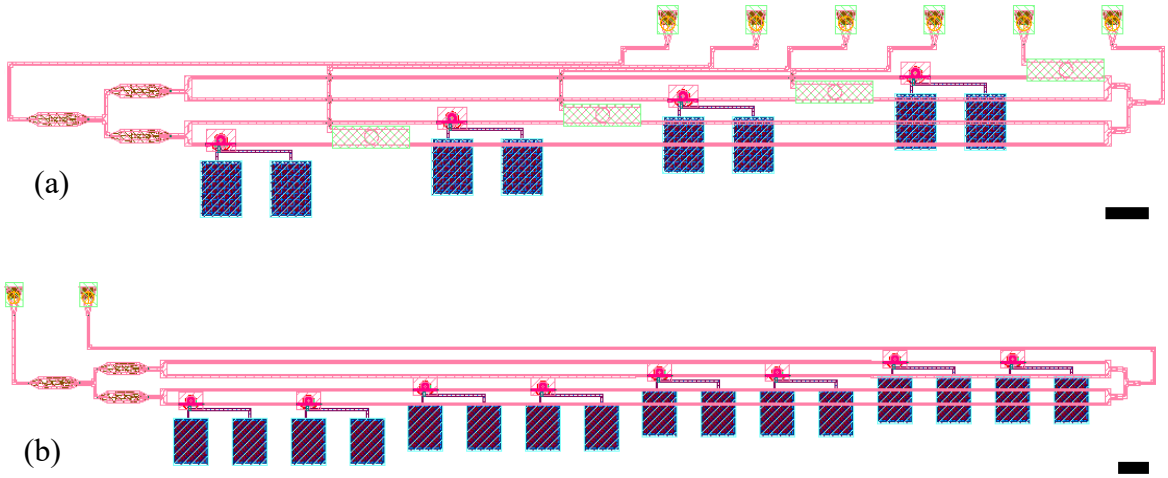

Figure 5.4: (a) The layout of an optical time-domain multiplexing system using all optical switches. (b) The layout of an optical time-domain multiplexing system, which replaces the all optical switches as ring modulators. The black bar at right-bottom corner indicates a length of 60 um.

An optical time-domain multiplexing system is simulated by Lumerical Interconnect. The digital PRBS signals of path 1-4 are loaded from 4 random sequences, then the electrical signals for optical modulators are converted from the corresponding PRBS signals. Then, the switches are used to select the corresponding channel. Grating couplers are used to input the local oscillator signal and output the multiplexed signal. The schematic of the simulation is shown in Figure 5.5.

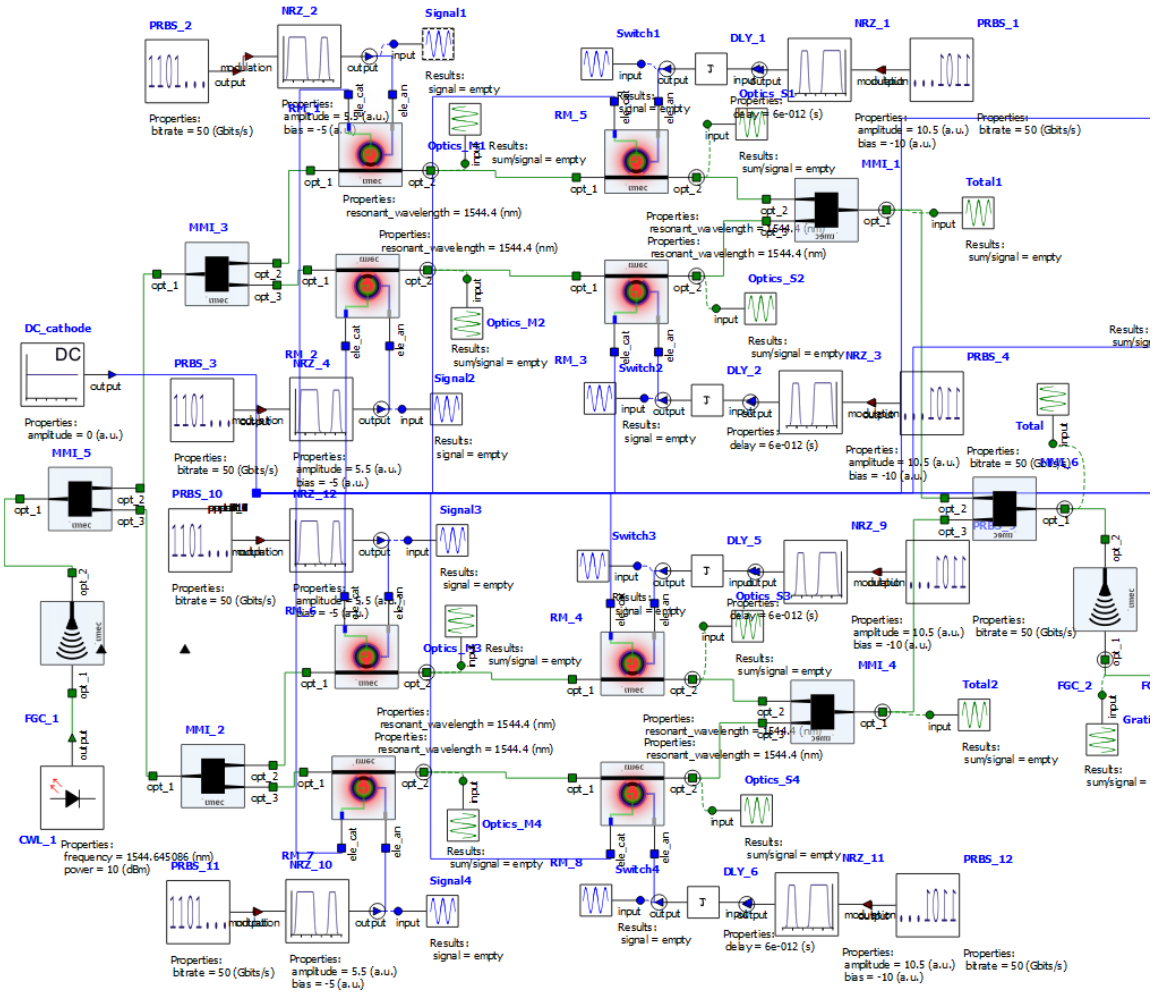

Figure 5.5: Schematic to simulate an optical time-domain multiplexing system using Lumerical INTERCONNECT and IMEC CML library.

The waveform of the signal through the optical time-domain multiplexing system is calculated using Lumerical Interconnect. The waveform for channel 1, 2, 3 and 4 is shown in Figure 5.6, Figure 5.7, Figure 5.8, and Figure 5.9, respectively. The signal 1-4 is generated as the random 1-bit number series. The optics M1-4 is the optical signal modulated by the random number series. The switch 1-4 is the 50 GHz pulse with 20 ps

pulse width and 20(n-1) ps delay for channel n. The optics CH1-4 is the corresponding optical signal after switching for each channel.

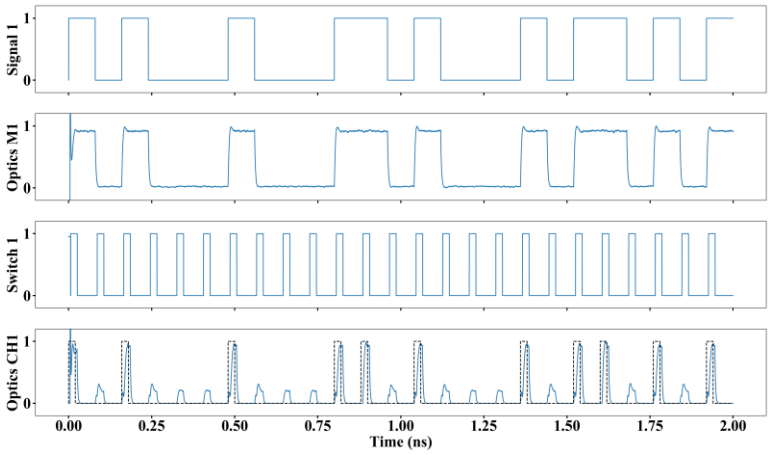

Figure 5.6: The waveform for channel 1 of the optical time-domain multiplexing system with the random signal as the input signal for modulators.

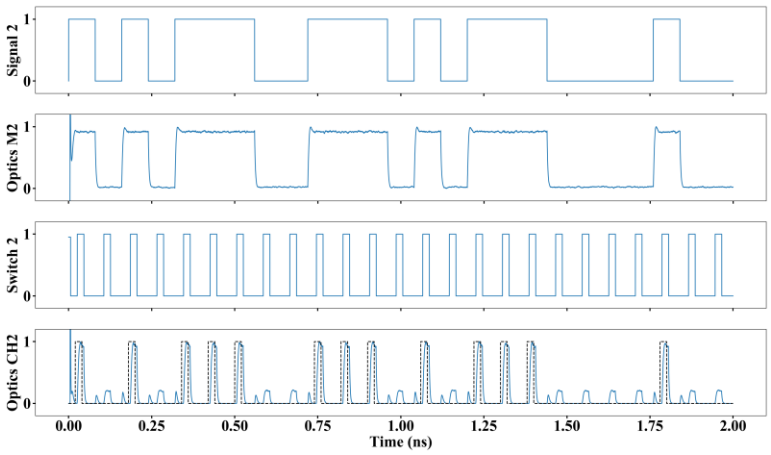

Figure 5.7: The waveform for channel 2 of the optical time-domain multiplexing system with the random signal as the input signal for modulators.

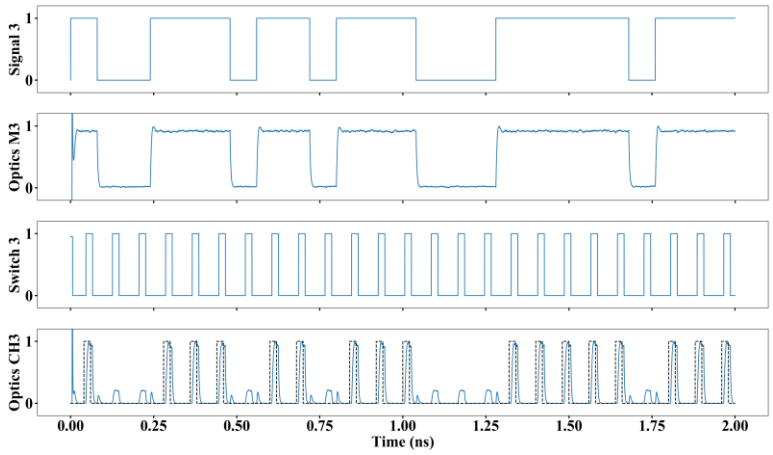

Figure 5.8: The waveform for channel 3 of the optical time-domain multiplexing system with the random signal as the input signal for modulators.

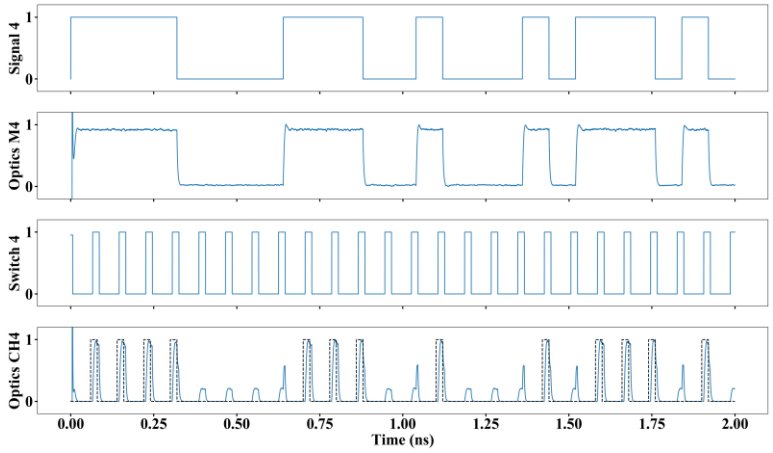

Figure 5.9: The waveform for channel 4 of the optical time-domain multiplexing system with the random signal as the input signal for modulators.

The last step for the multiplexing system is combining all the channel together, which waveform is shown in Figure 5.10. Figure 5.10(a-d) are the signal from each channel in Figure 5.9. Figure 5.10(e) and Figure 5.10(f) are the combined signal of CH1+CH2 and

CH3+CH4, respectively. The resulted multiplexed signal is shown in Figure 5.10(g), which is CH1+CH2+CH3+CH4.

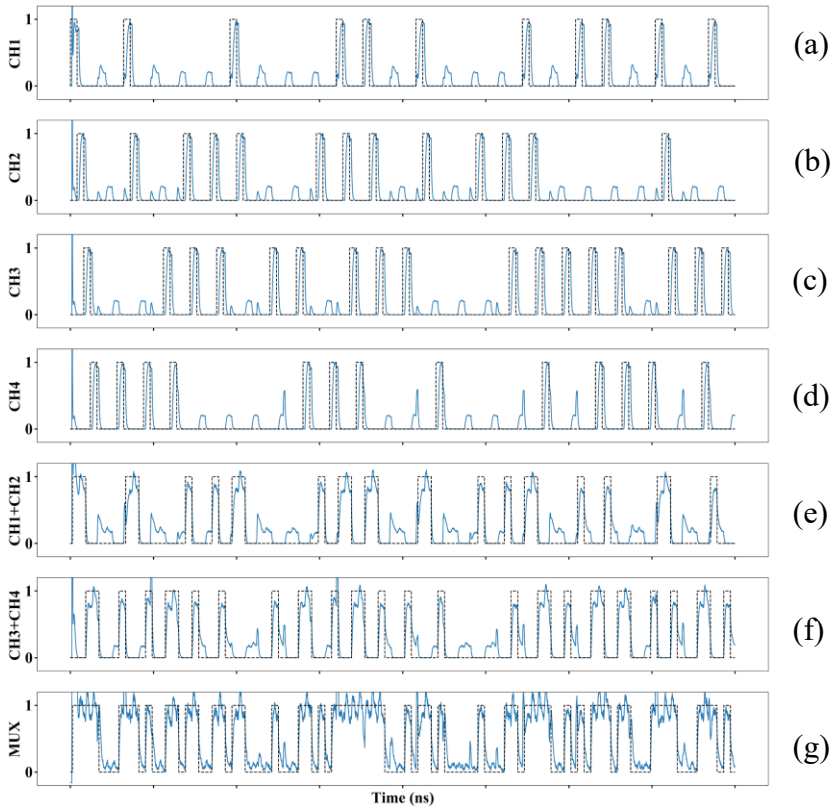

Figure 5.10: The waveform for (a) channel 1, (b) channel 2, (c) channel 3, (d) channel 4, (e) combining channel 1 and channel 2, (f) combining channel 3 and channel 4, and (g) the multiplexed signal (combining channel 1-4) of the optical time-domain multiplexing system.

5.4 TIME-DIVISION DE-MULTIPLEXING SYSTEM

The schematic of optical time-domain de-multiplexing (DEMUX) systems are illustrated in Figure 5.11. The de-multiplexing is the reverse of the multiplexing procedure. To de-multiplex the signal in n-th time division, a pulse train with time delay of 20(n-1)

ps is used to control the switch. The corresponding signal is dropped out and converted back into the 12.5 GHz signals through photodetectors.

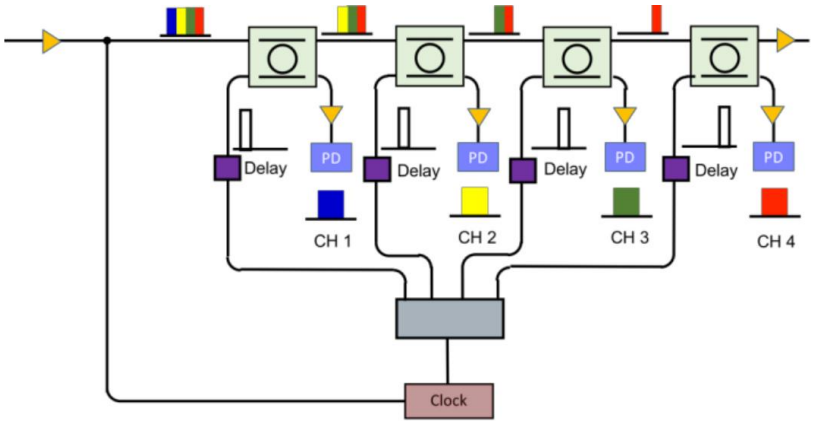

Figure 5.11: Optical time-domain de-multiplexing system.

The layout of such an optical time-domain de-multiplexing system is shown in Figure 5.12(a). The grating couplers are arranged at one side for the fiber array. There is one LO (local oscillator) optical input, four optical inputs for optical switches, four outputs for dropped signal, and one residual optical output. The add-drop structure is used to drop the signal of the selected channel. For the initial demonstration, the optical switches are replaced by electrical optical ring modulators, as shown in Figure 5.12(b).

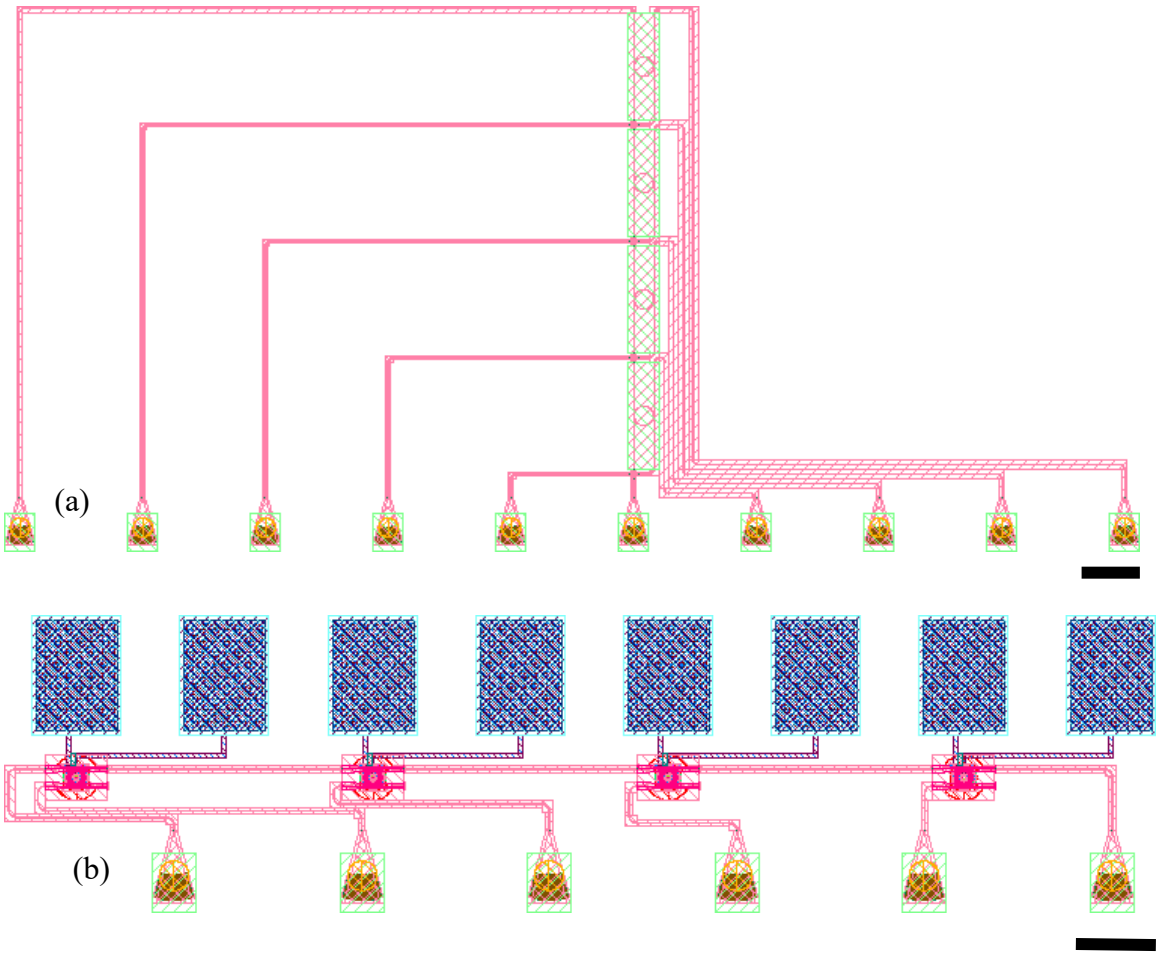

Figure 5.12: (a) The layout of an optical time-domain de-multiplexing system using all optical switches. (b) The layout of an optical time-domain de-multiplexing system, which replaces the all optical switches as ring modulators. The black bar at right bottom corner indicates a length of 60 um.

An optical time-domain de-multiplexing system is simulated by Lumerical Interconnect. The multiplexed signal in Figure 5.10 is input to the de-multiplexing system by a grating coupler. Then, the optical signal of each channel is de-multiplexed by the switch. The schematic of such a de-multiplexing system is shown in Figure 5.13.

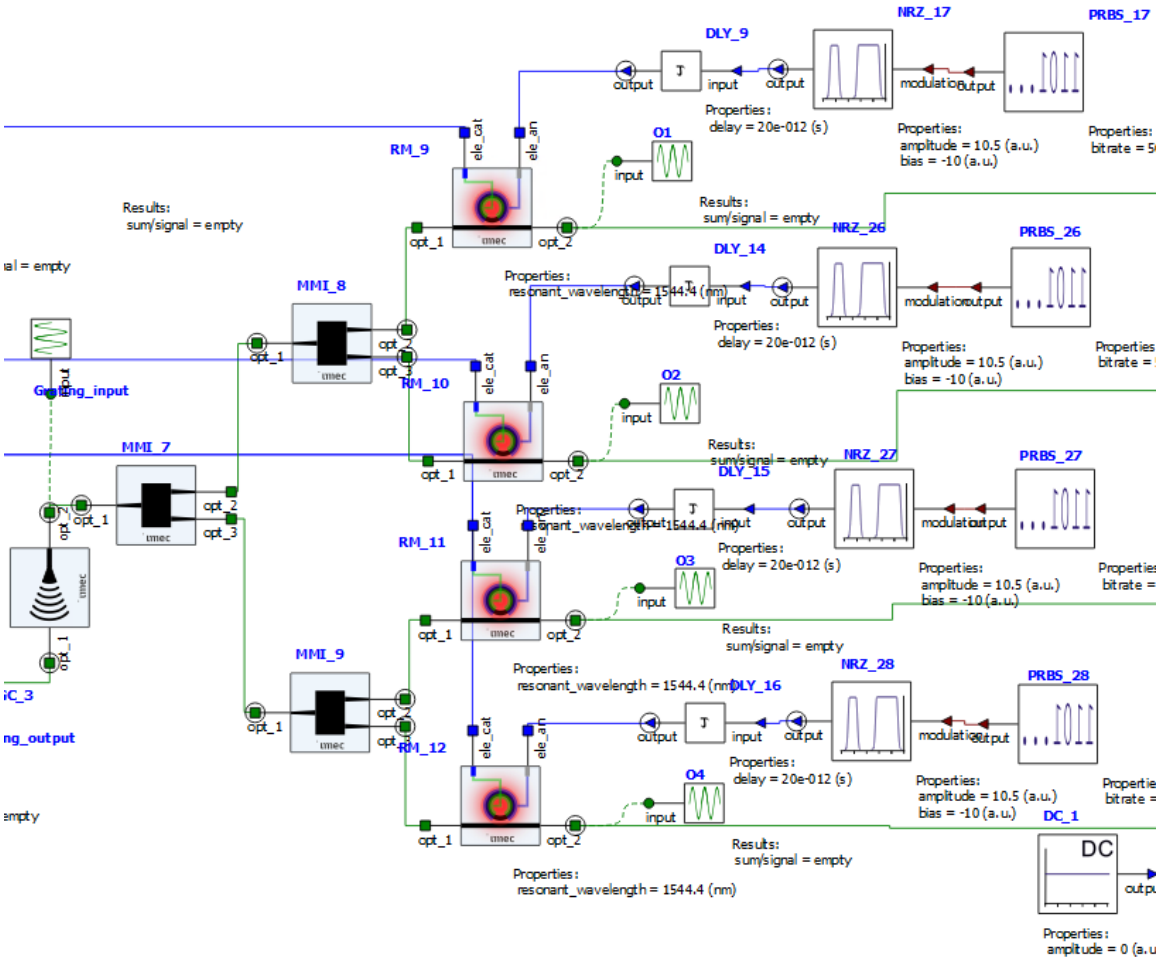

Figure 5.13: Schematic to simulate an optical time-domain de-multiplexing system using Lumerical INTERCONNECT and IMEC CML library.

The multiplexed signal in Figure 5.10 is feed into the de-multiplexing system. The de-multiplexing optical signal for each channel is dropped out by the high-speed switch, which is shown in Figure 5.14.

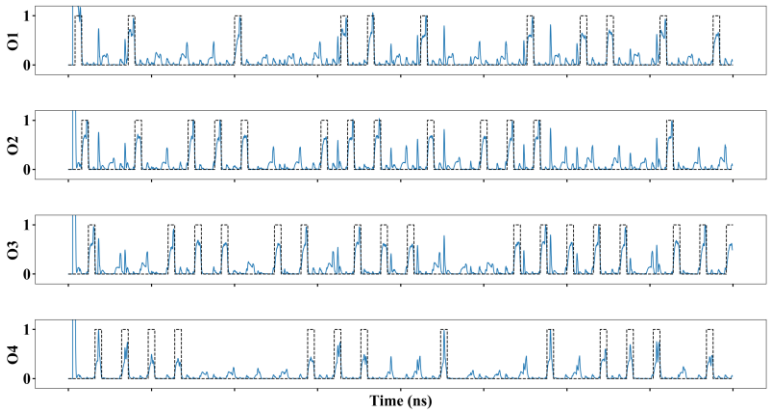

Figure 5.14: The waveform of the optical signal after the switch of each channel for the optical time-domain de-multiplexing system.

5.5 TIME-DIVISION DE-MULTIPLEXING SYSTEM WITH ON-CHIP PHOTODIODE

The on-chip photodiode is made by Germanium on a silicon doped vertical PIN diode. The responsivity at -1 V is 0.8 A/W, which the bandwidth at -1 V is 50 GHz. The dark current at -1 V and -2 V is 10 nA and 80 nA, respectively. The layout of such a photodiode is shown in Figure 5.15.

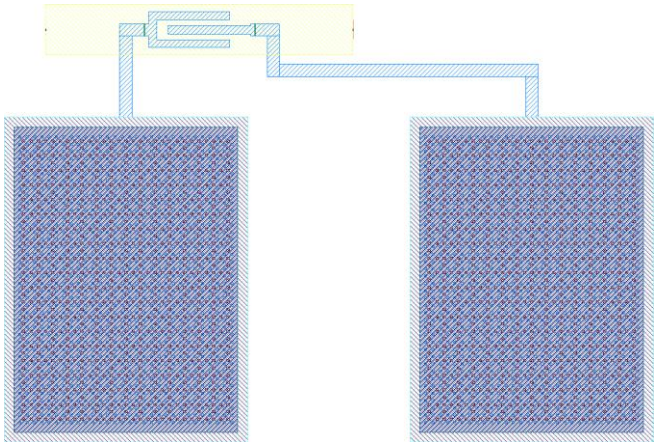

Figure 5.15: The layout of a Ge photodiode. The size of electrical pads is 60um*80um.

The layout of such an optical time-domain de-multiplexing system with Ge photodiodes is shown in Figure 5.16(a). The grating couplers are arranged at one side for the fiber array. There is one LO (local oscillator) optical input, four optical inputs for optical switches, four outputs for dropped signal, and one residual optical output. The add-drop structure is used to drop the signal of the selected channel. Then, the optical signal of each channel is converted back to electrical signal by the Ge photodiodes. For the initial demonstration, the optical switches are replaced by electrical optical ring modulators, as shown in Figure 5.16(b).

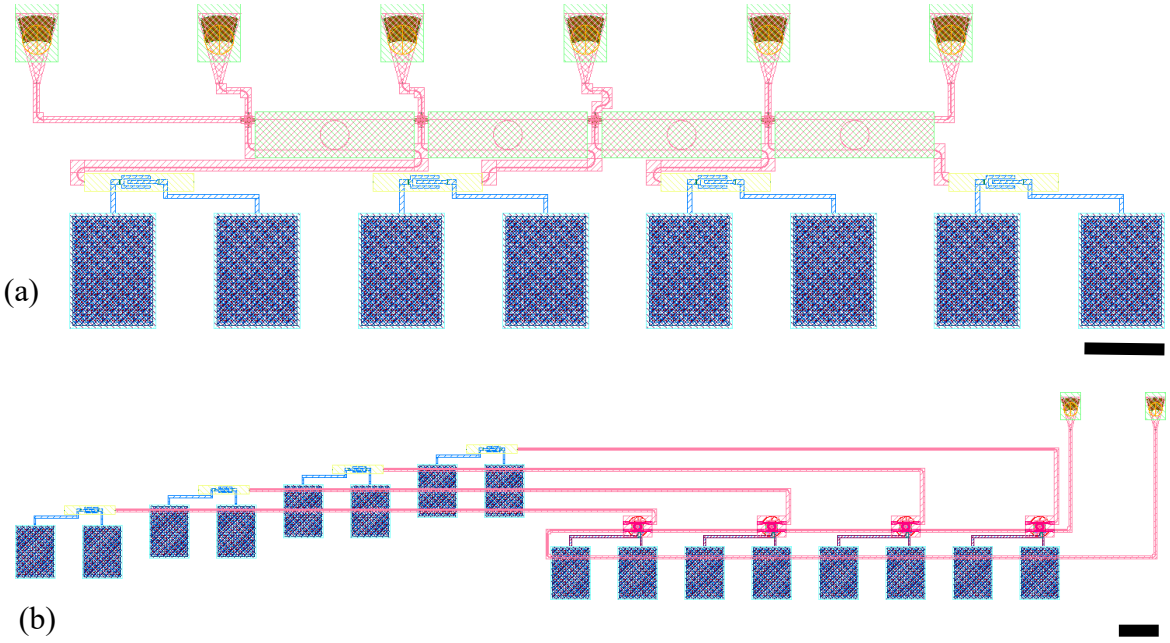

Figure 5.16: (a) The layout of an optical time-domain de-multiplexing system with Ge photodiodes using all optical switches. (b) The layout of an optical time-domain de-multiplexing system with Ge photodiodes, which replaces the all optical switches as ring modulators. The black bar at right-bottom corner indicates a length of 60 um.

An optical time-domain de-multiplexing system with Ge photodiodes is simulated by Lumerical Interconnect. The multiplexed signal in Figure 5.10 is input to the de-multiplexing system by a grating coupler. Then, the optical signal of each channel is de-multiplexed by the switch. The schematic of such a de-multiplexing system is shown in Figure 5.17.

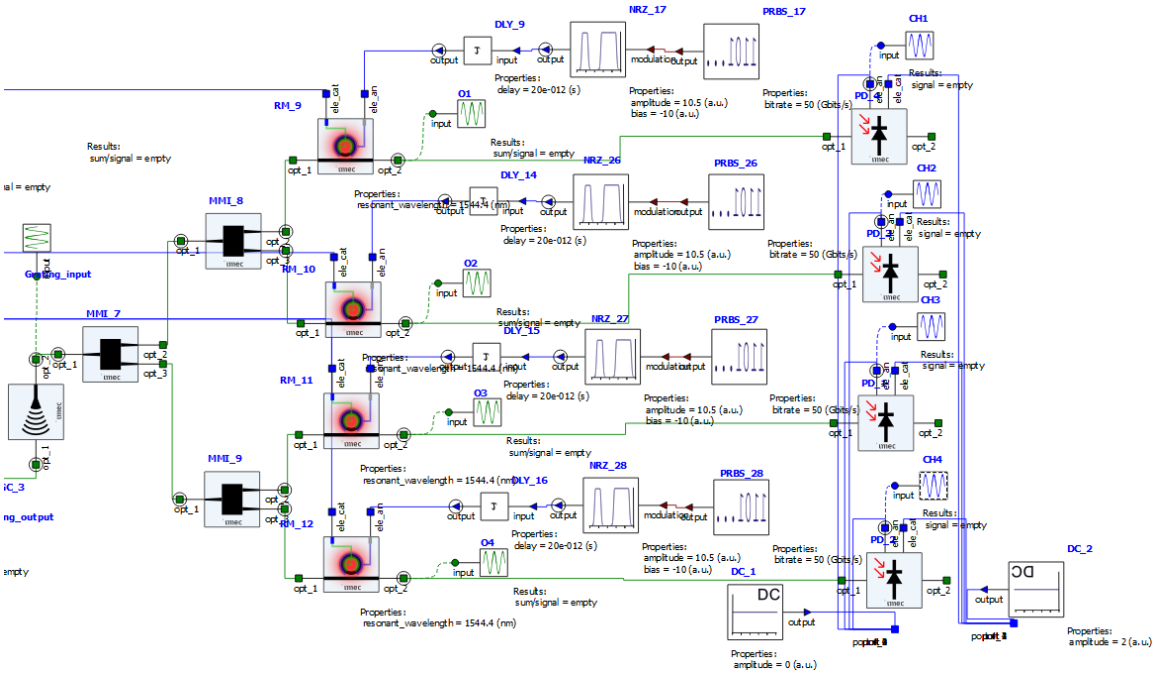

Figure 5.17: Schematic to simulate an optical time-domain de-multiplexing system with Ge photodiodes using Lumerical INTERCONNECT and IMEC CML library.

The multiplexed signal in Figure 5.10 is feed into the de-multiplexing system with Ge photodiodes. The de-multiplexing optical signal for each channel is dropped out by the high-speed switch. Then the optical signal is converted back to electrical signal by the Ge photodiodes, which results are shown in Figure 5.18.

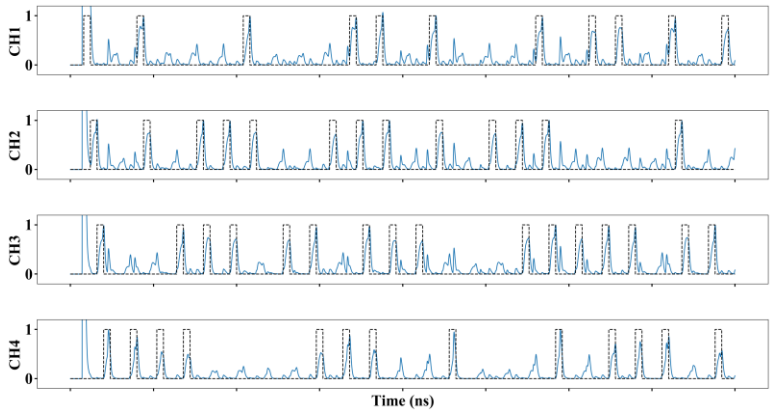

Figure 5.18: The waveform of the electrical signal after the photodetector of each channel for the optical time-domain de-multiplexing system.

5.6 SUMMARY

We have simulated the optical time-domain multiplexing and de-multiplexing system. 4 channels of 12.5 GHz RF signals are used as input signal to modulate the optical signal generated by a distributed feedback (DFB) laser. Then, 4 channels of the 50 GHz switches are used to multiplex the 4 channels of 12.5 GHz optical signal into a 50 GHz optical signal. The de-multiplexing system converts the 50 GHz multiplexed optical signal back to 12.5 GHz RF signal. Higher multiplexing and de-multiplexing speed can be achieved by using pulse generator with narrower line width and larger repetition rate. An external Digital Signal Processing (DSP) circuits can be used to actively improve the signal quality of the optical multiplexing and de-multiplexing system.

Chapter 6: Conclusion

6.1 Conclusion

In this dissertation, several polymer-based integrated photonic waveguide devices are demonstrated for interconnects.

Firstly, a mode transformer based on the quasi-vertical taper is demonstrated to enable high coupling efficiency from a standard SMF into a single mode polymer rib waveguide for optical inter-board interconnects. A triangular region fabricated above the waveguide is adopted to adiabatically transform the mode from the fiber into the polymer waveguide. A quasi-vertical taper for the polymer rib waveguide system is designed, fabricated, and characterized. Coupling losses of 1.79±0.30 dB and 2.23±0.31 dB per coupler for quasi-TM and quasi-TE mode, respectively, are measured across the optical communication C and L bands (1535 nm - 1610 nm). Due to the utilization of standard low cost SMFs for packaging, the overall packaging cost and packaging efforts for the single mode polymer photonic system can be minimized.

Secondly, a thermo-optical switch, 2-bit TO TTD module, and a RF transmission system with ±60° steering angle are demonstrated, utilizing the etch-free and roll-to-roll compatible fabrication process for fabricating very large-area polymer photonic systems utilizing large-area imprinting and inkjet printing processes. The time delays of 0.64 ps, 10.74 ps, 22.90 ps, and 35.39 ps are measured for $0\Delta\tau$, $1\Delta\tau$, $2\Delta\tau$, and $3\Delta\tau$ configuration of the 2-bit TO TTD module, respectively. A 1x4 X-band PAA system is setup and RF beam steering at 0°, ±16.78°, ±35.26°, and ±60° is demonstrated. Such a true-time-delay (TTD) enabled beam steering networks provide several advantages over their electronic counterparts, including squint-free beam steering, low RF loss, immunity to electromagnetic interference (EMI), and large bandwidth control.

Thirdly, the first high-speed optical modulator based on electro-optic polymer infiltrated subwavelength grating waveguide ring resonator is demonstrated. SWG structure increases the interactive volume between the optical signal and EO polymer, compared to a conventional strip waveguide. The power consumption for digital communication is 2.6 *f*J/bit. The 3-dB modulation bandwidth of the fabricated modulator is measured to be larger than 40 GHz occupying an area of 70 µm x 29 µm, which is the largest bandwidth and the most compact footprint that has been demonstrated for the ring resonators on the silicon-organic hybrid platform.

Finally, the 50 GHz optical time-domain multiplexing and de-multiplexing system is designed based on IMEC iSiPP50G platform. The multiplexing system combines 4 channels of 12.5 GHz RF signals to a 50 GHz optical signal. The de-multiplexing system converts the 50 GHz multiplexed optical signal back to 12.5 GHz RF signal.

6.2 FUTURE DIRECTION

In Chapter 5, I have designed an optical time-domain multiplexing and de-multiplexing system. However, it is based on electrical switch, which speed is around 50 GHz. In the future, the electrical switch can be replaced by all-optical switches. And the channel number can be increase to hundreds. The schematic of such a multiplexing and de-multiplexing system is shown in Figure 6.1. The speed of all-optical switch is around 1 THz. Thus, the multiplexing system can combine hundred channels of few GHz electrical signal into a 1 THz optical signal, and the de- multiplexing system can separate the 1 THz optical signal back to few GHz electrical signal. The multiplexed optical signal can propagate inside an optical fiber, which can travel a long distance and is immune to electromagnetic interference (EMI).

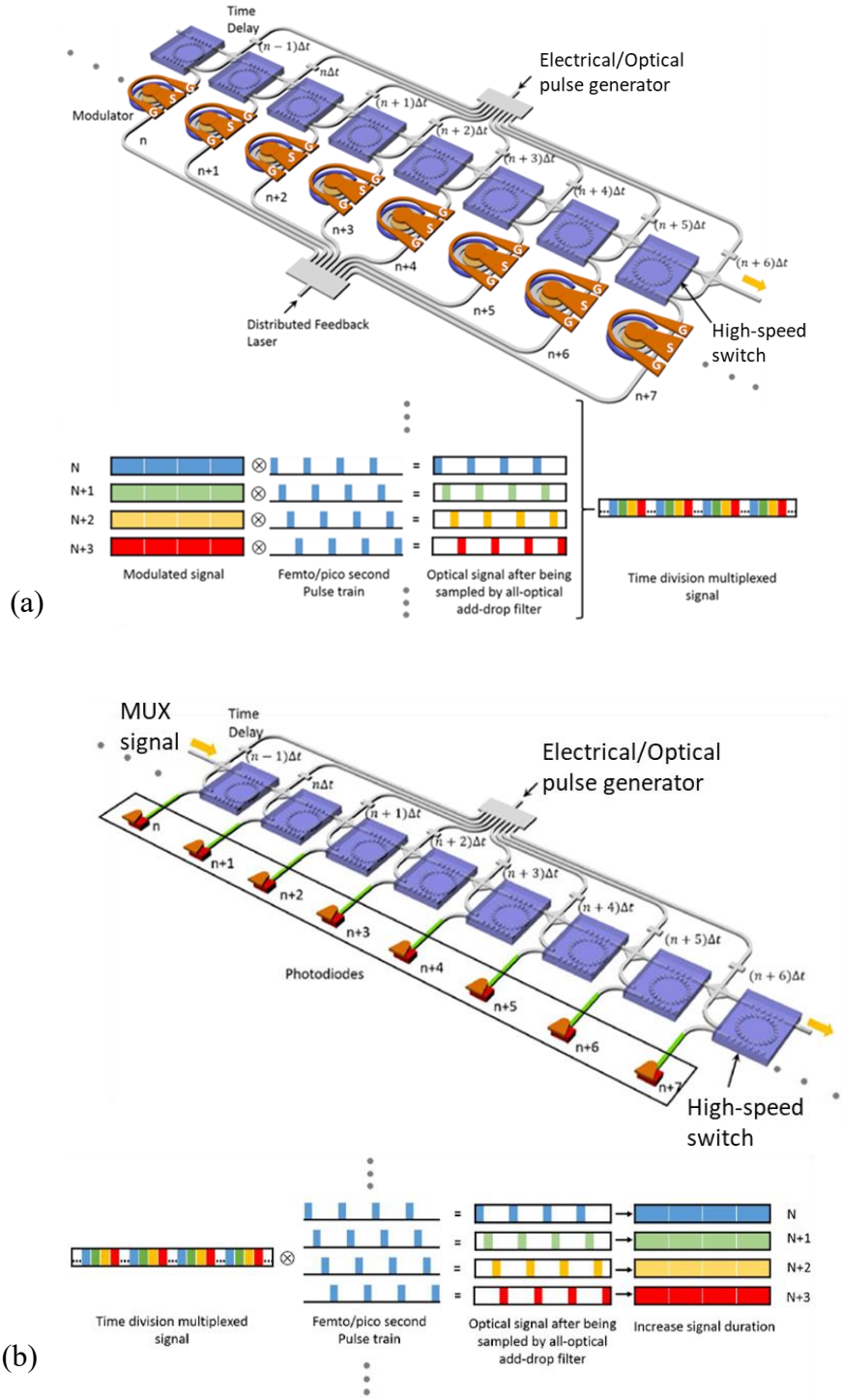

Figure 6.1: Optical time-domain (a) multiplexing and (b) de-multiplexing system.

Appendix

JOURNAL PUBLICATIONS

[1] **Z. Pan**, X. Xu, C.-J. Chung, H. Dalir, H. Yan, K. Chen, Y. Wang, B. Jia, and R. T. Chen, "High-speed modulator based on electro-optic polymer infiltrated subwavelength grating waveguide ring resonator," Laser & Photonics Reviews (accepted).

[2] C.-J. Chung, X. Xu, G. Wang, **Z. Pan**, and R. T. Chen, "On-chip optical true time delay lines featuring one-dimensional fishbone photonic crystal waveguide," Appl. Phys. Lett. 112, 71104 (2018).

[3] C.-J. Chung, X. Xu, **Z. Pan**, F. Mokhtari-Koushyar, R. Wang, H. Yan, H. Subbaraman, and R. T. Chen, "Silicon-based Hybrid Integrated Photonic Chip for Ku band Electromagnetic Wave Sensing," J. Light. Technol. 1–1 (2017).

[4] H. Yan, X. Xu, C.-J. Chung, H. Subbaraman, **Z. Pan**, S. Chakravarty, and R. T. Chen, "One-dimensional photonic crystal slot waveguide for silicon-organic hybrid electro-optic modulators," Opt. Lett. 41, 5466 (2016).

[5] P.-K. Shen, A. Hosseini, X. Xu, Y. Hei, **Z. Pan**, and R. T. Chen, "Multiple-Input Multiple-Output Enabled Large Bandwidth Density On-Chip Optical Interconnect," *J. Light. Technol.* 34, 2969–2974 (2016).

[6] C. Zhang, H. Subbaraman, Q. Li, **Z. Pan**, J. G. Ok, L. Tao, C.-J. Chung, X. Zhang, X. Lin, R. T. Chen, and J. Guo, "Printed Photonic Elements: Nanoimprinting and Beyond," *J. Mater. Chem. C* 4, 5133–5153 (2016).

[7] X. Zhang, C. J. Chung, S. Wang, H. Subbaraman, **Z. Pan**, Q. Zhan, and R. T. Chen, "Integrated Broadband Bowtie Antenna on Transparent Silica Substrate," *IEEE Antennas Wirel. Propag. Lett.* 15, 1377–1381 (2016).

[8] X. Zhang, S. Chakravarty, C.-J. Chung, **Z. Pan**, H. Yan, and R. T. Chen, "Ultra-compact and wide-spectrum-range thermo-optic switch based on silicon coupled photonic crystal microcavities," *Appl. Phys. Lett.* 107, 221104 (2015).

[9] **Z. Pan**, H. Subbaraman, Y. Zou, X. Xu, X. Zhang, C. Zhang, Q. Li, L. Jay Guo, and R. T. Chen, "Quasi-vertical tapers for polymer-waveguide-based interboard optical interconnects," *Photonics Res.* 3, 317–323 (2015).

[10] C.-T. Chen, X. Xu, A. Hosseini, **Z. Pan**, H. Subbaraman, X. Zhang, and R. T. Chen, "Design of Highly Efficient Hybrid Si-Au Taper for Dielectric Strip Waveguide to Plasmonic Slot Waveguide Mode Converter," *Light. Technol. J.* 33, 535–540 (2015).

[11] X. Lin, H. Subbaraman, **Z. Pan**, A. Hosseini, C. Longe, K. Kubena, P. Schleicher, P. Foster, S. Brickey, and R. Chen, "Towards realizing high-throughput, Roll-to-Roll manufacturing of flexible electronic systems," *Electronics* 3, 624–635 (2014).

CONFERENCE PROCEEDINGS

[1] **Z. Pan**, X. Xu, C.-J. Chung, H. Dalir, H. Yan, K. Chen, Y. Wang, B. Jia, and R. T. Chen, " High-speed silicon-organic hybrid modulator enabled by sub-wavelength grating waveguide ring resonator," in in *CLEO* (OSA, 2018).

[2] **Z. Pan**, X. Xu, C.-J. Chung, H. Dalir, H. Yan, K. Chen, Y. Wang, R. Chen, and R. Chen, "High Speed Modulator Based on Electro-optic Polymer Infiltrated

Subwavelength Grating Waveguide Ring Resonator," in Optical Fiber Communication Conference (OSA, 2018), p. M2I.2.

[3] H. Yan, X. Xu, C.-J. Chung, H. Subbaraman, **Z. Pan**, S. Chakravarty, and R. T. Chen, "One-dimensional photonic crystal slot waveguide for silicon-organic hybrid electro-optic modulators," in Photonics West (SPIE, 2017), p. 101090O.

[4] X. Xu, **Z. Pan**, B. Jia, Y. Wang, and R. T. Chen, "All-optical switch with 1 ps response time enabled by graphene oxide infiltrated subwavelength grating waveguide," in Photonics West (SPIE, 2017), p. 1010805.

[5] H. Yan, X. Xu, C.-J. Chung, H. Subbaraman, **Z. Pan**, S. Chakravarty, and R. Chen, "Silicon-organic Hybrid Electro-optic Modulator Based on One-dimensional Photonic Crystal Slot Waveguides," in *CLEO* (OSA, 2016), p. SF1E.6.

[6] **Z. Pan**, H. Subbaraman, C. Zhang, Q. Li, X. Xu, X. Chen, X. Zhang, Y. Zou, A. Panday, L. J. Guo, and R. T. Chen, "RF beam transmission of x-band PAA system utilizing large-area, polymer-based true-time-delay module developed using imprinting and inkjet printing," in *Photonics West* (SPIE, 2016), Vol. 9747, p. 97471T–97471T–7.

[7] H. Subbaraman, **Z. Pan**, C. Zhang, Q. Li, L. J. Guo, and R. T. Chen, "Printed polymer photonic devices for optical interconnect systems," in *Photonics West* (SPIE, 2016), Vol. 9753, p. 97530Y–97530Y–10.

[8] X. Zhang, C. Chung, H. Subbaraman, **Z. Pan**, C.-T. Chen, and R. T. Chen, "Design of a plasmonic-organic hybrid slot waveguide integrated with a bowtie-antenna for terahertz wave detection," in *Photonics West* (SPIE, 2016), Vol. 9756, pp. 975614–975618.

[9] X. Zhang, S. Chakravarty, C.-J. Chung, **Z. Pan**, H. Yan, and R. T. Chen, "Microheater-integrated silicon coupled photonic crystal microcavities for low-

power thermo-optic switching over a wide spectrum," in *Photonics West* (SPIE, 2016), Vol. 9752, pp. 975210–975214.

[10] X. Zhang, H. subbaraman, **Z. Pan**, C.-J. Chung, A. Hosseini, and R. T. Chen, "Low-loss Mode Converter for Silicon-Polymer Hybrid Slot Photonic Crystal Waveguide," in *CLEO* (OSA, 2015), p. SF2H.6.

[11] X. Zhang, S. Chakravarty, C.-J. Chung, **Z. Pan**, and R. T. Chen, "Wide-spectrum-range Power-efficient Compact Thermo-optic Switch Based on Coupled Photonic Crystal Microcavities," in *CLEO* (OSA, 2015), p. JTh2A.45.

[12] X. Zhang, S. Chakravarty, C. Chung, **Z. Pan**, H. Yan, and R. T. Chen, "Coupled photonic crystal microcavities for optical switching over wide spectral range," in *IEEE Optical Interconnects Conference (OI)* (IEEE, 2015), pp. 136–137.

[13] X. Zhang, A. Hosseini, H. Subbaraman, J. Luo, A. A. K. Jen, C. j. Chung, H. Yan, **Z. Pan**, R. L. Nelson, and R. T. Chen, "Backside-gate-assisted broadband modulation on silicon-polymer hybrid photonic crystal waveguide," *IEEE Opt. Interconnects Conf.* 138–139 (2015).

[14] **Z. Pan**, H. Subbaraman, C. Zhang, A. Panday, Q. Li, X. Zhang, Y. Zou, X. Xu, L. J. Guo, and R. T. Chen, "Reconfigurable thermo-optic polymer switch based true-time-delay network utilizing imprinting and inkjet printing," in *Photonics West* (SPIE, 2015), Vol. 9362, pp. 936214–936218.

[15] **Z. Pan**, H. Subbaraman, Y. Zou, X. Zhang, C. Zhang, Q. Li, L. J. Guo, and R. T. Chen, "High optical coupling efficiency quasi-vertical taper for polymer waveguide devices," in *Photonics West* (SPIE, 2015), Vol. 9368, pp. 936807–936808.

[16] X. Zhang, A. Hosseini, H. Subbaraman, S. Wang, Q. Zhan, J. Luo, A. K. Jen, C.-J. Chung, H. Yan, **Z. Pan**, R. L. Nelson, C. Y. Lee, and R. T. Chen, "Antenna-coupled silicon-organic hybrid integrated photonic crystal modulator for broadband

electromagnetic wave detection," in *Photonics West* (SPIE, 2015), Vol. 9362, p. 93620O–93620O–20.

[17] X. Zhang, S. Wang, H. Subbaraman, Q. Zhan, **Z. Pan**, C. Chung, H. Yan, and R. T. Chen, "Integrated broadband bowtie antenna on transparent substrate," in *Photonics West* (SPIE, 2015), Vol. 9362, p. 93620P–93620P–8.

[18] X. Zhang, H. Subbaraman, A. Hosseini, **Z. Pan**, H. Yan, C.-J. Chung, and R. T. Chen, "Low-loss mode converter for coupling light into slotted photonic crystal waveguide," in *Photonics West* (SPIE, 2015), Vol. 9368, pp. 936807–936813.

[19] X. Zhang, A. Hosseini, H. Subbaraman, J. Luo, A. K. Y. Jen, C.-J. Chung, H. Yan, **Z. Pan**, R. L. Nelson, and R. T. Chen, "Broadband energy-efficient optical modulation by hybrid integration of silicon nanophotonics and organic electro-optic polymer," in *Photonics West* (SPIE, 2015), Vol. 9368, p. 93680K–93680K–12.

[20] C.-T. Chen, X. Xu, A. Hosseini, **Z. Pan**, and R. T. Chen, "High efficiency silicon strip waveguide to plasmonic slot waveguide mode converter," in *Photonics West* (SPIE, 2015), Vol. 9368, pp. 936807–936809.

[21] P.-K. Shen, X. Xu, A. Hosseini, **Z. Pan**, and R. T. Chen, "Multiple-input multiple-output based high density on-chip optical interconnect," in *Photonics West* (SPIE, 2015), Vol. 9368, pp. 936812–936816.

[22] **Z. Pan**, H. Subbaraman, X. Lin, Q. Li, C. Zhang, T. Ling, L. J. Guo, and R. T. Chen, "Reconfigurable thermo-optic polymer switch based True-Time-Delay network utilizing imprinting and inkjet printing," in *CLEO* (OSA, 2014), p. SM4G.4.

References

1. W. Heni, C. Haffner, D. L. Elder, A. F. Tillack, Y. Fedoryshyn, R. Cottier, Y. Salamin, C. Hoessbacher, U. Koch, B. Cheng, B. Robinson, L. R. Dalton, and J. Leuthold, "Nonlinearities of organic electro-optic materials in nanoscale slots and implications for the optimum modulator design," Opt. Express **25**, 2627 (2017).
2. B. Bortnik, Y.-C. Hung, H. Tazawa, B.-J. Seo, J. Luo, A. K.-Y. Jen, W. H. Steier, and H. R. Fetterman, "Electrooptic Polymer Ring Resonator Modulation up to 165 GHz," IEEE J. Sel. Top. Quantum Electron. **13**, 104–110 (2007).
3. L. Gu, W. Jiang, X. Chen, and R. T. Chen, "Physical Mechanism of p-i-n-Diode-Based Photonic Crystal Silicon Electrooptic Modulators for Gigahertz Operation," IEEE J. Sel. Top. Quantum Electron. **14**, 1132–1139 (2008).
4. D. Chen, H. R. Fetterman, A. Chen, W. H. Steier, L. R. Dalton, W. Wang, and Y. Shi, "Demonstration of 110 GHz electro-optic polymer modulators," Appl. Phys. Lett. **70**, 3335–3337 (1997).
5. H. Subbaraman, Z. Pan, C. Zhang, Q. Li, L. J. Guo, and R. T. Chen, "Printed polymer photonic devices for optical interconnect systems," in *Photonics West* (SPIE, 2016), Vol. 9753, p. 97530Y–97530Y–10.
6. Y.-T. Han, J.-U. Shin, S.-H. Park, H.-J. Lee, W.-Y. Hwang, H.-H. Park, and Y. Baek, "N × N polymer matrix switches using thermo-optic total-internal-reflection switch," Opt. Express **20**, 13284–13295 (2012).
7. Y.-O. Noh, H.-J. Lee, Y.-H. Won, and M.-C. Oh, "Polymer waveguide thermo-optic switches with −70 dB optical crosstalk," Opt. Commun. **258**, 18–22 (2006).
8. X. Wang, B. Howley, M. Y. Chen, and R. T. Chen, "4 × 4 Nonblocking Polymeric Thermo-Optic Switch Matrix Using the Total Internal Reflection Effect," IEEE J. Sel. Top. Quantum Electron. **12**, 997–1000 (2006).
9. B. Howley, X. Wang, M. Chen, and R. T. Chen, "Reconfigurable delay time polymer planar lightwave circuit for an X-band phased-array antenna demonstration," J. Light. Technol. **25**, 883–890 (2007).
10. Y. Chen, K. Wu, F. Zhao, G. Kim, and R. T. Chen, "Reconfigurable true-time delay for wideband phased-array antennas," in *Emerging Optoelectronic Applications* (SPIE, 2004), Vol. 5363, pp. 125–130.
11. X. Wang, B. Howley, M. Y. Chen, Q. Zhou, R. Chen, and P. Basile, "Polymer-based thermo-optic switch for optical true time delay," in *Integrated Optics: Devices, Materials, and Technologies IX* (SPIE, 2005), Vol. 5728, pp. 60–67.
12. C. Changming, H. Chao, W. Lei, Z. Haixin, S. Xiaoqiang, W. Fei, and Z. DaMing, "650-nm All-Polymer Thermo-Optic Waveguide Switch Arrays Based on Novel Organic-Inorganic Grafting PMMA Materials," IEEE J. Quantum Electron. **49**,

447–453 (2013).

13. F. Qiu, J. Liu, G. Cao, Y. Guan, Q. Shen, D. Yang, and Q. Guo, "Design and analysis of Y-branched polymeric digital optical switch with low power consumption," Opt. Commun. **296**, 53–56 (2013).

14. D. M. Zhang, X. Q. Sun, F. Wang, and C. M. Chen, "Fast polymer thermo-optic switch with silica under-cladding," in *2013 IEEE International Symposium on Next-Generation Electronics (ISNE)* (2013), pp. 92–94.

15. H. Yu, X. Jiang, J. Yang, X. Li, M. Wang, and Y. Li, "The design of a 2×2 polymer TIR switch based on thermal field analysis employing thermo-optic effect," in *Passive Components and Fiber-Based Devices* (SPIE, 2005), Vol. 5623, pp. 174–183.

16. X. Lin, T. Ling, H. Subbaraman, L. J. Guo, and R. T. Chen, "Printable thermo-optic polymer switches utilizing imprinting and ink-jet printing," Opt. Express **21**, 2110–2117 (2013).

17. X. Wang, B. Howley, M. Y. Chen, and R. T. Chen, "Polarization-independent all-wave polymer-based TIR thermooptic switch," J. Light. Technol. **24**, 1558–1565 (2006).

18. J. Yang, Q. Zhou, and R. T. Chen, "Polyimide-waveguide-based thermal optical switch using total-internal-reflection effect," Appl. Phys. Lett. **81**, 2947–2949 (2002).

19. X. Niu, Y. Zheng, Y. Gu, C. Chen, Z. Cai, Z. Shi, F. Wang, X. Sun, Z. Cui, and D. Zhang, "Thermo-optic waveguide gate switch arrays based on direct UV-written highly fluorinated low-loss photopolymer," Appl. Opt. **53**, 6698–6705 (2014).

20. Z. Pan, H. Subbaraman, X. Lin, Q. Li, C. Zhang, T. Ling, L. J. Guo, and R. T. Chen, "Reconfigurable thermo-optic polymer switch based True-Time-Delay network utilizing imprinting and inkjet printing," in *CLEO* (OSA, 2014), p. SM4G.4.

21. Z. Pan, H. Subbaraman, C. Zhang, A. Panday, Q. Li, X. Zhang, Y. Zou, X. Xu, L. J. Guo, and R. T. Chen, "Reconfigurable thermo-optic polymer switch based true-time-delay network utilizing imprinting and inkjet printing," in *Photonics West* (SPIE, 2015), Vol. 9362, pp. 936214–936218.

22. G. Coppola, L. Sirleto, I. Rendina, and M. Iodice, "Advance in thermo-optical switches: principles, materials, design, and device structure," Opt. Eng. **50**, 71112–71114 (2011).

23. X. Wang, B. Howley, M. Y. Chen, and R. T. Chen, "Phase error corrected 4-bit true time delay module using a cascaded 2 × 2 polymer waveguide switch array," Appl. Opt. **46**, 379–383 (2007).

24. A. Yeniay and G. Renfeng, "True Time Delay Photonic Circuit Based on

Perfluorpolymer Waveguides," Photonics Technol. Lett. IEEE **22**, 1565–1567 (2010).

25. J. Capmany and D. Novak, "Microwave photonics combines two worlds," Nat. Photonics **1**, 319–330 (2007).

26. B. Howley, C. Yihong, X. Wang, Z. Qingjun, Z. Shi, Y. Jiang, and Y. Chen, "2-bit reconfigurable true time delay lines using 2×2 polymer waveguide switches," Photonics Technol. Lett. IEEE **17**, 1944–1946 (2005).

27. W.-J. Chin, D.-H. Kim, J.-H. Song, and S.-S. Lee, "Integrated photonic microwave bandpass filter incorporating a polymeric microring resonator," Jpn. J. Appl. Phys. **45**, 2576 (2006).

28. X. Zhang, A. Hosseini, X. Lin, H. Subbaraman, and R. T. Chen, "Polymer-based hybrid-integrated photonic devices for silicon on-chip modulation and board-level optical interconnects," IEEE J. Sel. Top. Quantum Electron. **19**, 196–210 (2013).

29. X. Lin, A. Hosseini, X. Dou, H. Subbaraman, and R. T. Chen, "Low-cost board-to-board optical interconnects using molded polymer waveguide with 45 degree mirrors and inkjet-printed micro-lenses as proximity vertical coupler," Opt. Express **21**, 60–69 (2013).

30. R. Dangel, F. Horst, D. Jubin, N. Meier, J. Weiss, B. J. Offrein, B. W. Swatowski, C. M. Amb, D. J. Deshazer, and W. K. Weidner, "Development of versatile polymer waveguide flex technology for use in optical interconnects," Light. Technol. J. **31**, 3915–3926 (2013).

31. B. Block, S. Liff, M. Kobrinsky, M. Reshotko, R. Tseng, I. Ban, and P. Chang, "A low power electro-optic polymer clad Mach-Zehnder modulator for high speed optical interconnects," in J. Kubby and G. T. Reed, eds. (International Society for Optics and Photonics, 2013), Vol. 8629, p. 86290Z.

32. X. Dou, A. X. Wang, X. Lin, and R. T. Chen, "Photolithography-free polymer optical waveguide arrays for optical backplane bus," Opt. Express **19**, 14403–14410 (2011).

33. R. T. Chen, L. Lin, C. Choi, Y. J. Liu, B. Bihari, L. Wu, S. Tang, R. Wickman, B. Picor, M. K. Hibb-Brenner, J. Bristow, and Y. S. Liu, "Fully embedded board-level guided-wave optoelectronic interconnects," Proc. IEEE **88**, 780–793 (2000).

34. R. T. Chen, W. Phillips, T. Jannson, and D. Pelka, "Integration of holographic optical elements with polymer gelatin waveguides on GaAs, LiNbO3, glass, and aluminum," Opt. Lett. **14**, 892–894 (1989).

35. R. T. Chen, L. Wu, F. Li, S. Tang, M. Dubinovsky, J. Qi, C. L. Schow, J. C. Campbell, R. Wickman, B. Picor, M. Hibbs-Brenner, J. Bristow, Y. S. Liu, S. Rattan, and C. Noddings, "Si CMOS process compatible guided-wave multi-GBit/sec optical clock signal distribution system for Cray T-90 supercomputer," in

Massively Parallel Processing Using Optical Interconnections, 1997., Proceedings of the Fourth International Conference on (1997), pp. 10–24.

36. S. Natarajan, C. Zhao, and R. T. Chen, "Bi-directional optical backplane bus for general purpose multi-processor board-to-board optoelectronic interconnects," Light. Technol. J. **13**, 1031–1040 (1995).

37. X. Lin, T. Ling, H. Subbaraman, X. Zhang, K. Byun, L. J. Guo, and R. T. Chen, "Ultraviolet imprinting and aligned ink-jet printing for multilayer patterning of electro-optic polymer modulators," Opt. Lett. **38**, 1597–1599 (2013).

38. X. Zhang, B. Lee, C. Lin, A. X. Wang, A. Hosseini, and R. T. Chen, "Highly linear broadband optical modulator based on electro-optic polymer," IEEE Photonics J. **4**, 2214–2228 (2012).

39. L. R. Dalton, "Electro-optic polymer modulators," Broadband Opt. Modul. Sci. Technol. Appl. 223 (2011).

40. J. Liu, G. Xu, F. Liu, I. Kityk, X. Liu, and Z. Zhen, "Recent advances in polymer electro-optic modulators," RSC Adv. **5**, 15784–15794 (2015).

41. X. Zhang, A. Hosseini, H. Subbaraman, S. Wang, Q. Zhan, J. Luo, A. K. Y. Jen, and R. T. Chen, "Integrated photonic electromagnetic field sensor based on broadband bowtie antenna coupled silicon organic hybrid modulator," J. Light. Technol. **32**, 3774–3784 (2014).

42. C.-Y. Lin, A. X. Wang, B. S. Lee, X. Zhang, and R. T. Chen, "High dynamic range electric field sensor for electromagnetic pulse detection," Opt. Express **19**, 17372–17377 (2011).

43. S.-L. Chen, Y.-C. Chang, C. Zhang, J. G. Ok, T. Ling, M. T. Mihnev, T. B. Norris, and L. J. Guo, "Efficient real-time detection of terahertz pulse radiation based on photoacoustic conversion by carbon nanotube nanocomposite," Nat Phot. **8**, 537–542 (2014).

44. C. Zhang, T. Ling, S.-L. Chen, and L. J. Guo, "Ultrabroad Bandwidth and Highly Sensitive Optical Ultrasonic Detector for Photoacoustic Imaging," ACS Photonics **1**, 1093–1098 (2014).

45. C. Zhang, S. Chen, T. Ling, and L. Jay Guo, "Review of Imprinted Polymer Microrings as Ultrasound Detectors: Design, Fabrication, and Characterization," Sensors Journal, IEEE **15**, 3241–3248 (2015).

46. C. Zhang, S.-L. Chen, T. Ling, and L. J. Guo, "Imprinted Polymer Microrings as High Performance Ultrasound Detectors in Photoacoustic Imaging," Light. Technol. J. **PP**, 1 (2015).

47. Z. Pan, H. Subbaraman, Y. Zou, X. Zhang, C. Zhang, Q. Li, L. J. Guo, and R. T. Chen, "High optical coupling efficiency quasi-vertical taper for polymer waveguide devices," in *Photonics West* (SPIE, 2015), Vol. 9368, pp. 936807–

936808.

48. Z. Pan, H. Subbaraman, Y. Zou, X. Xu, X. Zhang, C. Zhang, Q. Li, L. Jay Guo, and R. T. Chen, "Quasi-vertical tapers for polymer-waveguide-based interboard optical interconnects," Photonics Res. **3**, 317–323 (2015).

49. X. Lin, H. Subbaraman, Z. Pan, A. Hosseini, C. Longe, K. Kubena, P. Schleicher, P. Foster, S. Brickey, and R. Chen, "Towards realizing high-throughput, Roll-to-Roll manufacturing of flexible electronic systems," Electronics **3**, 624–635 (2014).

50. R. A. Soref, "Silicon-based optoelectronics," Proc. IEEE **81**, 1687–1706 (1993).

51. R. Soref, "The Past, Present, and Future of Silicon Photonics," IEEE J. Sel. Top. Quantum Electron. **12**, 1678–1687 (2006).

52. D. Thomson, A. Zilkie, J. E. Bowers, T. Komljenovic, G. T. Reed, L. Vivien, D. Marris-Morini, E. Cassan, L. Virot, J.-M. Fédéli, J.-M. Hartmann, J. H. Schmid, D.-X. Xu, F. Boeuf, P. O'Brien, G. Z. Mashanovich, and M. Nedeljkovic, "Roadmap on silicon photonics," J. Opt. **18**, 73003 (2016).

53. J. E. Bowers, T. Komljenovic, M. Davenport, J. Hulme, A. Y. Liu, C. T. Santis, A. Spott, S. Srinivasan, E. J. Stanton, and C. Zhang, "Recent advances in silicon photonic integrated circuits," in *Photonics West* (SPIE, 2016), Vol. 9774, p. 977402.

54. D. Perez-Galacho, C. Baudot, T. Hirtzlin, S. Messaoudène, N. Vulliet, P. Crozat, F. Boeuf, L. Vivien, and D. Marris-Morini, "Low voltage 25Gbps silicon Mach-Zehnder modulator in the O-band," Opt. Express **25**, 11217 (2017).

55. R. Waldhäusl, B. Schnabel, P. Dannberg, E.-B. Kley, A. Bräuer, and W. Karthe, "Efficient coupling into polymer waveguides by gratings," Appl. Opt. **36**, 9383–9390 (1997).

56. R. Bruck and R. Hainberger, "Efficiency enhancement of grating couplers for single-mode polymer waveguides through high index coatings," in *Proceedings 14th European Conference on Integrated Optics* (2008), pp. 201–204.

57. R. Bruck and R. Hainberger, "Efficient small grating couplers for low-index difference waveguide systems," in (2009), Vol. 7218, p. 72180A–72180A–11.

58. L. Wang, Y. Li, M. Garcia Porcel, D. Vermeulen, X. Han, J. Wang, X. Jian, R. Baets, M. Zhao, and G. Morthier, "A polymer-based surface grating coupler with an embedded Si3N4 layer," J. Appl. Phys. **111**, 114507 (2012).

59. M. E. Pollard, S. J. Pearce, R. Chen, S. Oo, and M. D. B. Charlton, "Polymer waveguide grating couplers for low-cost nanoimprinted integrated optics," in (2012), Vol. 8264, p. 826418.

60. Z. Zhang, A. Maese-Novo, E. Schwartz, C. Zawadzki, and N. Keil, "301-nm wavelength tunable differentially driven all-polymer optical filter," Opt. Lett. **39**,

5170–5172 (2014).

61. Y. Shani, C. H. Henry, R. C. Kistler, K. J. Orlowsky, and D. A. Ackerman, "Efficient coupling of a semiconductor laser to an optical fiber by means of a tapered waveguide on silicon," Appl. Phys. Lett. **55**, 2389–2391 (1989).

62. B. Mersali, A. Ramdane, and A. Carenco, "Optical-mode transformer: a III-V circuit integration enabler," Sel. Top. Quantum Electron. IEEE J. **3**, 1321–1331 (1998).

63. I. Moerman, P. P. Van Daele, and P. M. Demeester, "A review on fabrication technologies for the monolithic integration of tapers with III-V semiconductor devices," Sel. Top. Quantum Electron. IEEE J. **3**, 1308–1320 (1998).

64. T. T. Aalto, P. Heimala, S. Yliniemi, M. Kapulainen, and M. J. Leppihalme, "Fabrication and characterization of waveguide structures on SOI," in *Integrated Optical Devices: Fabrication and Testing* (2003), Vol. 4944, pp. 183–194.

65. I. E. Day, I. Evans, A. Knights, F. Hopper, S. Roberts, J. Johnston, S. Day, J. Luff, H. K. Tsang, and M. Asghari, "Tapered Silicon Waveguides for Low Insertion Loss Highly-Efficient High-Speed Electronic Variable Optical Attenuators," in *Optical Fiber Communication Conference* (Optical Society of America, 2003), p. TuM5.

66. R. J. Bozeat, S. Day, F. Hopper, F. P. Payne, S. W. Roberts, and M. Asghari, "Silicon based waveguides," in *Silicon Photonics* (Springer, 2004), pp. 269–294.

67. T. Aalto, K. Solehmainen, M. Harjanne, M. Kapulainen, and P. Heimala, "Low-loss converters between optical silicon waveguides of different sizes and types," IEEE Photonics Technol. Lett. **18**, 709–711 (2006).

68. D. Dai, S. He, and T. Hon-Ki, "Bilevel mode converter between a silicon nanowire waveguide and a larger waveguide," J. Light. Technol. **24**, 2428–2433 (2006).

69. J. K. Doylend and A. P. Knights, "Design and simulation of an integrated fiber-to-chip coupler for silicon-on-insulator waveguides," IEEE J. Sel. Top. Quantum Electron. **12**, 1363–1370 (2006).

70. V. Nguyen, T. Montalbo, C. Manolatou, A. Agarwal, C. Hong, J. Yasaitis, L. C. Kimerling, and J. Michel, "Silicon-based highly-efficient fiber-to-waveguide coupler for high index contrast systems," Appl. Phys. Lett. **88**, (2006).

71. A. Barkai, A. Liu, D. Kim, R. Cohen, N. Elek, H.-H. Chang, B. H. Malik, R. Gabay, R. Jones, M. Paniccia, and N. Izhaky, "Double-stage taper for coupling between SOI waveguides and single-mode fiber," J. Light. Technol. **26**, 3860–3865 (2008).

72. Q. Fang, T.-Y. Liow, J. F. Song, C. W. Tan, M. Bin Yu, G. Q. Lo, and D.-L. Kwong, "Suspended optical fiber-to-waveguide mode size converter for silicon photonics," Opt. Express **18**, 7763–7769 (2010).

73. Q. Huang, J. Cheng, L. Liu, Y. Tang, and S. He, "Ultracompact tapered coupler for the Si/III-V heterogeneous integration," Appl. Opt. **54**, 4327–4332 (2015).

74. H. Park, S. Kim, J. Park, J. Joo, and G. Kim, "A fiber-to-chip coupler based on Si/SiON cascaded tapers for Si photonic chips," Opt. Express **21**, 29313–29319 (2013).

75. A. Khilo, M. A. Popović, M. Araghchini, and F. X. Kärtner, "Efficient planar fiber-to-chip coupler based on two-stage adiabatic evolution," Opt. Express **18**, 15790–15806 (2010).

76. M. Wood, P. Sun, and R. M. Reano, "Compact cantilever couplers for low-loss fiber coupling to silicon photonic integrated circuits," Opt. Express **20**, 164–172 (2012).

77. M. Pu, L. Liu, H. Ou, K. Yvind, and J. M. Hvam, "Ultra-low-loss inverted taper coupler for silicon-on-insulator ridge waveguide," Opt. Commun. **283**, 3678–3682 (2010).

78. T. Shoji, T. Tsuchizawa, T. Watanabe, K. Yamada, and H. Morita, "Low loss mode size converter from 0.3 μm square Si wire waveguides to singlemode fibres," Electron. Lett. **38**, 1669–1670 (2002).

79. R. Orobtchouk, "On Chip Optical Waveguide Interconnect: the Problem of the In/Out Coupling," in *Optical Interconnects* (Springer, 2006), pp. 263–290.

80. K. Kataoka, "Estimation of coupling efficiency of optical fiber by far-field method," Opt. Rev. **17**, 476–480 (2010).

81. M. Sanghadasa, P. R. Ashley, E. L. Webster, C. Cocke, G. A. Lindsay, and A. J. Guenthner, "A simplified technique for efficient fiber-polymer-waveguide power coupling using a customized cladding with tunable index of refraction," Light. Technol. J. **24**, 3816–3823 (2006).

82. Y. Shun, B. Mukherjee, and S. Dixit, "Advances in photonic packet switching: an overview," IEEE Commun. Mag. **38**, 84–94 (2000).

83. S. Nakamura, Y. Ueno, and K. Tajima, "168-Gb/s all-optical wavelength conversion with a symmetric-Mach-Zehnder-type switch," IEEE Photonics Technol. Lett. **13**, 1091–1093 (2001).

84. L. Gu, W. Jiang, C. Xiaonan, and R. T. Chen, "Thermooptically Tuned Photonic Crystal Waveguide Silicon-on-Insulator Mach–Zehnder Interferometers," IEEE Photonics Technol. Lett. **19**, 342–344 (2007).

85. X. Zhang, S. Chakravarty, C.-J. Chung, Z. Pan, H. Yan, and R. T. Chen, "Ultra-compact and wide-spectrum-range thermo-optic switch based on silicon coupled photonic crystal microcavities," Appl. Phys. Lett. **107**, 221104 (2015).

86. M. Y. Chen, D. Pham, H. Subbaraman, X. Lu, and R. T. Chen, "Conformal Ink-Jet

Printed C-Band Phased-Array Antenna Incorporating Carbon Nanotube Field-Effect Transistor Based Reconfigurable True-Time Delay Lines," IEEE Trans. Microw. Theory Tech. **60**, 179–184 (2012).

87. Z. Shi, Y. Chen, H. R. Fetterman, G. Brost, X. Wang, L. Gu, B. Howley, Y. Jiang, Q. Zhou, and R. Chen, "True-time-delay modules based on a single tunable laser in conjunction with a waveguide hologram for phased array antenna application," Opt. Eng. **44**, 84301–84307 (2005).

88. H. Subbaraman, M. Y. Chen, and R. T. Chen, "Photonic dual RF beam reception of an X band phased array antenna using a photonic crystal fiber-based true-time-delay beamformer," Appl. Opt. **47**, 6448–6452 (2008).

89. T. Ling, S.-L. Chen, and L. J. Guo, "High-sensitivity and wide-directivity ultrasound detection using high Q polymer microring resonators," Appl. Phys. Lett. **98**, 204103 (2011).

90. H. Subbaraman, D. T. Pham, X. Xiaochuan, M. Y. Chen, A. Hosseini, L. Xuejun, and R. T. Chen, "Inkjet-Printed Two-Dimensional Phased-Array Antenna on a Flexible Substrate," Antennas Wirel. Propag. Lett. IEEE **12**, 170–173 (2013).

91. D. T. Pham, H. Subbaraman, M. Y. Chen, X. Xiaochuan, and R. T. Chen, "Light Weight and Conformal 2-Bit, 1 X 4 Phased-Array Antenna With CNT-TFT-Based Phase Shifter on a Flexible Substrate," Antennas Propagation, IEEE Trans. **59**, 4553–4558 (2011).

92. D. Pham, H. Subbaraman, M. Y. Chen, X. Xu, and R. T. Chen, "Phase shifter using carbon nanotube thin-film transistor for flexible phased-array antenna," in *Proc. SPIE 7936, RF and Millimeter-Wave Photonics* (2011), Vol. 7936, pp. 793604–793606.

93. X. Zhang, S. Wang, H. Subbaraman, Q. Zhan, Z. Pan, C. Chung, H. Yan, and R. T. Chen, "Integrated broadband bowtie antenna on transparent substrate," in *Photonics West* (SPIE, 2015), Vol. 9362, p. 93620P–93620P–8.

94. X. Zhang, C. J. Chung, S. Wang, H. Subbaraman, Z. Pan, Q. Zhan, and R. T. Chen, "Integrated Broadband Bowtie Antenna on Transparent Silica Substrate," IEEE Antennas Wirel. Propag. Lett. **15**, 1377–1381 (2016).

95. R. Ding, Y. Liu, Y. Ma, Y. Yang, Q. Li, A. E.-J. Lim, G.-Q. Lo, K. Bergman, T. Baehr-Jones, and M. Hochberg, "High-Speed Silicon Modulator With Slow-Wave Electrodes and Fully Independent Differential Drive," J. Light. Technol. **32**, 2240–2247 (2014).

96. R. Ding, Y. Liu, Q. Li, Y. Yang, Y. Ma, K. Padmaraju, A. E.-J. Lim, G.-Q. Lo, K. Bergman, T. Baehr-Jones, and M. Hochberg, "Design and characterization of a 30-GHz bandwidth low-power silicon traveling-wave modulator," Opt. Commun. **321**, 124–133 (2014).

97. H. Xu, X. Li, X. Xiao, Z. Li, Y. Yu, and J. Yu, "Demonstration and Characterization of High-Speed Silicon Depletion-Mode Mach-Zehnder Modulators," IEEE J. Sel. Top. Quantum Electron. **20**, (2014).

98. R. Soref and B. Bennett, "Electrooptical effects in silicon," IEEE J. Quantum Electron. **23**, 123–129 (1987).

99. G. P. Agrawal, *Lightwave Technology: Components and Devices* (John Wiley & Sons, 2004).

100. D. J. Thomson, F. Y. Gardes, J. M. Fedeli, S. Zlatanovic, Y. Hu, B. P. P. Kuo, E. Myslivets, N. Alic, S. Radic, G. Z. Mashanovich, and G. T. Reed, "50-Gb/s silicon optical modulator," IEEE Photonics Technol. Lett. **24**, 234–236 (2012).

101. L. Alloatti, R. Palmer, S. Diebold, K. P. Pahl, B. Chen, R. Dinu, M. Fournier, J.-M. Fedeli, T. Zwick, W. Freude, C. Koos, and J. Leuthold, "100 GHz silicon-organic hybrid modulator," Light Sci. Appl. **3**, e173 (2014).

102. S. Koeber, R. Palmer, M. Lauermann, W. Heni, D. L. Elder, D. Korn, M. Woessner, L. Alloatti, S. Koenig, P. C. Schindler, H. Yu, W. Bogaerts, L. R. Dalton, W. Freude, J. Leuthold, and C. Koos, "Femtojoule electro-optic modulation using a silicon–organic hybrid device," Light Sci. Appl. **4**, e255 (2015).

103. H. Zwickel, S. Wolf, C. Kieninger, Y. Kutuvantavida, M. Lauermann, T. de Keulenaer, A. Vyncke, R. Vaernewyck, J. Luo, A. K.-Y. Jen, W. Freude, J. Bauwelinck, S. Randel, and C. Koos, "Silicon-organic hybrid (SOH) modulators for intensity-modulation / direct-detection links with line rates of up to 120 Gbit/s," Opt. Express **25**, 23784 (2017).

104. C. Kieninger, Y. Kutuvantavida, H. Zwickel, S. Wolf, M. Lauermann, D. Elder, L. Dalton, W. Freude, S. Randel, C. Koos, S. Randel, C. Koos, and C. Koos, "Record-High In-Device Electro-Optic Coefficient of 359 pm/V in a Silicon-Organic Hybrid (SOH) Modulator," in *Conference on Lasers and Electro-Optics* (OSA, 2017), p. STu3N.2.

105. H. Zwickel, T. De Keulenaer, S. Wolf, C. Kieninger, Y. Kutuvantavida, M. Lauermann, M. Verplaetse, R. Pierco, R. Vaernewyck, A. Vyncke, X. Yin, G. Torfs, W. Freude, E. Mentovich, J. Bauwelinck, and C. Koos, "100 Gbit/s serial transmission using a silicon-organic hybrid (SOH) modulator and a duobinary driver IC," in *Optical Fiber Communications Conference and Exhibition (OFC)* (2017).

106. J.-M. Brosi, C. Koos, L. C. Andreani, M. Waldow, J. Leuthold, and W. Freude, "High-speed low-voltage electro-optic modulator with a polymer-infiltrated silicon photonic crystal waveguide," Opt. Express **16**, 4177 (2008).

107. X. Zhang, C.-J. Chung, A. Hosseini, H. Subbaraman, J. Luo, A. K.-Y. Jen, R. L. Nelson, C. Y.-C. Lee, and R. T. Chen, "High Performance Optical Modulator

Based on Electro-Optic Polymer Filled Silicon Slot Photonic Crystal Waveguide," J. Light. Technol. **34**, 2941–2951 (2016).

108. C. Koos, J. Leuthold, W. Freude, M. Kohl, L. Dalton, W. Bogaerts, A. L. Giesecke, M. Lauermann, A. Melikyan, S. Koeber, S. Wolf, C. Weimann, S. Muehlbrandt, K. Koehnle, J. Pfeifle, W. Hartmann, Y. Kutuvantavida, S. Ummethala, R. Palmer, D. Korn, L. Alloatti, P. C. Schindler, D. L. Elder, T. Wahlbrink, and J. Bolten, "Silicon-Organic Hybrid (SOH) and Plasmonic-Organic Hybrid (POH) Integration," J. Light. Technol. **34**, 256–268 (2016).

109. A. Melikyan, L. Alloatti, A. Muslija, D. Hillerkuss, P. C. Schindler, J. Li, R. Palmer, D. Korn, S. Muehlbrandt, D. Van Thourhout, B. Chen, R. Dinu, M. Sommer, C. Koos, M. Kohl, W. Freude, and J. Leuthold, "High-speed plasmonic phase modulators," Nat. Photonics **8**, 229–233 (2014).

110. H. Yan, X. Xu, C.-J. Chung, H. Subbaraman, Z. Pan, S. Chakravarty, and R. T. Chen, "One-dimensional photonic crystal slot waveguide for silicon-organic hybrid electro-optic modulators," Opt. Lett. **41**, 5466 (2016).

111. R. Palmer, S. Koeber, D. L. Elder, M. Woessner, W. Heni, D. Korn, M. Lauermann, W. Bogaerts, L. Dalton, W. Freude, J. Leuthold, and C. Koos, "High-Speed, Low Drive-Voltage Silicon-Organic Hybrid Modulator Based on a Binary-Chromophore Electro-Optic Material," J. Light. Technol. **32**, 2726–2734 (2014).

112. R. Palmer, L. Alloatti, D. Korn, P. C. Schindler, R. Schmogrow, W. Heni, S. Koenig, J. Bolten, T. Wahlbrink, M. Waldow, H. Yu, W. Bogaerts, P. Verheyen, G. Lepage, M. Pantouvaki, J. Van Campenhout, P. Absil, R. Dinu, W. Freude, C. Koos, and J. Leuthold, "Silicon-Organic Hybrid MZI Modulator Generating OOK, BPSK and 8-ASK Signals for Up to 84 Gbit/s," IEEE Photonics J. **5**, 6600907–6600907 (2013).

113. R. Ding, T. Baehr-Jones, Y. Liu, R. Bojko, J. Witzens, S. Huang, J. Luo, S. Benight, P. Sullivan, J.-M. Fedeli, M. Fournier, L. Dalton, A. Jen, and M. Hochberg, "Demonstration of a low V_πL modulator with GHz bandwidth based on electro-optic polymer-clad silicon slot waveguides," Opt. Express **18**, 15618 (2010).

114. T. Baehr-Jones, B. Penkov, J. Huang, P. Sullivan, J. Davies, J. Takayesu, J. Luo, T.-D. Kim, L. Dalton, A. Jen, M. Hochberg, and A. Scherer, "Nonlinear polymer-clad silicon slot waveguide modulator with a half wave voltage of 0.25V," Appl. Phys. Lett. **92**, 163303 (2008).

115. M. Gould, T. Baehr-Jones, R. Ding, S. Huang, J. Luo, A. K.-Y. Jen, J.-M. Fedeli, M. Fournier, and M. Hochberg, "Silicon-polymer hybrid slot waveguide ring-resonator modulator," Opt. Express **19**, 3952 (2011).

116. J. Takayesu, M. Hochberg, T. Baehr-Jones, E. Chan, Guangxi Wang, P. Sullivan, Yi Liao, J. Davies, L. Dalton, A. Scherer, and W. Krug, "A Hybrid Electrooptic

Microring Resonator-Based 1 X 4 X 1 ROADM for Wafer Scale Optical Interconnects," J. Light. Technol. **27**, 440–448 (2009).

117. X. Sun, D. Dai, L. Thylén, and L. Wosinski, "Double-Slot Hybrid Plasmonic Ring Resonator Used for Optical Sensors and Modulators," Photonics **2**, 1116–1130 (2015).

118. P. Steglich, C. Mai, D. Stolarek, S. Lischke, S. Kupijai, C. Villringer, S. Pulwer, F. Heinrich, J. Bauer, S. Meister, D. Knoll, M. Casalboni, and S. Schrader, "Novel Ring Resonator Combining Strong Field Confinement With High Optical Quality Factor," IEEE Photonics Technol. Lett. **27**, 2197–2200 (2015).

119. P. Rabiei, W. H. Steier, C. Zhang, and L. R. Dalton, "Polymer micro-ring filters and modulators," Light. Technol. J. **20**, 1968–1975 (2002).

120. F. Qiu, H. Sato, A. M. Spring, D. Maeda, M. Ozawa, K. Odoi, I. Aoki, A. Otomo, and S. Yokoyama, "Ultra-thin silicon/electro-optic polymer hybrid waveguide modulators," Appl. Phys. Lett. **107**, 123302 (2015).

121. F. Y. Gardes, A. Brimont, P. Sanchis, G. Rasigade, D. Marris-Morini, L. O'Faolain, F. Dong, J. M. Fedeli, P. Dumon, L. Vivien, T. F. Krauss, G. T. Reed, and J. Marti, "High-speed modulation of a compact silicon ring resonator," 2009 6th IEEE Int. Conf. Gr. IV Photonics **17**, 241–243 (2009).

122. T. Baba, S. Akiyama, M. Imai, N. Hirayama, H. Takahashi, Y. Noguchi, T. Horikawa, and T. Usuki, "50-Gb/s ring-resonator-based silicon modulator," Opt. Express **21**, 11869 (2013).

123. J.-M. Lee, D.-J. Kim, H. Ahn, S.-H. Park, and G. Kim, "Temperature Dependence of Silicon Nanophotonic Ring Resonator With a Polymeric Overlayer," J. Light. Technol. **25**, 2236–2243 (2007).

124. M. Lauermann, R. Palmer, S. Koeber, P. C. Schindler, D. Korn, T. Wahlbrink, J. Bolten, M. Waldow, D. L. Elder, L. R. Dalton, J. Leuthold, W. Freude, and C. Koos, "Low-power silicon-organic hybrid (SOH) modulators for advanced modulation formats," Opt. Express **22**, 29927 (2014).

125. R. Halir, P. J. Bock, P. Cheben, A. Ortega-Moñux, C. Alonso-Ramos, J. H. Schmid, J. Lapointe, D.-X. Xu, J. G. Wangüemert-Pérez, Í. Molina-Fernández, and S. Janz, "Waveguide sub-wavelength structures: a review of principles and applications," Laser Photon. Rev. **9**, 25–49 (2015).

126. Y. Xiong, D. X. Xu, J. H. Schmid, P. Cheben, and W. N. Ye, "High Extinction Ratio and Broadband Silicon TE-Pass Polarizer Using Subwavelength Grating Index Engineering," IEEE Photonics J. **7**, (2015).

127. J. H. Schmid, P. Cheben, S. Janz, J. Lapointe, E. Post, A. Delâge, A. Densmore, B. Lamontagne, P. Waldron, and D. X. Xu, "Subwavelength grating structures in silicon-on-insulatorwaveguides," Adv. Opt. Technol. **17**, 19120–19133 (2008).

128. J. D. Sarmiento-Merenguel, A. Ortega-Moñux, J.-M. Fédéli, J. G. Wangüemert-Pérez, C. Alonso-Ramos, E. Durán-Valdeiglesias, P. Cheben, Í. Molina-Fernández, and R. Halir, "Controlling leakage losses in subwavelength grating silicon metamaterial waveguides," Opt. Lett. **41**, 3443 (2016).

129. S. Inoue and A. Otomo, "Electro-optic polymer/silicon hybrid slow light modulator based on one-dimensional photonic crystal waveguides," Appl. Phys. Lett. **103**, 171101 (2013).

130. J. Gonzalo Wangüemert-Pérez, P. Cheben, A. Ortega-Moñux, C. Alonso-Ramos, D. Pérez-Galacho, R. Halir, I. Molina-Fernández, D.-X. Xu, and J. H. Schmid, "Evanescent field waveguide sensing with subwavelength grating structures in silicon-on-insulator," Opt. Lett. **39**, 4442 (2014).

131. V. Donzella, J. Flueckiger, A. Sherwali, S. T. Fard, S. M. Grist, and L. Chrostowski, "Compact and broad band directional coupler for sub-wavelength grating SOI components," 2014 IEEE Photonics Conf. IPC 2014 **3**, 607–608 (2014).

132. P. J. Bock, P. Cheben, J. H. Schmid, J. Lapointe, A. Delâge, S. Janz, G. C. Aers, D.-X. Xu, A. Densmore, and T. J. Hall, "Subwavelength grating periodic structures in silicon-on-insulator: a new type of microphotonic waveguide.," Opt. Express **18**, 20251–62 (2010).

133. J. Flueckiger, S. Schmidt, V. Donzella, A. Sherwali, D. M. Ratner, L. Chrostowski, and K. C. Cheung, "Sub-wavelength grating for enhanced ring resonator biosensor," Opt. Express **24**, 15672 (2016).

134. X. Xu, H. Subbaraman, J. Covey, D. Kwong, A. Hosseini, and R. T. Chen, "Colorless grating couplers realized by interleaving dispersion engineered subwavelength structures," Opt. Lett. **38**, 3588 (2013).

135. X. Xu, H. Subbaraman, J. Covey, D. Kwong, A. Hosseini, and R. T. Chen, "Complementary metal–oxide–semiconductor compatible high efficiency subwavelength grating couplers for silicon integrated photonics," Appl. Phys. Lett. **101**, 31109 (2012).

136. Z. Wang, X. Xu, D. Fan, Y. Wang, H. Subbaraman, and R. T. Chen, "Geometrical tuning art for entirely subwavelength grating waveguide based integrated photonics circuits," Sci. Rep. **6**, 24106 (2016).

137. X. Xu, Z. Pan, B. Jia, Y. Wang, and R. T. Chen, "All-optical switch with 1 ps response time enabled by graphene oxide infiltrated subwavelength grating waveguide," in *Photonics West* (SPIE, 2017), p. 1010805.

138. G. T. Reed, G. Mashanovich, F. Y. Gardes, and D. J. Thomson, "Silicon optical modulators," Nat. Photonics **4**, 518–526 (2010).

139. C. C. Teng, M. A. Mortazavi, and G. K. Boudoughian, "Origin of the poling-

induced optical loss in a nonlinear optical polymeric waveguide," Appl. Phys. Lett. **66**, 667–669 (1995).

140. A. Yacoubian, W. Lin, D. J. Olson, and J. H. Bechtel, "Analysis of poling-induced polymer waveguide losses in push-pull Mach-Zehnder modulators," in *International Symposium on Optical Science and Technology* (2001), Vol. 4455, pp. 181–188.

141. H. Chen, B. Chen, D. Huang, D. Jin, J. D. Luo, A. K.-Y. Jen, and R. Dinu, "Broadband electro-optic polymer modulators with high electro-optic activity and low poling induced optical loss," Appl. Phys. Lett. **93**, 43507 (2008).

142. X. Zhang, A. Hosseini, S. Chakravarty, J. Luo, A. K. Y. Jen, and R. T. Chen, "Wide optical spectrum range, subvolt, compact modulator based on an electro-optic polymer refilled silicon slot photonic crystal waveguide," Opt. Lett. **38**, 4931–4934 (2013).

143. L. Chrostowski and M. Hochberg, *Silicon Photonics Design: From Devices to Systems* (Cambridge University Press, 2015).

144. L. G. Roberts, "Beyond Moore's law: Internet growth trends," Computer (Long. Beach. Calif). **33**, 117–119 (2000).

145. W. Śmigaj, P. Lalanne, J. Yang, T. Paul, C. Rockstuhl, and F. Lederer, "Closed-form expression for the scattering coefficients at an interface between two periodic media," Appl. Phys. Lett. **98**, 111107 (2011).

146. L.-W. Luo, N. Ophir, C. P. Chen, L. H. Gabrielli, C. B. Poitras, K. Bergmen, and M. Lipson, "WDM-compatible mode-division multiplexing on a silicon chip," Nat. Commun. **5**, 3069 (2014).

147. J. M. Kahn and K.-P. Ho, "Spectral Efficiency Limits and Modulation/Detection Techniques for DWDM Systems," IEEE J. Sel. Top. Quantum Electron. **10**, 259–272 (2004).

148. J. Callaway, "Optical Absorption in an Electric Field," Phys. Rev. **130**, 549–553 (1963).

Vita

Zeyu Pan received his B.S. degree in Optical Information Science & Technology from Nanjing University of Science and Technology in 2010 and the M.S. degree in Electrical and Computer Engineering from University of Alabama in Huntsville in 2013. He is currently working toward the Ph.D. degree in University of Texas at Austin. He has authored and coauthored about 41 journal and conference publications. His interests include the polymer/silicon waveguide, optical modulator, optical switches, printed flexible electronics & photonics, Patch Array Antennas (PAA), thermo- and electro-optic polymers, phase delay, nanofabrication, RF measurements, inkjet printing, imprinting, and numerical algorithms.

Email: panzeyu@utexas.edu

This dissertation was typed by the author.